Abstract

Spatial degrees of freedom in multimode fibers

Wen Xiong

2020

Multimode fibers are complex and versatile photonic systems, providing a multi-functional platform for studying fundamental optical physics and applications. Spatial degrees of freedom in multimode fibers have been explored for a wide range of applications from space-division multiplexing in optical communication, fiber endoscopy to fiber lasers and spectroscopy. In this thesis, we investigate spatial degrees of freedom in multimode fibers to understand wave physics in this system and to utilize spatial degrees of freedom in multimode fibers for communication and novel optical sensing.

At first, we systematically discuss spatiotemporal control of light transmitted through multimode fibers. Taking advantage of the coupling between spatial and temporal degrees of freedom in multimode fibers, we can effectively control the temporal profile of a transmitted pulse by manipulating the input wavefront. Specifically, we show that by preparing the input wavefront to be a principal mode, modal dispersion can be suppressed and the temporal profile of the input can be retained. We study principal modes and their bandwidth in both the weak and the strong mode coupling regimes. We find that principal modes are only effective within a finite frequency range because of the first-order approximation in the definition. We improve the bandwidth of principal modes with a nonlinear optimization algorithm. Using principal modes as the initial guess, we find modes with broader bandwidths. The obtained modes are named super-principal modes. Reversing the concept, we deploy the same optimization algorithm to find anti-principal modes, which exhibit the narrowest bandwidths. Anti-principal modes suffer from strong modal dispersion and

thus can find applications in multimode-fiber-based spectrometers.

Super-principal-modes have broader bandwidths than principal modes, but it is unknown whether a super-principal-mode is the most effective way of delivering an optical pulse through the multimode fiber. We also address this fundamental question in this thesis. By measuring a time-resolved transmission matrix of the multimode fiber, we use eigenchannels of the transmission matrix to deliver the maximal energy of a pulse at arbitrary arrival time. We further discover that long-range correlation in the fiber assists the pulse delivery. The relationship between principal modes and eigenchannels of the time-resolved transmission matrix is also discussed.

Secondly, we demonstrate that input spatial degrees of freedom can also exert effective control over the output polarization states. By manipulating the input wavefront, a multimode fiber can function as a reconfigurable matrix of waveplates. We also reveal the analogy between the polarization mixing in a multimode fiber and the wave transport in a chaotic cavity. The theory developed for chaotic cavities predicts the polarization extinction ratio.

Finally, spatial degrees of freedom at the output, i.e., spatial speckle patterns formed by multimodal interference in the fiber, can be utilized for ultrafast pulse characterization. In this part, we first demonstrate a linear single-shot temporal measurement technique based on a multimode fiber. Complex spatiotemporal speckle fields are created by a well-characterized pulse propagating through the fiber. By interfering an unknown pulse signal with the spatiotemporal speckles, both the amplitude and phase of the unknown signal are retrieved. The method has high sensitivity and a broad measuring range, but it requires a reference pulse. We further study the more challenging problem of characterizing an ultrafast pulse without a reference pulse. We propose a method of using two-photon speckle patterns formed at the end of a multimode fiber for pulse recovery. The two-photon pattern is the fingerprint of pulses. A deep neural network is implemented to decode the temporal profile from the speckle pattern. A Multimode fiber combined with computational algorithms can be a versatile platform for optical sensing.

Spatial degrees of freedom in multimode fibers

A Dissertation
Presented to the Faculty of the Graduate School
of
Yale University
in Candidacy for the Degree of
Doctor of Philosophy

by
Wen Xiong

Dissertation Director: Professor Hui Cao

2020

Contents

List of Figures

Acknowledgements

My six-year Ph.D. study at Yale is a long and exciting journey. Six years ago, with just two suitcases, I came to the U.S. from China to start this adventure. I was concerned and confused at the beginning, but I am lucky to make it to the end. It would be impossible without the help, guidance, and company from amazing people I got to know here at Yale.

First of all, I want to thank my thesis advisor Prof. Hui Cao for her mentorship. Hui is so available to her students. We have a one-on-one meeting every week. She is always open and willing to discussions. I learn new things from her in each meeting. She has extraordinary physics intuitions which I may never catch up with, but at least I have made some progress. I learned not only science but also the persistent, passionate and hardworking attitude toward difficulties in science from her. She also gave me valuable suggestions to polish my communication skills, which has been so beneficial to me when I present at conferences and when I give job talks. Hui was also very supportive when she knew my interest in industry jobs. She allowed me to do a summer internship so that I could get a flavor of the industry. I am grateful to her significant contribution to this thesis and to her endeavor of mentoring me. I also want to thank my thesis committee members Prof. Douglas Stone and Prof. Peter Rakich for their helpful suggestions and advice. They are so kind and easy to communicate with. I learned a lot of optics and physics from them in joint group meetings and discussions. All the knowledge I learned from them will be with me

and help me in my future research.

Secondly, I want to thank all the colleagues in our research group. Special thanks to Dr. Yaron Bromberg and Dr. Chia Wei (Wade) Hsu. Thank Yaron for his help and guidance during my early Ph.D. time. His guidance and help assured me when I just started my research here at Yale. He also encouraged me with his own story to continue Ph.D. studies when I wanted to give up. I have been missing him after he started his faculty position in Israel. Wade is super helpful and efficient. He contributed significantly to my research projects. He can always give insights and suggestions. I am lucky to have the chance to work with him. I also want to thank other former group members Dr. Stefan Bittner, Dr. Seng Fatt Liew, Dr. Brandon Redding, Dr. Sebastian Knitter, Dr. Raktim Sarma, and Shai Gertler. They always gave me valuable assistance and help in the lab. Many thanks to our current group members Dr. Hasan Yilmaz, Dr. Yaniv Eliezer, Nicolas Bender and KyungDuk Kim for the help and the happy time we spent together in the basement of Becton. All the people in the research group are open-minded, helpful and generous. I couldn't have finished my Ph.D. without their help. I also want to thank the admin staff Maria Rao, Giselle Maillet, Alex Bozzi in the Applied Physics Department. They are so helpful and kind. I could have lost in endless paperwork without them.

I would like to thank my collaborators in TU Wien Prof. Stefan Rotter and Dr. Philipp Ambichl for their theoretical contribution to the principal mode projects. Thank Matthias Khmayer for stimulating discussions on fibers. Thank Prof. Rodrigo Amezcua Correa in CREOL, UCF for providing some of the fiber samples. I also thank Prof. Tsampikos Kottos, Dr. Huanan Li and Poom Chiarawongse at Wesleyan University for their collaboration on fiber mode-dependent loss study. I am grateful for the opportunity of collaborating with these brilliant theoreticians. I would also like to thank Dr. Nicolas Fontaine and Dr. Joel Carpenter for stimulating discussions and communication at conferences. I want to thank Dr. Ming-Jun Li and Dr. Steven

Rosenblum for their guidance in my internship at Corning Research & Development. Ming is an expert in fiber optics, from fiber design to fabrication. We worked together on designing new fibers for telecommunication challenges. Rosie hired me for this internship and gave me useful career suggestions. The internship is a precious experience for me.

My friends at Yale make my life enjoyable and wonderful. I would like to thank Dandan Ji, Luyao Jiang, Minglei Wang, Xin Liang, Xin Yan, Yuan Yuan, Silin Ren, and Yizhi Luo and many other Yalies for their friendship and company. I will always remember the delighted moments we had together wherever I go. I also thank my bestie Xi Xiong for her 29 years of friendship. Though we have been far apart for six years, she has been giving me support and care along the way.

I thank my parents for their unconditional love. My hometown is in a less-developed area in China and there are only limited education resources. But my parents valued education and provided me the best education they could afford from primary school to college. They gave out everything to me without reservation. They supported me when I decided to come to this distant country for Ph.D. studies. For six years, I only had time to visit them twice. As the only child of them, I sometimes feel guilty and I do not know how to pay them back. I can only do better to make them proud of me. Finally, I would like to thank Siyuan Dong, my caring and supportive husband, for his love. From undergrad to Ph.D., from Hangzhou to New England, life has had ups and downs but he has always been there for me. He is a knowledgeable colleague in science and a faithful partner in life. More importantly, his persistence, intelligence, and hard work inspired me to overcome difficulties in Ph.D. studies. It would not be possible for me to finish this long and tough journey without his encouragement, support and love.

Chapter 1

Introduction

1.1 Multimode optical fibers

An optical fiber is a cylindrical optical waveguide composed of a core embedded in a cladding with a lower refractive index. It confines light by total internal reflection for light with incident angles larger than the critical angle. When the core diameter is small, only a single mode is supported and the fiber is called single-mode fiber (SMF). Fibers with larger cores are multimode fibers (MMFs) which supports many propagating modes. Optical fibers are usually made of low-loss materials such as silica, and the loss has been reduced to 0.15 dB/km by improving the purity of the material. The low-loss and high-bandwidths properties of optical fibers revolutionized communications ranging from data transmission across different continents to computer communications within a local network.

MMFs are widely used in optical fiber communication within a local network such as within a campus or a data center. MMFs are favored in short-haul communications systems because of the higher tolerance of connector alignments and reduced costs of transceiver components. An MMF is characterized by a few important parameters: the fiber core radius a, the refractive index contrast Δ, and the index profile

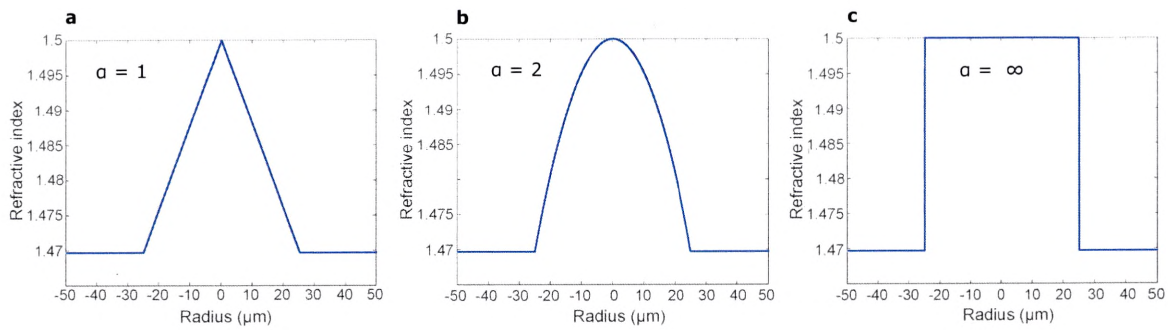

Figure 1.1: Refractive index profiles of MMFs with different α parameters.

parameter α. The index contrast between the cladding and the core is defined as $\Delta = \frac{n_{\text{core}}^2 - n_{\text{cladding}}^2}{2n_{\text{core}}^2}$, where n_{core} and n_{cladding} are the corresponding refractive index of the cladding and the core. The numerical aperture (NA) of the fiber is the sine of that maximum angle of an incident ray that can be guided by total internal reflection. The NA of the fiber is related with the index contrast by $\text{NA} = \text{n}_{\text{core}}\sqrt{2\Delta}$. The index profile is determined by a parameter α by

$$n(r) = \begin{cases} n_{\text{core}}[1 - 2\Delta(\frac{r}{a})^{\alpha}]^{1/2}, & \text{for } r < a \\ n_{\text{cladding}}, & \text{for } r \geq a. \end{cases}$$

The values of α are between 1 and ∞. The profile is triangular when $\alpha = 1$, parabolic when $\alpha = 2$ and step when $\alpha = \infty$, as shown in Fig. 1.1. The commercially available MMFs usually have parabolic or step index profiles shown in Fig. 1.1(b) and (c).

With a specified refractive index boundary condition, Maxwell's equations can be solved and the corresponding solutions are fiber eigenmodes. An MMF supports many modes, each having a different electromagnetic field profile. A detailed analysis of fiber eigenmodes is available in [1]. When the index contrast is small, under the weak guiding approximation, fiber eigenmodes can be reduced to linearly polarized (LP) modes. Each spatial intensity profile corresponds to the two degenerate orthogonal linear polarizations. In Fig. 1.2, we show all the horizontally polarized LP modes of an MMF with $a = 25$ μm, $\alpha = \infty$ and NA = 0.22 at wavelength $\lambda = 1550$ nm.

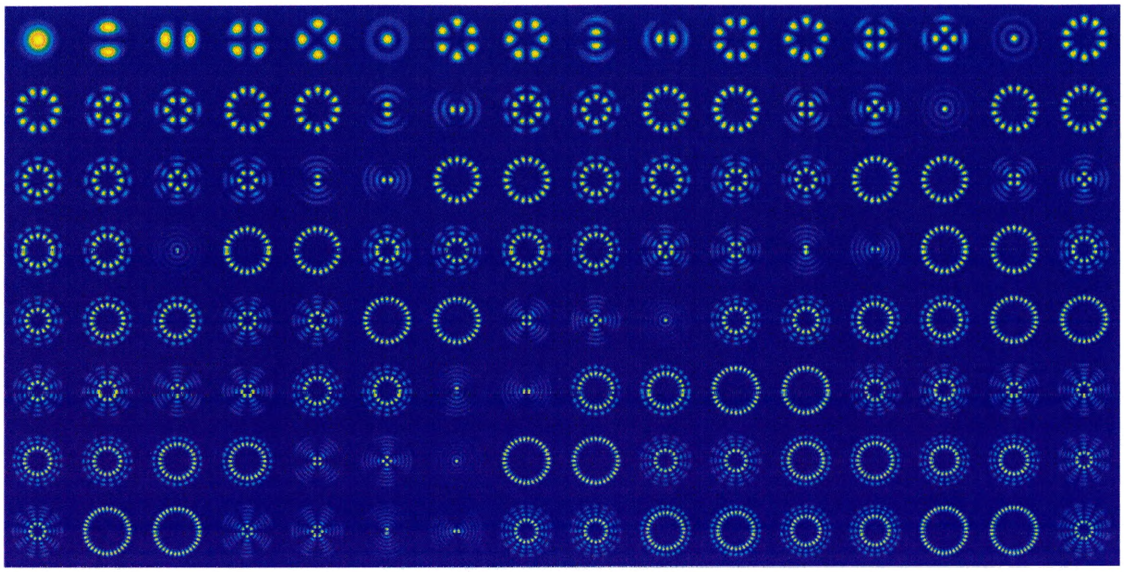

Figure 1.2: 128 spatial intensity profiles of a step-index MMF with $a = 25$ μm, NA $= 0.22$.

A quick and rough estimation of the number of modes is to use the V number. It is defined as $V = \frac{2\pi}{\lambda} a\mathrm{NA}$ for a step-index fiber. For V values below 2.405, a fiber supports only one mode per polarization. This is also the cut-off condition for SMFs. For large values, the number of supported modes can be calculated approximately as $M = \frac{V^2}{2}$. With the parameters of the MMF specified above, we obtain 124 modes, close to the numerical result in Fig. 1.2.

Each LP mode travels with a distinct propagation constant and group velocity. This results in a variety of arrival times when different modes travel through the fiber so that the output light pulses are distorted and broadened. This effect is named modal dispersion, which limits the separation between adjacent pulses that can be sent without overlapping and thus limits the bandwidth the communication system can operate. The broadening of the output pulse can be quantified as the differential group delays (DGDs), representing the strength of modal dispersion in an MMF. DGDs increase with the length of the fiber. Even when light is launched into a single LP mode, imperfections of the index profile and environmental perturbations such as bending and twisting cause mode coupling, making the signal subject to modal

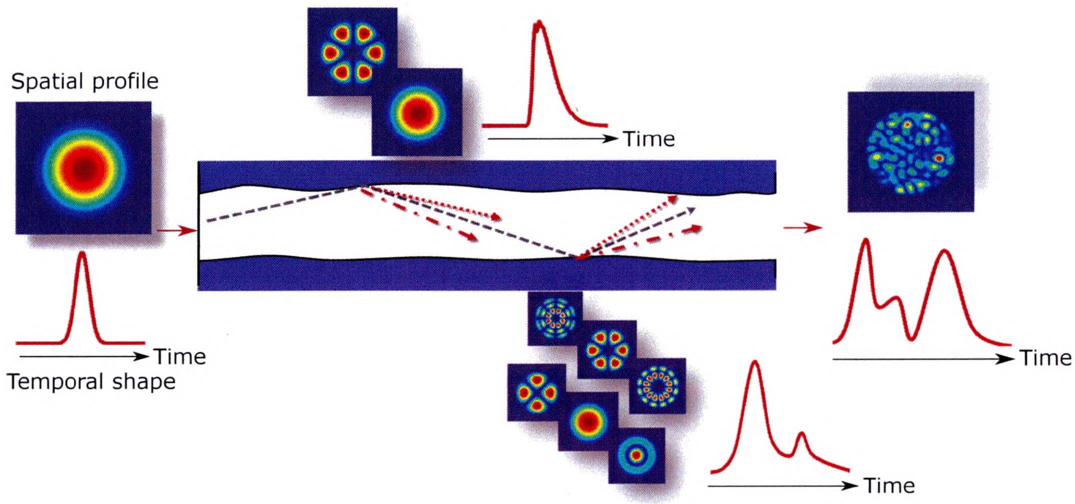

Figure 1.3: Differential group delay (DGD) introduced by mode coupling in an MMF with intrinsic or external defects.

dispersion. Figure 1.3 illustrates the DGD introduced by mode coupling in an MMF with defects. Modal dispersion is the main reason why MMFs are only used in short-haul fiber-optic communications.

SMFs are free from modal dispersion because only one spatial mode (including two orthogonal polarizations) is supported. All available degrees of freedom such as time, wavelength, phase and polarization have already been deployed for increasing the capacity. The capacity of SMFs based fiber-optic communication systems is approaching its fundamental limit imposed by fiber nonlinearity and optical amplification noise [2]. To further improve the capacity of fiber-optic communications, space-division multiplexing (SDM) are proposed [3]. SDM exploits a plurality of modes in an MMF as independent channels to transmit parallel data streams. Long-distance propagations inevitably cause coupling between different modes. Thus effective mitigation of DGDs will play an important role in utilizing MMFs in space-division-multiplexing and increasing the capacity of fiber-optic communication systems. In chapter 2-4 of this thesis, we will explore the methods of mitigating modal dispersion in an MMF. These methods harness input spatial degrees of freedom in MMFs. By controlling

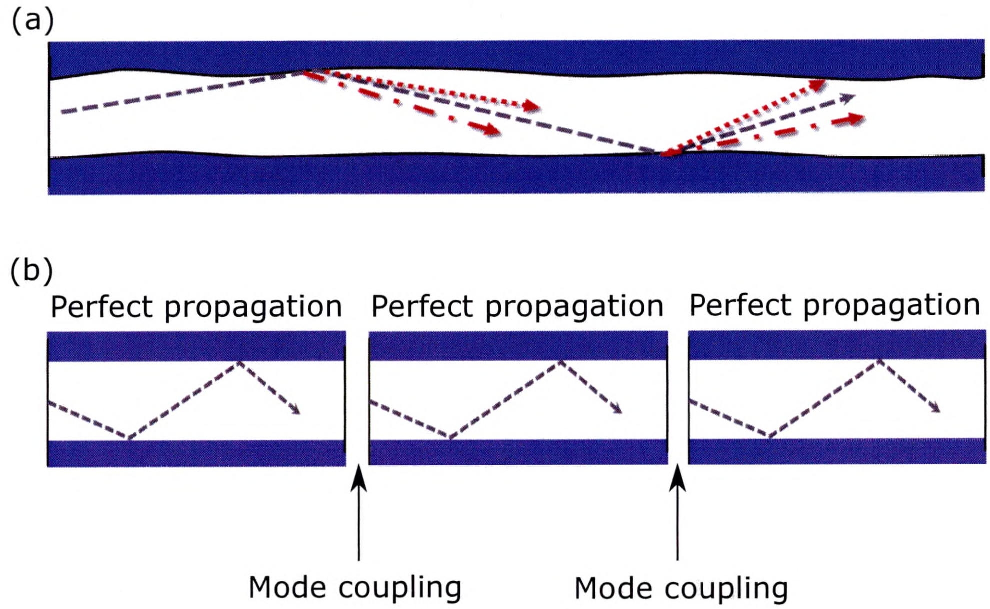

Figure 1.4: Concatenated fiber model. (a) In a realistic fiber, mode coupling happens gradually as light propagate through the fiber. (b) In the concatenated fiber model, mode mixing only happens at the joints of adjacent fiber segments.

the spatial wavefront launched into the MMF, a significant reduction of DGDs are achieved.

1.2 Mode coupling model

DGDs are closely related to the mode coupling process when light propagates through an MMF. Mode coupling occurs gradually in an MMF as shown in Fig. 1.4(a). A simpler concatenated fiber model has been proposed to mimic strong mode coupling in MMFs and thus understand DGDs in the strong mode coupling regime [4]. Figure 1.4(b) illustrates the model. The MMF is divided into multiple sections. In each section, there is only perfect propagation without mode coupling. At the joint of two sections, a complete mode coupling happens. After the mode coupling, the scattered modes propagate in another perfect fiber section again. The length of the section is determined by the correlation length of the fiber under consideration. It is defined as the propagation distance after which a single LP mode input is coupled to all other

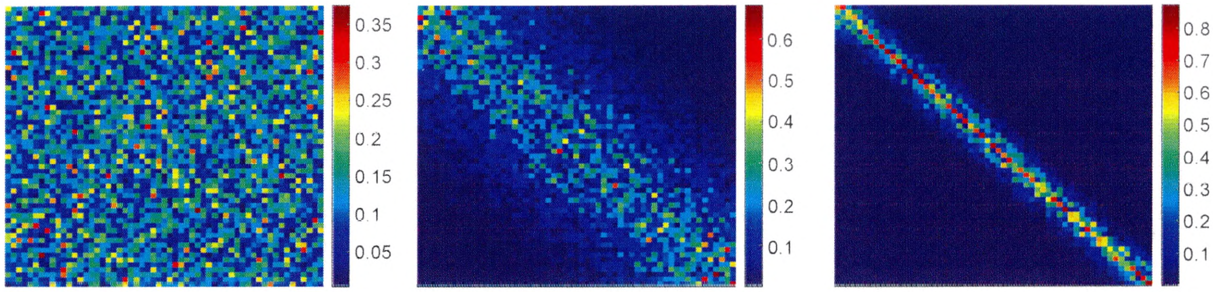

Figure 1.5: Mode coupling matrix with tunable coupling strength from strong mode coupling (left) to weak mode coupling (right).

LP modes. The correlation length is analogous to the transport mean free path in disordered scattering media [5]. An MMF in the strong mode coupling regime refers to a fiber that can be modeled by more than one segment. Otherwise, the fiber is in the weak mode coupling regime.

Mathematically, each fiber segment is represented by the product of three matrices $M(\omega) = V\Lambda(\omega)U$. $\Lambda(\omega)$ is a diagonal matrix with elements being the frequency-dependent phase term $e^{-i\beta_n(\omega)L}$, where $\beta_n(\omega)$ is the propagation constant of mode n and L is the length of the segment. U and V are random unitary matrices representing the mode coupling at the input and output joints. The mode coupling matrices are assumed to be wavelength-independent. The wavelength dependence of each segment is only from the propagation matrix. The matrix representing the entire fiber is the product of the matrix of each segment. The entire fiber can be represented by a Gaussian unitary random matrix. With this simplified mode, it has been reported that the DGD scales with the square root of fiber length [4]. In contrast, the DGD increases linearly with the length of the fiber in the weak mode coupling regime. Strong mode coupling brings the advantage of slowly growing DGDs in long MMFs.

We further generalize this fiber model to the weak mode coupling regime by replacing the random unitary coupling matrix at the joint with a matrix of attenuated off-diagonal elements [6]. The matrix is $A = \exp[iH]$, where H is a random Hermitian matrix. We construct $H = G\cdot(R+R^\dagger)$, in which R is a complex random matrix whose elements are taken from the normal distribution, and G is a real matrix imposing a Gaussian envelope function on the matrix elements along the off-diagonal direction. The magnitude of the matrix elements decays away from the diagonal, and the decay rate, i.e., the width of the Gaussian envelope function, depends on the degree of mode coupling, as shown in Fig. 1.5. In this thesis, we use this generalized concatenated fiber model to simulate light propagation in MMFs with mode mixing.

1.3 Multimode fibers as complex photonic structures

Mode coupling in MMFs is analogous to multiple scatterings in disordered media. In disordered media, light is scattered to different directions (k vectors) due to inhomogeneities in the refractive index. In an MMF, light is scattered to different LP modes due to variations of the fiber cross-section. Like the disordered scattering media, an MMF can be considered as a complex photonic structure [7, 8] with diverse and coupled degrees of freedom in space, time, spectrum and polarization. Figure 1.6 conceptually illustrates the coupling between different degrees of freedom in an MMF with mode mixing. The degrees of freedom in the spectrum domain at the input is coupled to the spatial degrees of freedom at the output, resulting wavelength-dependent speckle patterns, as shown in Fig. 1.6(a). Moreover, temporal degrees of freedom are coupled with spatial degrees of freedom. For an optical pulse incident into disorder media, each output spatial channel generates a different temporal trace, as indicated in Fig. 1.6(b). The polarization states are also coupled with spatial degrees of freedom after multiple scatterings, as shown in Fig. 1.6(c). The coupling between different degrees of freedom in electromagnetic waves enables controlling or measuring degrees of freedom in one domain with degrees of freedom in another domain. For example, with the spatial degrees of freedom, the temporal

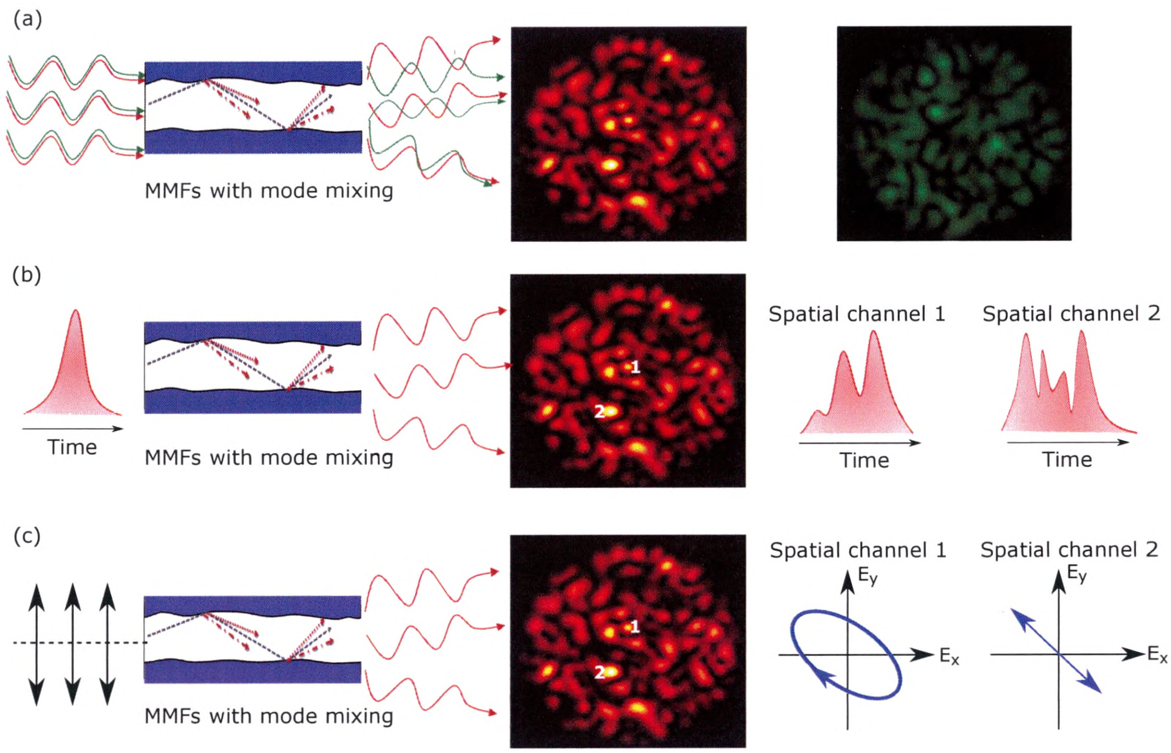

Figure 1.6: Complex coupling between different degrees of freedom in an MMF with mode mixing. (a) Input degrees of freedom in the spectrum domain is coupled to spatial degrees of freedom at the output. Light with different frequencies generates distinct patterns. (b) Temporal degrees of freedom are coupled with spatial degrees of freedom in an MMF with mode mixing. Each output spatial channel generates a different temporal profile. (c) Polarization degrees of freedom are coupled with spatial degrees of freedom. The polarization state of each speckle grain is different.

profile of an ultrashort pulse transmitted through a disordered scattering medium can be compressed [9].

The advantage of MMFs over disordered media is that the scattered light in other modes still propagates forward and thus the transmission of light through an MMF is very high. Furthermore, spatial modes in an MMF can be controlled by the fiber parameters. The number of modes can be tuned from a few modes to thousands of modes. In contrast, the number of spatial modes in an open disordered media is above millions, preventing a complete characterization of the system. It is possible to exert complete control of the spatial degrees of freedom in MMFs, which is not obtainable in disordered media. Hence, an MMF provides a controllable, highly transmitting, versatile and multi-functional platform for communication, imaging and sensing applications [3, 10–13].

In this thesis, we will understand the couplings between different degrees of freedom and utilize them. For example, the abundant input spatial degrees of freedom can be utilized for controlling linear propagation of light in MMFs. The temporal and polarization states of transmitted light are manipulated by shaping the spatial wavefront of an incident beam. Modal dispersion and depolarization in MMFs can be suppressed. Therefore, an MMF can function as a pulse shaper or a reconfigurable polarizer. We will also exploit the reverse process, i.e., extracting input information such as the spectrum and temporal profile from the speckle patterns formed by multimodal interference at the output. In the next subsections, we review the technique of wavefront shaping to access input spatial degrees of freedom and present an example of using speckle patterns in MMFs for spectroscopy.

1.3.1 Wavefront shaping

Wavefront shaping was first used in astronomy to compensate optical aberrations of light transmitted through the atmosphere. The technology was based on a device named spatial light modulator (SLM), which could modulate the shape of electromagnetic waves. However, with only dozens of pixels, SLMs at that time were not able to correct strong aberrations. With the development of the technology of liquid crystals and micro-electro-mechanical systems, SLMs now have millions of pixels. With the abundant number of spatial degrees of freedom, SLMs open the way of studying complex photonic systems where light is strongly scattered or distorted [7, 8].

The pioneering work of wavefront shaping in strong scattering media was performed by Vellekoop and Mosk [14]. They demonstrated focusing of light through opaque scattering media by controlling the incident wavefront. Unlike other techniques such as multi-photon microscopy or optical coherence tomography which select

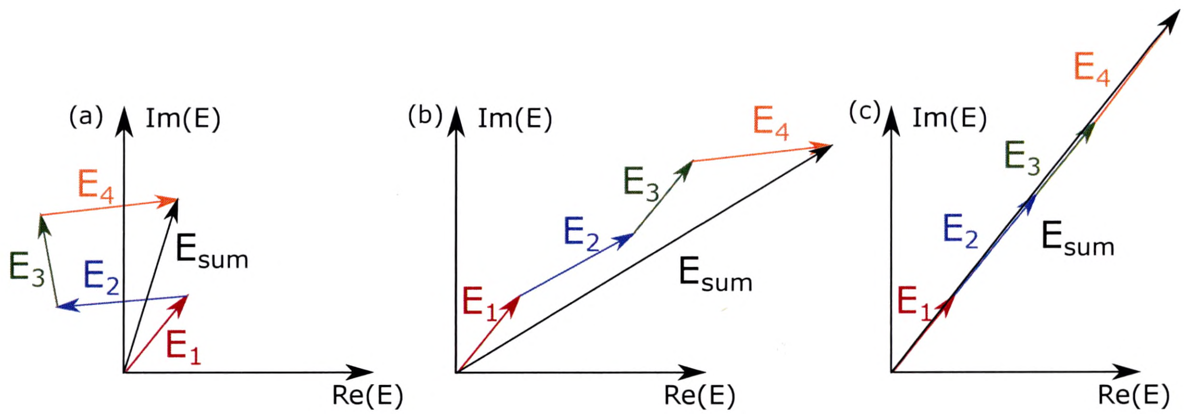

Figure 1.7: Representation in the complex plane of the amplitude at the focus in the optimization process. (a) Before the optimization, the electric field adds up randomly, resulting a small total amplitude E_{sum}. (b) During the optimization process, the electric field aligns and the total amplitude is enhanced. (c) After the optimization, the field is well-aligned and the total amplitude is maximized.

ballistic photons from scattering samples, wavefront shaping aligns the phase of the scattered waves, giving rise to a bright focus spot. This is achieved by optimizing the phase of the incident wave, which is schematically illustrated in Figure 1.7. At the target position, the light field is the sum of contributions from each input pixel. Before optimization, the phase of the wave from each pixel is random. The modulus of the field can be seen as a random walk in the complex plane and is proportional to the square root of the number of pixels N. During the optimization process, the scattered waves are iteratively aligned one by one to increase the intensity. At the end of the optimization, ideally, the amplitude is proportional to the number of pixels N. The intensity at the target position is $N\pi/4$ times stronger than that before the optimization [7].

Optimizing the incident wavefront to enhance intensity at a single speckle behind the scattering media is equivalent to measuring a single column of the transmission matrix of the media. A full matrix measurement can provide more complete information on the system for studying and controlling light propagation. The first optical transmission matrix measurement of over 60,000 elements was demonstrated in [15].

They utilized an SLM to generate vectors in Hadamard basis, whose rows are mutually orthogonal and whose entries are either +1 or -1, to probe the disordered medium made of ZnO particles. With the transmission matrix, a scattering medium can act as a lens to image objects behind it. Though 60,000 is a large number of experimentally measured matrix elements, it is only a small fraction of the full transmission matrix with millions of elements. For an open complex photonic system such as disordered medium, a full transmission matrix has never been obtained.

Measuring transmission matrices has also been applied to MMFs. Because of the limited number of modes in MMFs, a complete matrix is accessible. A full transmission matrix of an MMF with 110 spatial and polarization modes has been measured [16]. The SLM generates LP modes and launches them into MMFs. The output modal field is decomposed into LP modes by another SLM. With the matrix, the linear propagation of light in the MMF is completely captured. For example, by inverting the matrix, desired output spatial patterns can be generated. As we will show in this thesis, by measuring frequency-dependent or polarization-dependent transmission matrices of MMFs, we are able to control temporal profiles and polarization states of light transmitted through MMFs. We are also able to study dynamic long-range correlations in MMFs with time-dependent transmission matrices.

1.3.2 Multimode-fiber-based spectrometers

Wavefront shaping accesses input spatial degrees of freedom in MMFs. Output spatial degrees of freedom, i.e., speckle patterns formed by multimode interference, embeds information in other domains at the input. For example, the coupling between degrees of freedom in spectrum and space enables an MMF to function as a compact, low-cost spectrometer to achieve ultra-high spectral resolution [17, 18]. In the absence of mode coupling, the spatial profile at the output of an MMF is $E(x, y, \omega) = \sum_n A_n \psi_n(x, y) \exp(-i\beta_n(\omega)L)$, where A_n is the complex coefficient de-

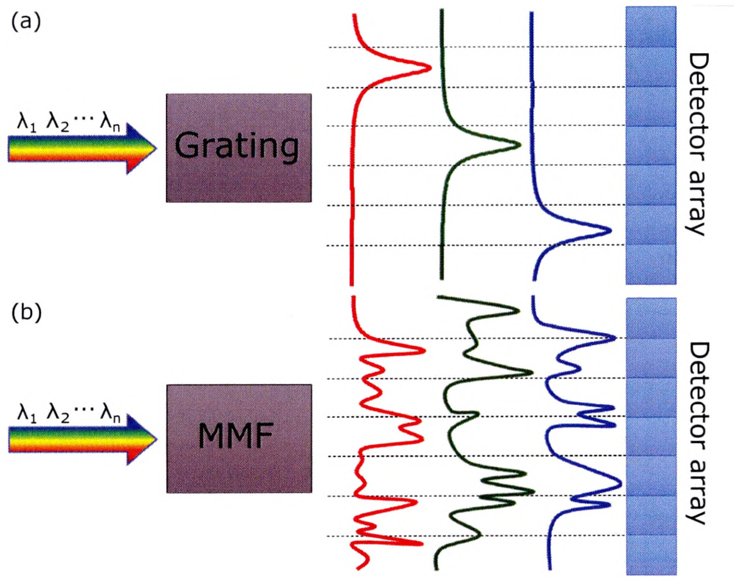

Figure 1.8: Operating principle of multimode-fiber-based spectrometers. (a) Traditional grating spectrometers perform one-to-one mapping from spectrum to space. (b) Multimode fiber spectrometers perform complex mappings from spectrum to space.

termined by the input wavefront and $\psi_n(x, y)$ is the electric field of mode n. The propagation constant $\beta_n(\omega)$ is dependent on frequency and so does the output spatial profile. When the input frequency is tuned, the phase term $\exp(-i\beta_n(\omega)L)$ changes and the interference between all the modes changes accordingly. Though the variation of β_n with frequency is small, the phase change can be remarkably amplified by the fiber length L. When the phase change is about 2π, a completely different speckle pattern is expected. The different spatial patterns at different frequencies can be used as the fingerprints to recover the input spectrum. The MMF basically performs a complex mapping from the spectral domain to space, drastically different from the one-to-one mapping in traditional grating-based spectrometers, as shown in Fig. 1.8.

In the multimode-fiber-based spectrometer, the response of the n^{th} detector is $x_n = M_{n1}a_{\lambda_1} + M_{n2}a_{\lambda_2} + ... + M_{nm}a_{\lambda_m}$, where m is the number of spectral channels.

Written in the matrix format, we have

$$\begin{bmatrix} x_1 \\ x_2 \\ \vdots \\ x_n \end{bmatrix} = \begin{bmatrix} M_{11} & M_{12} & \cdots & M_{1m} \\ M_{21} & M_{22} & \cdots & M_{2m} \\ \vdots & \vdots & \cdots & \vdots \\ M_{n1} & M_{n2} & \cdots & M_{nm} \end{bmatrix} \begin{bmatrix} a_{\lambda_1} \\ a_{\lambda_2} \\ \vdots \\ a_{\lambda_m} \end{bmatrix}. \tag{1.1}$$

The input spectrum $a_{\lambda_1} \cdots a_{\lambda_m}$ can be recovered from the simple matrix inversion. The number of spectral channels m that can be recovered is ultimately determined by the number of spatial channels n.

Soon after the concept of multimode fiber based spectrometer being demonstrated, modal dispersion in multimode fibers has been actively deployed for optical frequency comb spectroscopy [19] and hyperspectral imaging [20]. Though modal dispersion in MMFs has been notorious for its impairment of optical communication, it becomes beneficial for MMFs based spectrometers. A high spectral resolution can be achieved by using a longer fiber [18] or a fiber with stronger modal dispersion. From the square root relation between the fiber length and the DGD, it is also clear that mode mixing in an MMF reduces the spectral resolution. In chapter 3, we will show that by manipulating the input wavefront, we can obtain modes with large DGDs, which can be beneficial for MMFs based spectrometers.

Furthermore, in chapter 6 and 7 of this thesis, we will discuss a novel method of measuring not only the spectral amplitude but also the spectral phase of the signal with an MMF, and thus obtaining the temporal pulse shape in a single-shot measurement.

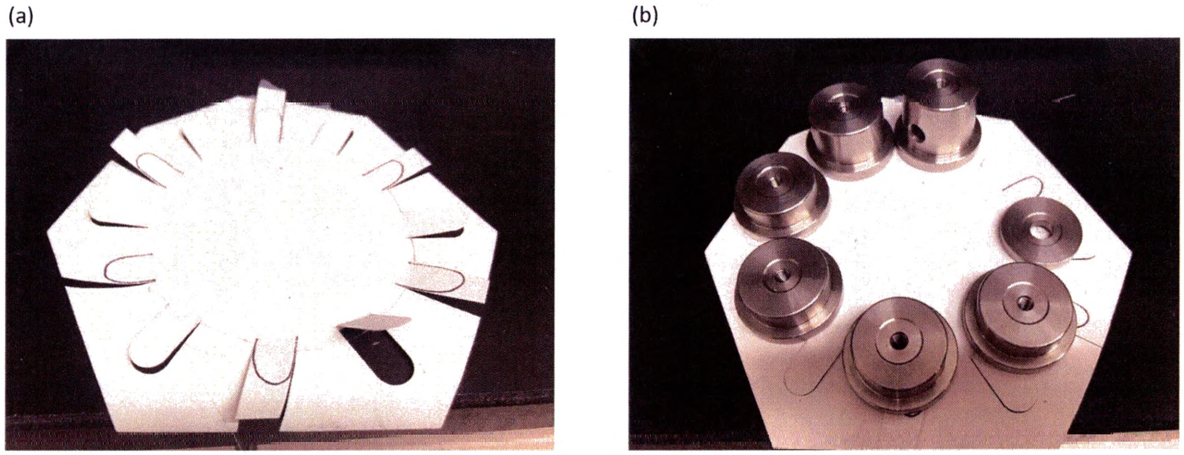

Figure 1.9: (a) A one-meter-long fiber is coiled to the paper clip. (b) Heavy load is put on top of the fiber coil to enhance mode coupling.

1.4 Introduce mode coupling in experiments

With advanced fiber fabrication technology, a multimode fiber usually does not present strong mode coupling. In this thesis, strong mode coupling is needed for studying fundamental physics and optical applications. The most effective way to introduce strong mode coupling is to create micro-bendings in the fiber.

We coiled the fiber on a paper clip as shown in Fig. 1.9(a). The deformable paper clip does not break the fiber and can create an abrupt distortion to the fiber. There are 12 clips and a one-meter-fiber can be coiled to 3 loops. To further enhance the mode-coupling, we put a heavy load on the top, as shown in Fig. 1.9(b). The load also stabilizes the coiled fiber. After coiling the fiber, we wait for 24 hours before doing experiments. During the 24 hours, the tension in the fiber can relax and the fiber coil becomes more stable. The effectiveness of our method of introducing mode coupling is demonstrated in chapter 5.

1.5 Mode-dependent loss model

Micro-bendings in multimode fibers not only introduce mode coupling but also mode-dependent loss. At the micro-bendings, guided light radiates out of the fiber. The leakage is stronger for higher-order modes, introducing mode-dependent loss. It is difficult to realistically model the radiation loss due to micro-bendings, because it depends on the specific geometry. In this thesis, we introduce a uniform material absorption loss to model it. The loss is $\exp(-\alpha\ell)$, where α is the absorption coefficient and ℓ is the length of the path light takes from the input to the output, which will be mode-dependent. Thus higher-order modes taking the longer paths suffer higher loss and it is the opposite for the lower-order modes. We can change the absorption coefficient to adjust the mode-dependent loss. In the experiment, we measure the transmission matrix of a multimode fiber and perform singular-value decomposition. Numerically, we adjust the absorption coefficient to fit the singular value distribution from the experiment.

1.6 Outline of this thesis

In this thesis, we exploit spatial degrees of freedom in multimode fibers for controlling light propagation and measuring properties of light.

In this chapter, we have introduced the basic concepts such as modal dispersion and different group delays in multimode fibers. We also briefly discussed how mode coupling in multimode fibers happens and how it can be modeled. We introduced the wavefront shaping technology widely used in disordered media to study and control light propagations in multimode fibers. The interference effect between different spatial modes gives rise to speckle patterns, with information such as the spectrum encoded into it. We showed an example of using speckle patterns generated by multimode fibers for spectroscopy to illustrate the potential applications of spatial degrees of freedom at the output of a multimode fiber.

In chapters 2, 3 and 4, we demonstrate spatiotemporal control with wavefront shaping. By controlling the spatial profile launched into the MMF, the temporal profile at the output can be tailored. In chapter 2, we experimentally demonstrate that principal modes can suppress modal dispersion and retain the temporal profile of optical pulses. However, principal modes have very narrow bandwidths, limiting its effectiveness for short pulses. In chapter 3, we find super-principal modes with nonlinear optimization algorithms. Super-principal modes outperform principal modes in terms of bandwidths. In chapter 4, we show a method to deliver the maximal energy of an optical pulse at arbitrary arrival times. This method is related but more general than principal modes or super-principal modes.

In chapter 5, we show that the polarization state at the output can also be controlled by wavefront shaping at the input. The coupling between spatial and polarization degrees of freedom makes an MMF reconfigurable waveplate.

From chapter 2 to chapter 5, we utilizes spatial degrees of freedom at the input of an MMF. In chapters 6 and 7, we focus on the spatial degrees of freedom at the output. We propose two novel methods of measuring ultrafast pulses in this part. With the speckle pattern formed at the end of the fiber, we recover not only the spectral amplitude but also the spectral phase, which enables recovery of temporal profiles of optical pulses. Chapter 6 describes a linear measurement scheme when a reference pulse is available. Chapter 7 describes a nonlinear characterization scheme when there are no reference pulses.

We summarize this thesis and discuss future prospects in chapter 8.

Bibliography

[1] K. Okamoto, Fundamentals of optical waveguides. Academic press (2006).

[2] R. J. Essiambre, G. Kramer, P. J. Winzer, G. J. Foschini and B. Goebel, Capacity limits of optical fiber networks, J. Light. Technol. **8**, 662-701 (2010).

[3] D. J. Richardson, J. M. Fini and L. E. Nelson, Space-division multiplexing in optical fibres, Nat. Photon. **7**, 354 (2013).

[4] K. P. Ho and J. M. Kahn, Statistics of group delays in multimode fiber with strong mode coupling, J. Light. Technol. **29**, 3119-3128 (2011).

[5] M. V. van Rossum and T. M. Nieuwenhuizen, Multiple scattering of classical waves: microscopy, mesoscopy, and diffusion, Rev. Mod. Phys. **71**, 313 (1999).

[6] W. Xiong, P. Ambichl, Y. Bromberg, B. Redding, S. Rotter and H. Cao, Principal modes in multimode fibers: exploring the crossover from weak to strong mode coupling, Opt. Express **25**, 2709-2724 (2017).

[7] A. P. Mosk, A. Lagendijk, G. Lerosey and M. Fink, Controlling waves in space and time for imaging and focusing in complex media, Nat. Photon. **6**, 283 (2012).

[8] S. Rotter and S. Gigan, Light fields in complex media: Mesoscopic scattering meets wave control, Rev. Mod. Phys. **89**, 015005 (2017).

[9] O. Katz, E. Small, Y. Bromberg and Y. Silberberg, Focusing and compression of ultrashort pulses through scattering media, Nat. Photon. **5**, 372 (2011).

[10] J. M. Kahn and D. A. Miller, Communications expands its space, Nat. Photon. **11**, 5 (2017).

[11] I. N. Papadopoulos, S. Farahi, C. Moser and D. Psaltis, Focusing and scanning light through a multimode optical fiber using digital phase conjugation, Opt. Express **20**, 10583-10590 (2012).

[12] A. M. Caravaca-Aguirre, E. Niv, D. B. Conkey and R. Piestun, Real-time resilient focusing through a bending multimode fiber, Opt. Express **21**, 12881-12887 (2013).

[13] M. Plöschner, T. Tyc and T. Čižmár, Seeing through chaos in multimode fibres, Nat. Photon. **9**, 529 (2015).

[14] I. M. Vellekoop and A. P. Mosk, Focusing coherent light through opaque strongly scattering media, Opt. Lett. **32**, 2309-2311 (2007).

[15] S. M. Popoff, G. Lerosey, R. Carminati, M. Fink, A. C. Boccara and S. Gigan, Measuring the transmission matrix in optics: an approach to the study and control of light propagation in disordered media, Phys. Rev. Lett. **104**, 100601 (2010).

[16] J. Carpenter, B. J. Eggleton and J. Schrder, 110x110 optical mode transfer matrix inversion, Opt. Express **22**, 96-101 (2014).

[17] B. Redding and H. Cao, Using a multimode fiber as a high-resolution, low-loss spectrometer, Opt. Lett. **37**, 3384-3386 (2012).

[18] B. Redding, M. Alam, M. Seifert and H. Cao, High-resolution and broadband all-fiber spectrometers, Optica **1**, 175-180 (2014).

[19] N. Coluccelli, M. Cassinerio, B. Redding, H. Cao, P. Laporta and G. Galzerano, The optical frequency comb fibre spectrometer, Nat. Commun. **7**, 12995 (2016).

[20] R. French & S. Gigan, Snapshot fiber spectral imaging using speckle correlations and compressive sensing, Opt. Express **24**, 32302-32316 (2018).

Chapter 2

Principal modes in multimode fibers

2.1 Introduction

[1]The temporal dynamics of wave scattering in complex systems has been widely studied in mesoscopic physics, nuclear physics, acoustics and optics. Most of these studies, e.g., electromagnetic or ultrasonic wave propagation in billiards [3–6], electron transport through quantum dots [7, 8], and light scattering in random media [9–14] focused on the statistics of delay times, i.e., eigenvalues of the Wigner-Smith time-delay matrix [15–17]. Despite innumerable trajectories the wave could take through an open complex system, an eigenstate of the Wigner-Smith matrix remarkably has a well-defined delay time. Largely in parallel, the Wigner-Smith eigenstates were introduced for multimode optical fibers (MMFs), which attracted much attention in recent years due to the rapid development of space-division multiplexing for telecommunications [18]. Inherent imperfections and external perturbations introduce random

1. This chapter is primarily based on the work published in ref. [1, 2]. W. Xiong performed the experiment and numerical simulations with the assistance from Y. Bromberg and B. Redding. P. Ambichl performed theoretical derivations. S. Rotter and H. Cao supervised the project.

coupling of the guided modes in the fiber and cause temporal broadening and distortion of transmitted pulses. As a generalization of principal states of polarization in a single-mode fiber [19], the Wigner-Smith eigenstates, also called principal modes (PMs) of MMFs, were proposed to suppress modal dispersion [20]. PMs retain their output spatial profiles to the first order of frequency variation [20]. Mathematically PMs are the eigenstates of the time-delay matrix $q \equiv -it^{-1}dt/d\omega$, where t is the field transmission matrix. In the absence of backscattering in the fiber, the group delay matrix coincides with the Wigner-Smith time-delay matrix, $Q \equiv -iS^{-1}dS/d\omega$, where S is the scattering matrix. Hence, PMs correspond to the Wigner-Smith time-delay eigenstates [6], and have well-defined delay times that are equal to the real part of the associated eigenvalues. These eigenstates provide the most suitable basis for studying and controlling temporal dynamics of total transmission through MMFs.

Advances in wavefront shaping techniques now make it possible to probe a single Wigner-Smith eigenstate in optics. Recently PMs were observed experimentally in a multimode fiber with weak mode coupling [21]. In this regime, mode coupling in the fiber is only perturbative and hence the PMs are similar to the eigenmodes of a perfect fiber. In the strong mode coupling regime, however, all modes are strongly mixed and the multiple scattering of light between different guided modes generates numerous paths for light to propagate through the fiber. It remains obscure how PMs are formed with well-defined delay times and what properties they possess in the presence of non-perturbative mode mixing. It is also unknown how PMs evolve from the weak to the strong mode coupling regime. In this chapter, we study PMs in an MMF with mode coupling and their transition from the weak to the strong mode coupling regime.

2.2 Time-delay operator and definition of principal modes

PMs have the property of vanishing frequency derivative of the output speckle pattern [22]. We approximate the output vector with a Taylor series up to first order, $\vec{\psi}(\omega) \approx \vec{\psi}(\omega_0) + d\vec{\psi}/d\omega|_{\omega=\omega_0}(\omega - \omega_0)$. In the next step, we demand the first order term in this series to be aligned to the zeroth-order term, which translates into the requirement that these two vectors are proportional to each other with a complex constant τ,

$$i\,\tau\,\vec{\psi}(\omega_0) = \frac{d\vec{\psi}}{d\omega}|_{\omega=\omega_0}. \tag{2.1}$$

Inserting the input-output relation $\vec{\psi}(\omega) = t(\omega)\,\hat{\phi}$ into Eq. (2.1) and rearranging the terms, we get

$$\begin{aligned} \frac{dt}{d\omega}|_{\omega=\omega_0}\hat{\phi} &= i\,\tau\,t(\omega_0)\;\hat{\phi} \\ -i\,t^{-1}(\omega_0)\,\frac{dt}{d\omega}|_{\omega=\omega_0}\,\hat{\phi} &= \tau\,\hat{\phi} \end{aligned} \tag{2.2}$$

It directly shows that an eigenvector of the Wigner-Smith time-delay operator

$$q = -i\,t^{-1}(\omega_0)\,dt/d\omega|_{\omega_0} \tag{2.3}$$

is a PM. The constant τ plays the role of the corresponding eigenvalue.

2.3 Experimental demonstration

2.3.1 Transmission matrix measurement

To construct the Wigner-Smith time-delay matrix, we measured the field transmission matrices of an MMF at multiple wavelengths. Figure 2.1 is a schematic of

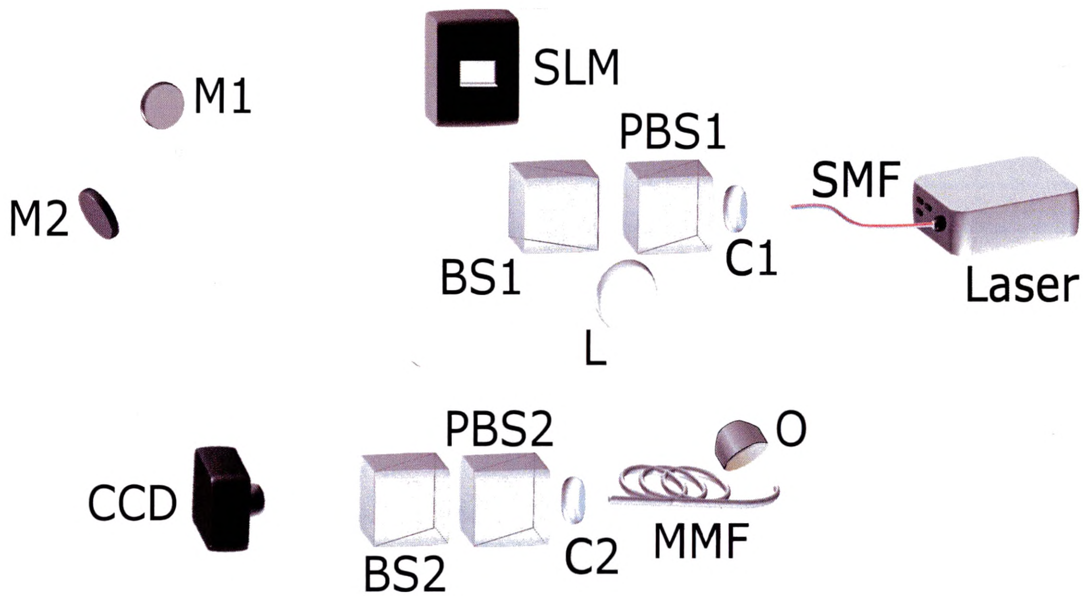

Figure 2.1: Experimental setup for measuring the field transmission matrix of an MMF. The continuous-wave output from a tunable laser source (Agilent 81940A) at wavelength $\sim$ 1550 nm is collimated (C1) and linearly polarized (PBS1). The beam is split into two arms by a beam splitter (BS1). In the fiber arm, light is modulated by the SLM in the reflection mode and then coupled to the MMF by a tube lens (L) and an objective (O). The output light from the MMF is collimated (C2) and linearly polarized (PBS2), before combining with the beam from the reference arm at a second beamsplitter (BS2). To match the optical path-length in the two arms, two mirrors (M1, M2) are inserted to the reference arm to adjust the path-length. BS2 is tilted to produce interference fringes of the two beams, which are recorded in the far-field by a CCD camera.

an interferometric setup. Input light is split into a fiber arm and a reference arm. The path-lengths of the two arms are matched. A spatial light modulator (SLM) in the fiber arm prepares the phase front of the light field, which is then imaged to the front facet of an MMF. The output from the fiber combines with the reference beam and forms interference fringes. From the interferogram, we extract the spatial distribution of the transmitted field through the fiber. The measured intensity is $I = |E_r|^2 + |E_s|^2 + E_r^* E_s e^{ikr\sin\theta} + E_r E_s^* e^{-ikr\sin\theta}$, where E_r and E_s are the electric fields of the reference arm and the fiber arm, respectively, and θ is the tilt angle between them. The first two terms represent the dc components, and the last two terms are modulated at the spatial frequency $\pm k\sin\theta$. These terms can be separated in the Fourier domain, namely, by performing the spatial Fourier transform. By applying a Hilbert filter, we select only the third term that has the positive spatial frequency, then remove the factor $e^{ikr\sin\theta}$ before applying an inverse Fourier transform to obtain the amplitude and phase of E_s. The transmission matrix is measured in momentum space. The SLM scans the incident angle of light onto the fiber facet, and the transmitted light is measured in the far-field of the distal tip.

In Chapter 1, we explained how the mode coupling is introduced. By adjusting the load we put on the fiber coil, we can tune the coupling strength. To evaluate the strength of mode coupling in the fiber, the transmission matrix is transformed into the mode basis by decomposing the input and output fields by linearly polarized modes, which are simply referred to as modes below. Figure 2.2 shows the amplitude and phase of the measured transmission matrices of the MMF. Without external stress, the field transmission matrix is nearly diagonal [Fig. 2.2(a)]. The small off-diagonal terms result from weak mode coupling due to the inherent imperfection and macro-bending of the fiber. With an increase in the stress applied to the fiber, the off-diagonal terms grow and eventually become comparable to the diagonal terms, as shown in Fig. 2.2(c). Hence, in the weak coupling regime, only modes with similar propagation

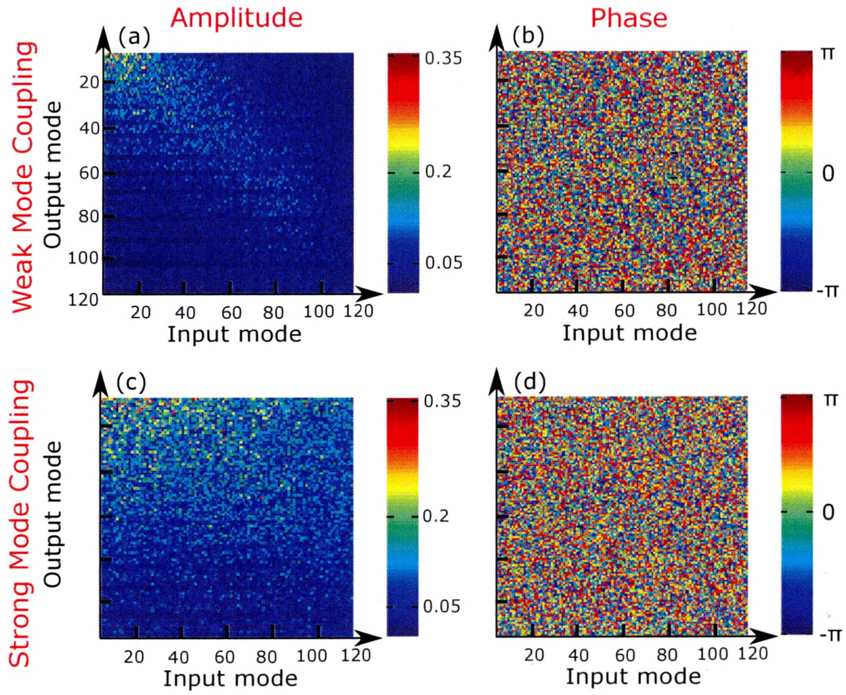

Figure 2.2: Field transmission matrix of an MMF with weak (a,b) and strong mode coupling (c,d). The one-meter-long step-index fiber has a 50 μm core and a numerical aperture of 0.22. There are about 120 guided modes for one polarization, which are labeled by the propagation constant (from large to small). Amplitude (a,c) and phase (b,d) of the measured transmission matrix at $\lambda = 1550$ nm ($\omega = 194$ THz) for one linear polarization. The transmission matrix is nearly diagonal in (a), indicating weak coupling among modes of similar propagation constants. In (c) all modes are coupled, although higher-order modes have more attenuation.

constants are coupled. However, in the strong coupling regime, light diffuses to all modes regardless of which mode it is injected. Greater loss results in a lower amplitude of higher-order modes at the output. However, if higher-order modes are launched into the fiber, they can be scattered to lower order modes which experience less attenuation and dominate the output fields. Consequently, the transmission matrix presents a stronger decay for the output modes of high-order than the input ones. The phases of the transmission matrix elements are randomly distributed for 0 and 2π, reflecting the random nature of the mode coupling in the MMF.

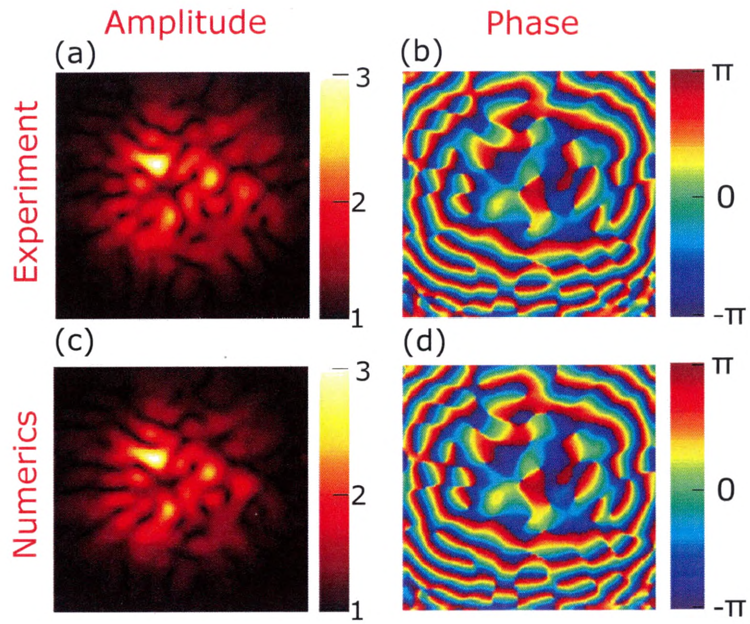

Figure 2.3: Experimentally measured (a,b) and numerically calculated (c,d) amplitude and phase of the output field of a PM in the same fiber as in Fig. 2.2. The agreement confirms the accuracy of the transmission matrix measurement.

2.3.2 Experimental demonstration of principal modes

After measuring the transmission matrices at multiple wavelengths, we construct the Wigner-Smith time-delay matrix $q \equiv -it^{-1}dt/d\omega$. An eigenvector of q gives the input field for a PM. We generate the input waveform of the principal mode by the SLM and launch it to the fiber. Since the SLM is limited to phase-only modulation, a complex-to-phase coding technique is used to convert the computer-generated phase-only hologram to a complex function with amplitude and phase modulation [23]. Figure 2.3(a,b) depict the measured amplitude and phase of the output field pattern Ψ for a PM. For comparison, we also calculate the output field $\mathbf{\Psi'}$ from the input field of the same PM using the measured transmission matrix [Figure 2.3(c,d)]. To quantify their difference, we compute $\int |\mathbf{\Psi} - \mathbf{\Psi'}|^2 \mathbf{dr}$, with $\int |\mathbf{\Psi}|^2 \mathbf{dr} = \mathbf{1}$ and $\int |\mathbf{\Psi'}|^2 \mathbf{dr} = \mathbf{1}$. The difference is 3.8%, confirming the accuracy of our experimental measurement.

We note that the transmission matrix is measured for one linear polarization of input and output light only. Since the polarization is scrambled in the MMF, some of the input light is converted to the other polarization and thus is not measured at the output. The transmission matrix is non-unitary even without intrinsic loss, and it is part of the full transmission matrix for both polarizations. Nevertheless, we can still obtain the time-delay matrix for one polarization from the partial transmission matrix. Its eigenstate gives the linearly-polarized input waveform that generates an output field whose one polarization component has a frequency-invariant spatial profile. Below we study the characteristics of such polarized PMs, which are simply referred to as PMs.

We first experimentally investigate the differences in PMs of the MMF with weak and strong mode coupling. Figure 2.4(a-c) shows the far-field patterns of three PMs in the weak mode coupling regime with short, medium and long delay times. The PM with short delay time has small transverse momentum, similar to the low-order modes [Fig. 2.4(a)]. With increasing delay time, the PM acquires larger transverse momentum [Fig. 2.4(b)]. The far-field pattern of the PM with long delay time consists of large transverse momentum, like the high-order modes [Fig. 2.4(c)]. We decompose the output field pattern by the LP modes, and the coefficients are given in Fig. 2.4(d-f). The PM with short/medium/long delay time is composed mostly of low/medium/high-order modes. Clearly, in the weak mode coupling regime, each PM contains only a few modes with similar propagation constants.

Figure 2.5(a-c) plots the spatial distribution of the output field amplitude for three PMs with short, medium and long delay time in the case of strong mode coupling. The far-field patterns contain many transverse momentum components and do not resemble any modes of the perfect fiber. The modal decomposition verifies that these PMs are a superposition of many LP modes [Fig. 2.5(d-f)]. Since higher-order modes experience more attenuation, their contributions to PMs, especially to the ones with shorter delay times, are reduced. To be more quantitative, we define the mode participation number as $N_e \equiv (\sum_n |\alpha_n|^2)^2/(\sum_n |\alpha_n|^4)$, where α_n is the decomposition

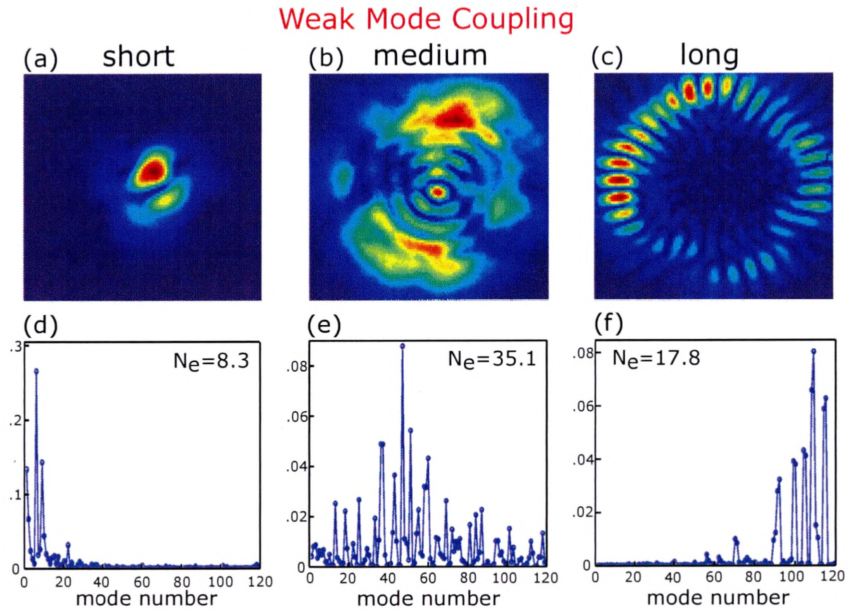

Figure 2.4: PMs in the weak mode coupling regime. (a-c) Spatial distribution of the far-field amplitude for three PMs in the weak mode coupling regime with short (a), medium (b) and long (c) delay time. (d-f) Decomposition of output fields in (a-c) by the LP modes. The PMs with short/medium/long delay time are composed mostly of low/medium/high-order LP modes. N_e is the mode participation number.

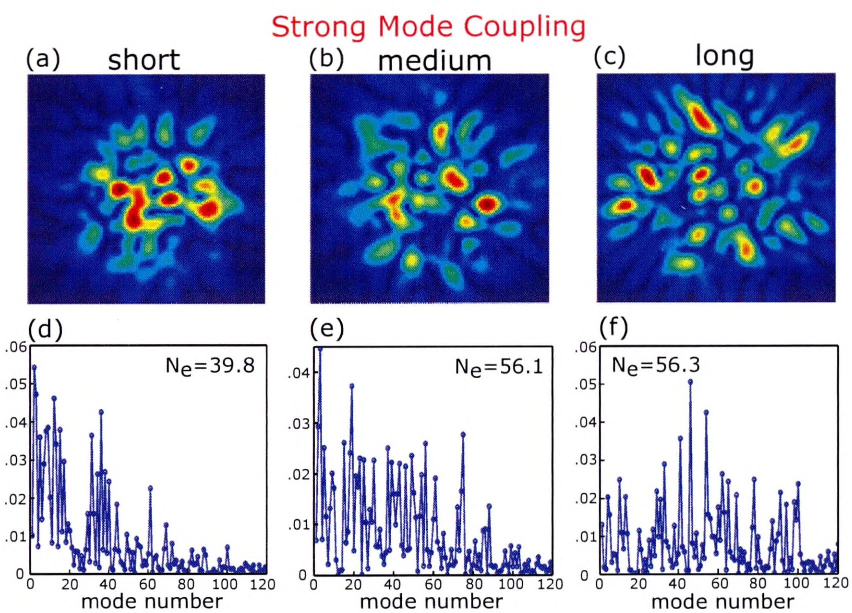

Figure 2.5: PMs in the strong mode coupling regime. (a-c) Spatial distribution of the far-field amplitude for three PMs in the strong mode coupling regime with short (a), medium (b) and long (c) delay time. (d-f) Modal decomposition of output fields in (a-c), revealing the PM is a superposition of many LP modes. N_e is the mode partition number.

coefficient for the n-th mode. As noted in Figs. 2.4 and 2.5, the values of N_e for the PMs in the weak mode coupling regime are significantly smaller than those in the strong mode coupling regime.

2.4 Spectral and temporal properties

2.4.1 Spectral property

To investigate the spectral property of PMs, we scan the frequency ω while keeping the input field pattern to that of a PM at ω_0. The output field pattern is measured at each frequency and compared to that at ω_0. Figure 2.6(a) shows the far-field patterns of a PM in the strong mode coupling regime at three frequencies (top row), and they are nearly identical. For comparison, a random superposition of modes at the input results in different output profiles at these three frequencies [bottom row of Fig. 2.6(a)]. This striking difference illustrates that the output field pattern of the PM decorrelates much slower with frequency.

To be more quantitative, we calculate the spectral correlation function $C(\Delta\omega \equiv \omega - \omega_0) \equiv |\mathbf{\Psi}(\omega_\mathbf{0} + \mathbf{\Delta}\omega) \cdot \mathbf{\Psi}(\omega_\mathbf{0})| = \cos[\theta(\mathbf{\Delta}\omega)]$, where $\mathbf{\Psi}$ is a vector representing the output fields in all spatial channels with its magnitude normalized to unity. θ is the angle between the two vectors at different frequencies. As shown in Fig. 2.6(b), $C(\Delta\omega)$ for the PM is significantly larger than that for the random input. It displays a broad plateau at $\Delta\omega = 0$. Thus the output field of a PM still de-correlates as a result of a frequency shift, leading to a finite bandwidth. To understand the shape of the correlation curve, we analyze the derivatives of $C(\Delta\omega)$. The first-order derivative of $C(\Delta\omega)$ with respect to $\Delta\omega$ is

$$\frac{dC(\Delta\omega)}{d\Delta\omega} = -\sin[\theta(\Delta\omega)]\frac{d\theta(\Delta\omega)}{d\Delta\omega}.$$

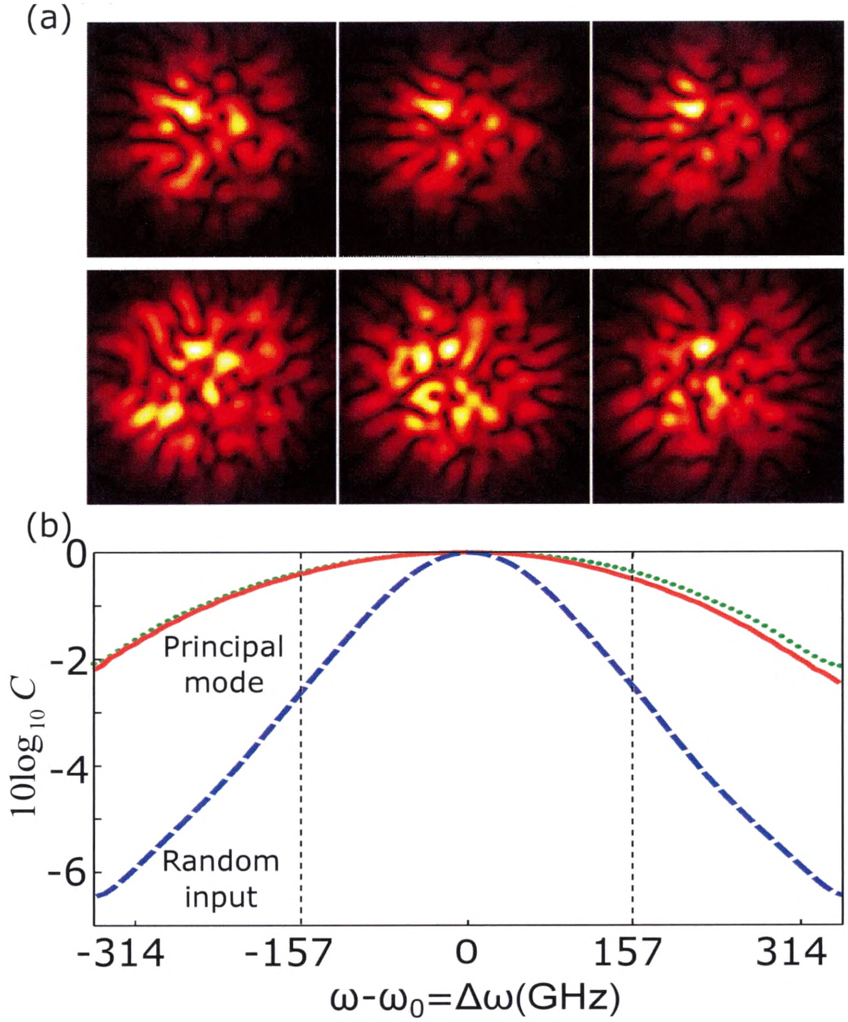

Figure 2.6: Spectral property of PMs in an MMF with strong mode coupling. (a) Output field amplitude for the input wavefront of a PM in the strong mode coupling regime with short delay time at $\omega_0 = 1219$ THz (top row), or a random superposition of linearly polarized modes (bottom row). The input frequency is $\omega - \omega_0 = -157$ GHz (left column), 0 (middle column), and 157 GHz (right column). The output field patterns for the PM input are similar while those for random input are totally different. (b) Spectral correlation function $C(\Delta\omega)$ of the output field pattern, measured experimentally for a PM (red solid curve) or calculated from the measured transmission matrix and input spatial profile of the same PM (green dotted curve). For comparison, $C(\Delta\omega)$ for a random input is also shown (blue dashed curve). $C(\Delta\omega)$ is normalized to one at $\Delta\omega = 0$. Its value decreases to 0.9 at $\Delta\omega = 338$ GHz for the PM and 173 GHz for the random input. The agreement between the red and green curves illustrates the accuracy of the measurement.

At $\Delta\omega = 0$, $\theta(\Delta\omega) = 0$ and $\sin[\theta(\Delta\omega)] = 0$. Thus the first-order derivative of the spectral correlation function vanishes for any input field. The second-order derivative of $C(\Delta\omega)$ is

$$\begin{aligned}\frac{d^2C(\Delta\omega)}{d\Delta\omega^2} &= -\cos[\theta(\Delta\omega)]\left[\frac{d\theta(\Delta\omega)}{d\Delta\omega}\right]^2 \\ &\quad -\sin[\theta(\Delta\omega)]\frac{d^2\theta(\Delta\omega)}{d\Delta\omega^2}\end{aligned}$$

At $\Delta\omega = 0$, the second term on the right hand side vanishes, and $\cos[\theta = 0] = 1$ in the first term, giving $C''(\Delta\omega = 0) = -[\theta'(\Delta\omega = 0)]^2$.

For a PM, the output field pattern is invariant with frequency to the first order, i.e., $\theta'(\Delta\omega = 0) = 0$. Thus the second-order derivative of the spectral correlation function vanishes, $C''(\Delta\omega = 0) = 0$. For a random input field, $\theta'(\Delta\omega = 0)$ does not vanish, and hence $C''(\Delta\omega = 0)$ is nonzero. Consequently, the spectral decorrelation of PMs is much slower than that of a random input, leading to a plateau of the correlation curve, that is absent for the random input. We note that C'' vanishes only at ω_0, not at nearby frequencies for a PM. Moreover, the third-order derivatives are non-zero even at ω_0. Thus the output field of a PM still de-correlates as a result of a frequency shift, leading to a finite bandwidth.

2.4.2 Temporal dynamics

In the next step we probe the temporal dynamics of a single PM. Like other open chaotic systems, the transmission of a pulse through an MMF with strong mode coupling involves spatial and temporal distortions. Strong mode mixing results in hopping of the light among modes with different propagation constants. Thus the light can take many paths of varying lengths through the fiber. The output in each spatial channel (e.g. speckle grain) is a sum of waves with different paths, each associated with a respective time delay, leading to temporal broadening and distortion of the

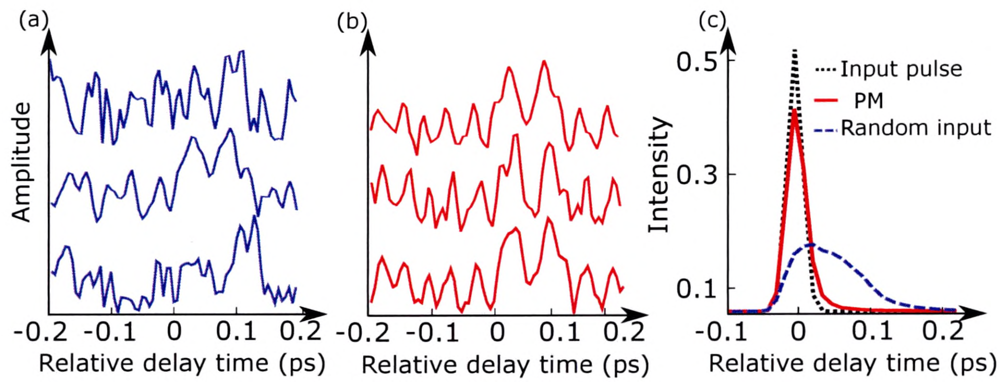

Figure 2.7: Temporal property of PMs in an MMF with strong mode coupling. (a,b) Temporal variation of the output field amplitude in three spatial channels (three speckles grains) when an optical pulse is launched into a random superposition of fiber modes (a) or a PM in the strong mode coupling regime at $\omega_0 = 194$ THz (b). The spatial profile of the output field is recorded in a frequency range of 400 GHz with a step size of 2.5 GHz. The Fourier transform is then performed to obtain the field evolution in time. The horizontal axis is the relative delay time, obtained by subtracting the average delay time for random input fields. The temporal traces of individual spatial channels are totally different for the random input, but nearly identical for the PM input. (c) Spatially integrated intensity of the input (black dotted curve) and the output pulses when a Gaussian pulse is injected to the MMF with random spatial profile (blue dashed curve) or with the profile of a PM (red solid curve).

input pulse. Typically, the temporal trace varies from one channel to another, since the combination of paths differs. This is confirmed by simulating the propagation of a pulse, $\phi(t) = \int \phi(\omega)\, e^{-i\omega t} d\omega$, with a field spectrum $\phi(\omega)$. The pulse is launched into a random superposition of modes at the input of the fiber, and the output field patterns are recorded experimentally as a function of frequency. We perform the Fourier transform to obtain the temporal evolution of the output field in each spatial channel. Figure 2.7(a) shows the temporal traces of field magnitude in three spatial channels. They are very different from each other, due to strong mode scrambling in the fiber.

However, if the input light is coupled to a PM, the output fields in different spatial channels are synchronized, as shown in Fig. 2.7(b). This is a direct consequence of the invariance of the output field pattern with frequency. Specifically, the output field vector at frequency ω can be written as $\mathbf{\Psi}(\omega) = \phi(\omega)t(\omega)\mathbf{\Phi}$, where the input field vector $\mathbf{\Phi}$ corresponds to a PM at ω_0. If the input bandwidth is less than the spectral correlation width of the PM, $t(\omega)\mathbf{\Phi} \approx \alpha(\omega)\hat{\mathbf{\Psi}}_0$, where $\hat{\mathbf{\Psi}}_0$ is a unit vector representing the normalized output field profile for the PM at ω_0, and $\alpha(\omega)$ is a complex number that may vary with frequency. The Fourier transform of $\mathbf{\Psi}(\omega)$ gives the output field vector $\mathbf{\Psi}(\tau) = \tilde{\phi}(\tau)\hat{\mathbf{\Psi}}_0$, where $\tilde{\phi}(\tau) = \int \phi(\omega)\alpha(\omega)e^{-i\omega\tau}d\tau$ represents the output pulse shape. Hence, the spatial and temporal variations of the output field become decoupled for the PM. The temporal traces in all output channels are identical up to a constant factor given by the elements of $\hat{\mathbf{\Psi}}_0$. The spatial profile of the output field remains constant in time, allowing the spatial and temporal distortions to be corrected separately. For example, the output pulse shape can be tailored by modulating the spectral phase of the input spectrum $\phi(\omega)$. Since the output fields are spatially coherent, a spatial mask can convert the output to any desired pattern or focus to a diffraction-limited spot.

Let us consider a simple case, $\alpha(\omega) \simeq \alpha_0 e^{i\eta(\omega)}$, where α_0 is a constant amplitude and the phase $\eta(\omega) \simeq \eta(\omega_0) + \eta_0' (\omega - \omega_0)$, where η_0' is the value of $d\eta/d\omega$ at ω_0. Then the output pulse, $\tilde{\phi}(\tau) \propto \phi(\tau - \eta_0')$, has the same temporal shape as the input one. This is confirmed by synthesizing a pulse with Gaussian spectrum and flat phase at the input. The output intensity, summed over all spatial channels, is plotted in Fig. 2.7(c) together with the input pulse intensity. The output pulse has negligible broadening and shape distortion, despite strong mode coupling in the fiber. In contrast, the same pulse, but with a random input pattern, suffers from severe broadening as seen in Fig. 2.7(c). PMs can thus compensate for the temporal distortion induced by modal dispersion in an MMF.

2.5 Principal mode bandwidth

The unique spectral and temporal properties of PMs hold in both weak and strong mode coupling regimes. However, the properties are only true within a finite frequency range. It is hence important to determine the bandwidth of PMs. To be quantitative, we define the PM bandwidth $\Delta\omega_c$ as the frequency range over which $C \geq 0.9C(0)$. Since the spectral decorrelation of the output pattern for any input waveform depends on fiber properties, such as the fiber length and numerical aperture, we plot the enhancement ratio of the bandwidth of PMs to the bandwidth of random inputs noted as normalized bandwidth. Figure 2.8 plots the correlation function and the normalized $\Delta\omega_c$ for all PMs versus their delay times. In the weak mode coupling regime, the PM bandwidth first drops sharply with increasing delay time, then levels off. In the strong mode coupling regime, $\Delta\omega_c$ remains nearly constant at short delay time, and starts decreasing as the delay time becomes larger. The normalized bandwidths of PMs in the weak mode coupling regime are larger than those in the strong mode coupling regime, indicating the enhancement of PMs is more profound in the weak mode coupling regime.

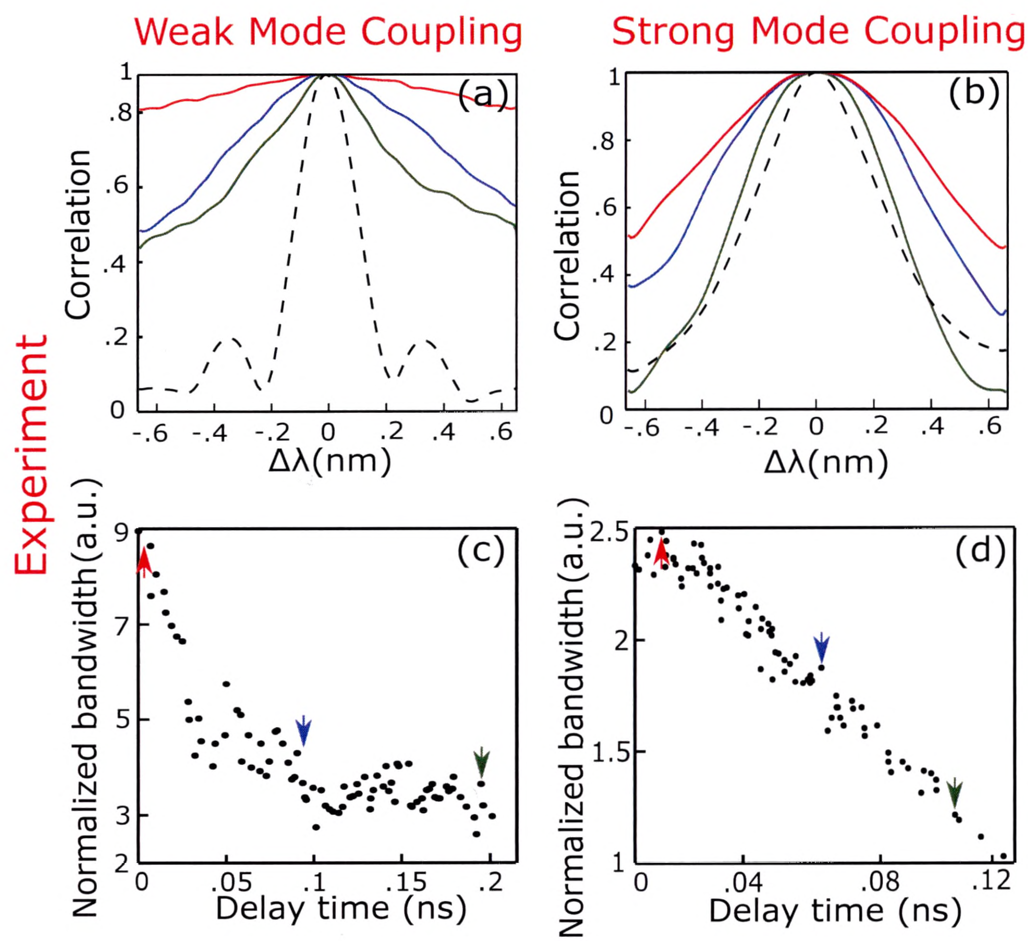

Figure 2.8: Spectral decorrelation of PMs. (a,b) Spectral correlation function $C(\Delta\omega)$ of the output field pattern, measured experimentally for three PMs with short delay time (red line), medium delay time (blue line) and long delay time (green line) in the MMF with weak (a) and strong (b) mode coupling. For comparison, $C(\Delta\omega)$ for a random input is also shown (black dashed curve). $C(\Delta\omega)$ is normalized to one at $\Delta\omega = 0$. The output field pattern for the PM with short delay time decorrelates more slowly with frequency than that with long delay time. (c,d) Normalized spectral correlation width of PMs vs. delay times in weak (c) and strong (d) mode coupling regime. The red, blue and green arrows indicate the PMs of which the three spectral correlation curves plotted in (a) and (b).

To understand what determines the bandwidths of PMs in the MMFs with weak and strong mode coupling, we perform numerical simulations using the concatenated fiber model [24]. In particular, we consider a one-meter-long step-index fiber with 50 μm core and 0.22 numerical aperture. The fiber is divided into 20 short segments; light propagates in each segment as in a perfect fiber without mode coupling. Between adjacent segments, the guided modes are randomly coupled. The scattering in the mode space is simulated by a unitary random matrix, which is given by $A = \exp[iH]$, where H is a random Hermitian matrix. We construct $H = G \cdot (R + R^{\dagger})$, in which R is a complex random matrix whose elements are taken from the normal distribution, and G is a real matrix imposing a Gaussian envelope function on the matrix elements along the off-diagonal direction. Specifically, the magnitude of the matrix elements decays away from the diagonal, and the decay rate, i.e., the width of the Gaussian envelope function, depends on the degree of mode coupling. The faster the decay, the narrower the envelope function and the weaker the mode coupling. Therefore, by varying the width of the Gaussian envelope function, we can tune the scattering strength in mode space.

To quantify the amount of scattering in mode space, we calculate the effective transport mean free path ℓ, which is given by the propagation distance beyond which the relative intensity distribution in each mode no longer changes [25, 26]. In the concatenated fiber model, the transport mean free path is obtained numerically by launching light into a single mode and computing the number of segments light propagates until all modes are equally populated. The coupling strength is described by the ratio of the fiber length L to the effective transport mean free path ℓ.

First, we ignore the fiber loss and calculate the normalized bandwidths of PMs in the MMF with different degrees of mode coupling. In the weak-coupling limit ($L/\ell \ll 1$), the normalized bandwidth has two maxima at the shortest delay time and the longest delay time [Fig. 2.9(a)]. As the mode coupling (L/ℓ) increases, the

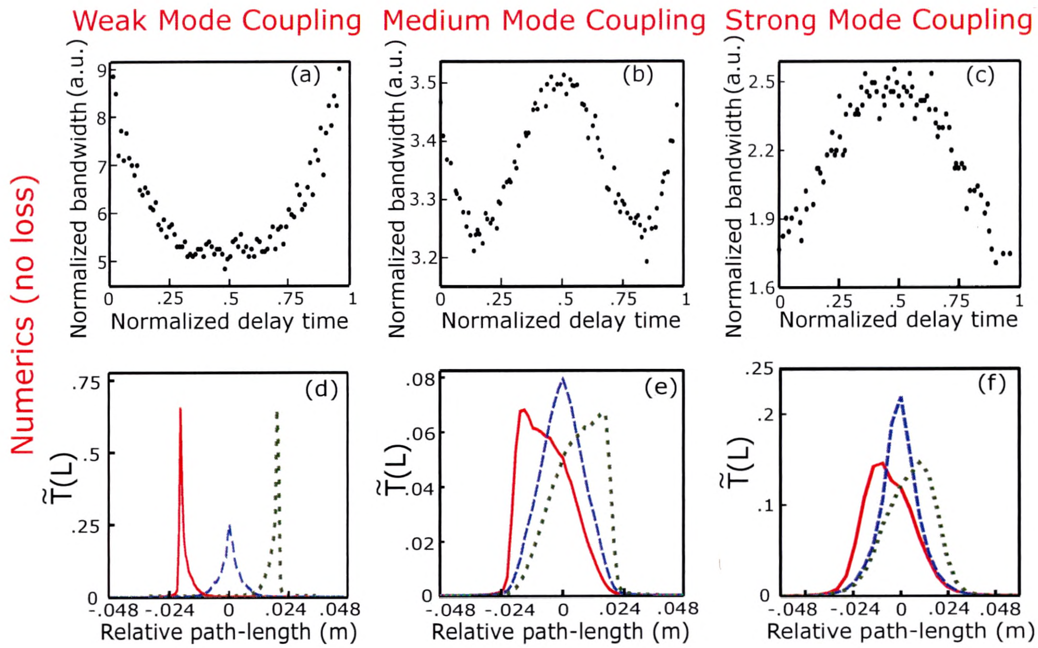

Figure 2.9: Calculated PM bandwidths (upper row) and corresponding path-length distributions (lower row). The MMF is a step-index fiber with 50 μm core and 0.22 numerical aperture. The mode coupling strength (L/ℓ) is 0.2 in (a,d), 1.0 in (b,e), and 10 in (c,f). (a,b,c) PM bandwidths vs. delay times. The bandwidth is normalized to the average width of random inputs. The shortest delay time is set to be 0 and the difference between the shortest and longest delay time is normalized to 1. (d,e,f) The intensity distributions over the relative path-length of the PMs in (a,c,e) with the delay time = 0 (red solid line), 0.5 (blue dashed line) and 1 (black dotted line). In the weak mode coupling regime (a), the PM bandwidth is maximized at the shortest and longest delay time. In the strong mode coupling regime (c), the PM bandwidth is the largest at the medium delay time. (b) shows the transition between the two regimes.

normalized bandwidths of all the PMs are reduced. However, the decrease at the medium delay time is slower than that at short and long delay times. Consequently, a new maximum arises at the medium delay time when ($L/\ell \simeq 1$) [Fig. 2.9(b)]. With a further increase of mode coupling, the two local maxima at the shortest and longest delay times disappear entirely [Fig. 2.9(c)]. Thus the variation of the bandwidth with the delay time in the strong mode coupling regime ($L/\ell \gg 1$) is just opposite to that in the weak mode coupling regime.

2.5.1 Physical understanding

To interpret these results, we resort to an intuitive picture of optical paths in the MMF. An MMF supports many propagating modes, each having a different propagation constant. From the geometrical-optics point of view, various rays propagate down the fiber at different angles relative to the axis of the fiber, and thus travel different distances and experience different phase delays. Inherent imperfections and external perturbations result in light hopping among the trajectories with different angles and lengths. Hence, light can take many paths of different lengths to transmit through the fiber. The sum of waves following different paths gives the output field. Formally, this fact can be expressed by writing the transmission amplitude $t_{nm}(\Delta\omega)$ from an incoming mode m and an outgoing mode n at frequency $\Delta\omega$ (central frequency is set to zero) through a sum over infinitely many paths p, each of which contributes with an amplitude A_p and with a phase that depends on the path length L_p in the following way: $t_{nm}(\Delta\omega) = \sum_p A_p \exp(i\Delta\omega L_p/c)$ [27]. This relation follows directly from the Feynman path integral formulation of the Green's function, for which several semiclassical approximations have been worked out (see [28] for an overview). The interesting insight that we now deduce from this path picture is that in the weak guiding approximation one can deduce the path spectrum $\tilde{t}_{nm}(L)$ contributing to the transmission amplitude $t_{nm}(\Delta\omega)$ by a simple Fourier transform $\tilde{t}_{nm}(L) = \int_{k_{\min}}^{k_{\max}} dk\, t_{nm}(k) \exp(-ikL)$ [29], where we define $k = \Delta\omega/c$. Correspondingly, the power spectrum of the total transmission through the fiber is given as $\tilde{T}(L) = \sum_{n,m} |\tilde{t}_{nm}(L)|^2$.

The width of the intensity distribution over the path-length spectrum determines how fast the output field decorrelates with frequency. The narrower the distribution, the weaker the dephasing among different paths, and the slower the decorrelation. We calculate $\tilde{T}(L)$ for the PMs in different mode coupling regimes. Figure 2.9(d,e,f) presents the results for three PMs with the shortest, intermediate, and longest delay times. In the case of weak mode coupling, the intensity distribution over the path-length is narrow [Fig. 2.9(d)] because each PM contains only a few modes with similar propagation constants. For example, the PM with short delay time consists of a few low-order modes. The adjacent modes that these low-order modes can couple to are higher-order modes with smaller propagation constants. However, the PM with intermediate delay time is composed of modes with medium propagation constants, which are surrounded by both lower and higher-order modes to which they can couple to. Since the propagation constants of modes in a step-index fiber are almost equally spaced, the constituent modes for an intermediate PM have more neighboring modes to couple to, and the intensity distribution over the path-length is wider than that for the fast PM. Consequently, the fast PM has a broader bandwidth than the intermediate PM. The same argument applies to the slow PM that has a long delay time. Therefore, the fastest and slowest PMs have the maximum bandwidth.

As the mode coupling strength increases gradually, the intensity distribution over the path-length is broadened [Fig. 2.9(e)], and the normalized bandwidth of PMs is reduced. Eventually all modes are coupled, and the transition from single scattering to multiple scattering occurs in mode space. Since light can follow many possible trajectories of the same length from the input to the output of the fiber, the interference of the fields from these paths determines the intensity distribution over the path-length. In Fig. 2.9(f), the fast PM has intensity concentrated on shorter paths, as the destructive interference of different trajectories with the same length makes $\tilde{T}(L)$ is merely pronounced for longer path-length. The opposite happens to the slow PM. Quite remarkably, Such interference effects are completely determined by the input wavefront. PMs with intermediate delay times suppress both short and long paths by a destructive interference. In the absence of mode-dependent loss, the central-limit-theorem dictates that the density of path-lengths has a Gaussian distribution that is peaked at the medium delay time. Thus the intermediate PMs, whose delay times coincide with or are close to the medium path-length of maximal density, only need to suppress a small number of trajectories of short or long path-lengths via interference. By contrast, the PMs with short delay times require a destructive interference of both medium and long paths. Since there are more trajectories with medium path-length, it is more difficult to suppress them via interference, as evident from the shoulder at medium path-length for the fast PM in Fig. 2.9(e). Hence, the fast PMs have broader path-length distributions and narrower bandwidths than the medium PMs. The same explanation applies to the bandwidths of the slow PMs.

It is now clear that the well-defined delay times of PMs are formed by multi-path interference. In the weak mode coupling regime, the PMs are formed by modes with similar propagation constants because these modes have similar path-lengths. In the strong mode coupling regime, the multi-path interference effect becomes more important. By controlling the input wavefront, light is selectively coupled into paths with similar path-lengths, though they manifest different modes at the input.

2.5.2 Effect of mode-dependent loss

The numerical study in the last subsection assumes no loss in the fiber. However, loss is common in an MMF. The loss is mainly from the scatterings at micro-bendings in the fiber, and it is usually greater for higher-order modes, as we illustrated in Chapter 1. In this section, we investigate the effects of mode-dependent loss (MDL) on PMs. In the concatenated fiber model, we introduce a uniform absorption coefficient to each segment of the fiber. Higher-order modes that have longer transit time thus experience more loss.

We compare the PM bandwidth with MDL to that without MDL in Fig. 2.10. In the weak mode coupling regime, MDL significantly reduces the bandwidth of PMs with long delay times, as indicated by the arrow in Fig. 2.10(a). In contrast, the bandwidth of PMs with short delay times are nearly unchanged by the MDL. This

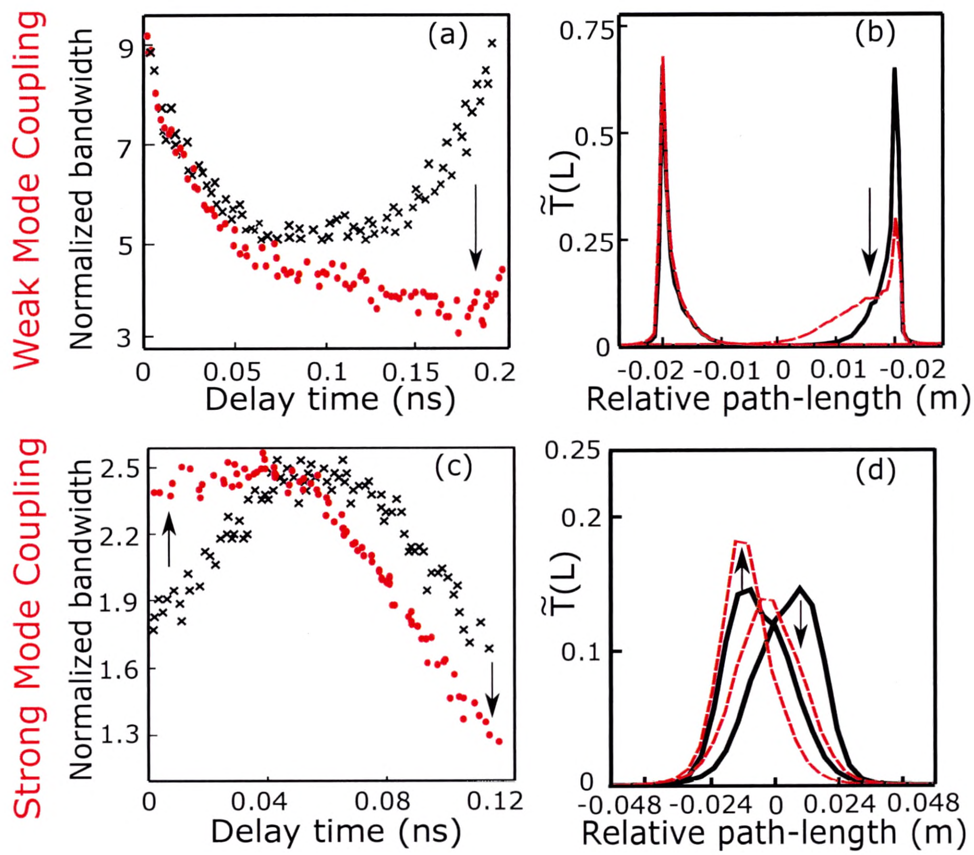

Figure 2.10: Effects of MDL on PM bandwidths and path-length distributions. (a) Normalized bandwidths of PMs in the weak (a) and strong (c) mode coupling regimes with (red dots) or without (black crosses) MDL. (b,d) Calculated intensity distributions over the path-length of PMs in (a,c) with delay time = 0, 0.2 ns in (b) and 0, 0.12 ns in (d) with (red dashed) or without (black solid) MDL. In the weak coupling regime, the MDL reduces significantly the bandwidth of slow PMs (a) by broadening their path-length distributions (b). In the strong coupling regime, the MDL enhances the bandwidth of fast PMs (c) by narrowing their path-length distribution (d).

behavior can be explained by the change in the intensity distribution over the path-length $\tilde{T}(L)$. The slow PM is composed of long paths, and the stronger attenuation of the longer paths broadens the distribution, as shown in Fig. 2.10(b). Consequently, the bandwidth of the PM with long delay time is reduced. The fast PM, by contrast, consists of short paths, which experience little loss, thus $\tilde{T}(L)$ remains almost the same, and with it also the bandwidth of the PM. The longer the delay time, the stronger the effect of MDL, and the greater the reduction in the PM bandwidth.

In the strong mode coupling regime, the MDL enhances the bandwidth of a PM with short delay time, while reducing the bandwidth of PM with long delay time [Fig. 2.10(c)]. Since the fast PM has a broader path-length distribution than that in the weak mode coupling regime, the MDL suppresses the longer paths and narrows the distribution that centers on the short path-length [Fig. 2.10(d)]. In contrast, the path-length distribution for the slow PM, which centers on the long path-length, is broadened by the MDL, as the shorter paths experience less attenuation than the longer ones. The variations of the PM bandwidth with the delay time in both weak and strong coupling regimes agree qualitatively with the experimental results in Fig. 2.8(b,d). We may thus conclude that MDL has a significant impact on the bandwidths of PMs and needs to be taken into account to understand the experimental data.

2.5.3 Transition from weak to strong mode coupling

We further analyze the transition from weak to strong mode coupling. The fiber length L is fixed while the transport mean free path ℓ decreases with increasing mode coupling. In Fig. 2.11, we plot the average bandwidth of PMs and random inputs as a function of the ratio L/ℓ. As L/ℓ increases, the average bandwidth of random input fields increases monotonically, as shown by the black dashed line in Fig. 2.11(a). In a multimode fiber of fixed length L, the path length spectrum is bound by the shortest path that light stays in the lowest-order guided mode while

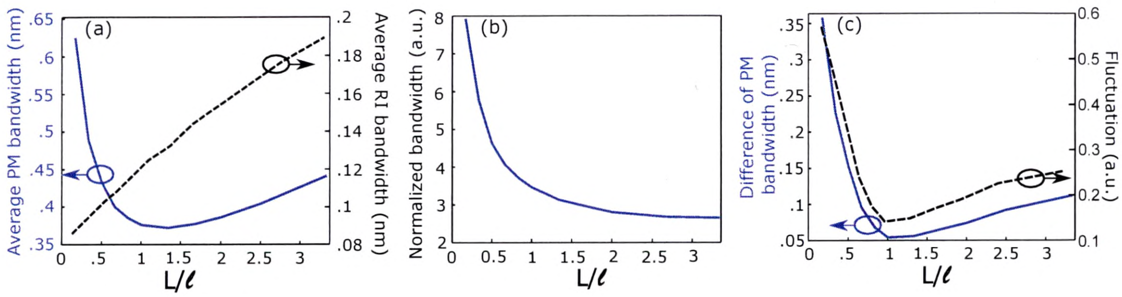

Figure 2.11: Evolution of PM bandwidth with mode coupling strength. (a) With L fixed, the average bandwidth of all PMs (blue solid curve) first decreases with L/ℓ, reaches the minimum at $L/\ell \simeq 1$, and then increases. For comparison (black dashed curve), the average bandwidth of random inputs increases monotonically with L/ℓ. The circles and arrows are denoting the corresponding axes. (b) The normalized bandwidths (bandwidth enhancement ratio) of PMs decrease with L/ℓ and approaches a constant. (c) The difference between the maximum bandwidth and the minimum bandwidth (blue, solid line) exhibits a similar trend as the average bandwidth. The bandwidth difference is normalized by the average bandwidth to show the relative bandwidth fluctuation (black, dashed line). The circles and arrows are denoting the corresponding axes.

propagating through the fiber, and by the longest path that light remains in the highest-order mode. Mode coupling causes light to be randomly scattered from one mode to another, thus the path length spectrum gets narrower. Consequently, the bandwidth of random input increases [26,30,31]. This is different from light diffusion in a random scattering medium. With a fixed system size L, an increase of the scattering strength (corresponding to a decrease of the transport mean free path ℓ) will increase the mean scattering path length and broaden the path length spectrum. The shortest path-length is L while the longer scattering path lengths change with ℓ. In a diffusive medium, the width of the path length spectrum increases linearly with the mean path length $\sim L^2/\ell$, thus the bandwidth will decrease as ℓ gets shorter. For PMs, the average bandwidth first decreases rapidly, then goes through a turning point at $L/\ell \simeq 1$, and starts increasing again [Fig. 2.11(a), blue solid curve]. In the absence of mode coupling, the PMs are simply the linearly polarized (LP) modes, which are the eigenmodes of the fiber with the weak-guiding approximation. Each PM corresponds to a single path length and has an infinite bandwidth. This is different from the case of a random input field that excites all LP modes with distinct propagation constants, leading to a large spread of path lengths and a small bandwidth. With the introduction of mode coupling, an LP mode is scattered to nearby ones with similar propagation constants. Each PM becomes a superposition of a few LP modes with slightly different propagation constants. The increase of the path length spread results in a reduction in the PM bandwidth. In the single scattering regime $L/\ell < 1$, stronger mode coupling further spreads light in mode space, and each PM consists of more LP modes. In particular, the number of LP modes in the PM with short or long delay time grows faster and approaches that with medium delay time. Consequently, the path-length distributions broaden more quickly and the bandwidths decrease more rapidly for the slow and fast PMs, leading to the reduction of the two local maxima at the shortest and longest delay times [Fig. 2.9(a,b)].

Figure 2.11(b) plots the normalized bandwidth, i.e, the ratio of the average bandwidth of PMs over that of random inputs, when the fiber length L is fixed. As the transport mean free path ℓ decreases with increasing mode coupling, the normalized bandwidth drops monotonically and eventually approaches a constant in the strong mode coupling regime. This behavior is in contrast to the non-monotonic variation of the actual bandwidth of PMs in Fig. 2.11(a), and it is attributed to the continuous increase of the random input bandwidth with mode coupling strength.

To find the range of PM bandwdiths, we also calculate the difference between the largest and smallest bandwidths of PMs, which exhibits a trend similar to the average bandwidth as seen in Fig. 2.11(c). In the weak mode coupling regime, the range is large but it declines dramatically with the coupling strength. When the system gradually transits to the strong mode coupling regime, the range increases slightly, but still remains at a small value. We normalized the range of PM bandwidth by the mean, which gives the relative fluctuation of the bandwidth (black dashed line), as shown in Fig. 2.11(c).

2.6 Conclusion

In summary, we experimentally probed individual eigenstates of the Wigner-Smith time-delay matrix of a multimode fiber with mode mixing. By applying external stress to the fiber and gradually adjusting the stress, we demonstrated PMs in the weak and strong mode coupling regime. In the weak mode coupling regime, each PM is composed of a small number of fiber eigenmodes with similar propagation constants. In the strong mode coupling regime, however, a PM is formed by all modes. We find that the well-defined delay times of the eigenstates are formed by multi-path interference, which can be manipulated by the spatial degrees of freedom of the input wavefront. Within certain bandwidths, PMs possess the unique spectral and temporal property that the spatial and temporal variations of the transmitted field are decoupled. It enables a global spatiotemporal control of pulse transmission through complex media. Such global control is more challenging than the control over a single spatial channel.

The bandwidths of PMs are very different in the weak and strong mode coupling regime. When there is no mode-dependent loss in the fiber, PMs with shorter or longer delay times have broader bandwidths in the weak mode coupling regime. The opposite is true for strong mode coupling where the bandwidth is maximal for PMs with medium delay times. By analyzing the path-length distributions, we discover two distinct mechanisms that determine the bandwidth of PMs in the weak and strong mode coupling regime. For weak mode coupling, fast or slow PMs spread less in mode space and experience weaker modal dispersion, thus having broader bandwidth than intermediate PMs. In the strong mode coupling regime, the path-length spectrum gets narrowed, and the maximum bandwidth is reached for the PMs whose delay time corresponds to the maximum density of path-length. Without MDL, the density of path-length is peaked at intermediate lengths such that the PMs with medium delay times have the largest bandwidth. MDL also affects the bandwidths of PMs. In the presence of MDL, the bandwidth for a slow PM is reduced significantly while that for a fast PM remains nearly unchanged. With MDL, the maximum density of path-length shifts to shorter paths, due to stronger attenuation of longer paths in the fiber. Consequently, MDL enhances the bandwidth of fast PMs while it reduces the bandwidth of slow PMs.

We also realized the transition from weak to strong mode coupling. Such a transition is mapped to that from single scattering to multiple scattering in mode space. During the transition from the weak to the strong mode coupling regime, the mean bandwidth of all PMs displays a non-monotonic evolution, reaching a global minimum at the transition point right between these two regimes. In contrast, the normalized bandwidth, which represents the enhancement of the PM bandwidth over that of random input fields, decreases monotonically with increasing mode coupling. The evolution of PM bandwidth with the disorder strength in a multimode fiber is thus very different from that in a random scattering medium, highlighting the subtle differences of light transport in multimode fibers and turbid media.

Bibliography

[1] W. Xiong, P. Ambichl, Y. Bromberg, B. Redding, S. Rotter and H. Cao, Spatiotemporal control of light transmission through a multimode fiber with strong mode coupling, Phys. Rev. Lett. **117**, 053901 (2016).

[2] W. Xiong, P. Ambichl, Y. Bromberg, B. Redding, S. Rotter and H. Cao, Principal modes in multimode fibers: exploring the crossover from weak to strong mode coupling, Opt. Express **25**, 2709-2724 (2017).

[3] E. Doron, U. Smilansky and A. Frenkel, Experimental demonstration of chaotic scattering of microwaves, Phys. Rev. Lett. **65**, 3072 (1990).

[4] D. V. Savin, & H. J. Sommers, Delay times and reflection in chaotic cavities with absorption, Phys. Rev. E **68**, 036211 (2003).

[5] Y. V. Fyodorov, D. V. Savin and H. J. Sommers, Scattering, reflection and impedance of waves in chaotic and disordered systems with absorption, J. Phys. A **38**, 10731 (2005).

[6] S. Rotter, P. Ambichl and F. Libisch, Generating particlelike scattering states in wave transport, Phys. Rev. Lett. **106**, 120602 (2011).

[7] P. W. Brouwer, K. M. Frahm and C. W. J. Beenakker, Quantum mechanical time-delay matrix in chaotic scattering, Phys. Rev. Lett. **78**, 4737 (1997).

[8] P. W. Brouwer, K. M. Frahm and C. W. J. Beenakker, Distribution of the quantum mechanical time-delay matrix for a chaotic cavity, Waves Random Media **9**, 91 (1999).

[9] A. Lagendijk, and B. A. Van Tiggelen, Resonant multiple scattering of light, Phys. Rep. **270**, 143 (1996).

[10] A. Z. Genack, P. Sebbah, M. Stoytchev, and B. A. Van Tiggelen, Statistics of wave dynamics in random media, Phys. Rev. Lett. **82**, 715 (1999).

[11] B. A. Van Tiggelen, P. Sebbah, M. Stoytchev, and A. Z. Genack, Delay-time statistics for diffuse waves, Phys. Rev. E **59**, 7166 (1999).

[12] M. Davy, Z. Shi, J. Wang, X. Cheng, A. Z. Genack, Transmission eigenchannels and the densities of states of random media, Phys. Rev. Lett. **114**, 033901 (2015).

[13] Z. Shi and A. Z. Genack, Dynamic spectral properties of transmission eigenchannels in random media, Phys. Rev. B **92**, 184202 (2015).

[14] M. Mounaix, D. Andreoli, H. Defienne, G. Volpe, O. Katz, S. Grésillon and S. Gigan, Spatiotemporal coherent control of light through a multiple scattering medium with the multi-spectral transmission matrix, Phys. Rev. Lett. **116**, 253901 (2016).

[15] L. Eisenbud, Ph.D. thesis, Princeton, 1948.

[16] E. P. Wigner, Lower limit for the energy derivative of the scattering phase shift, Phys. Rev. **98**, 145 (1955).

[17] F. T. Smith, Lifetime matrix in collision theory, Phys. Rev. **118**, 349 (1960).

[18] D. J. Richardson, J. M. Fini and L. E. Nelson, Space-division multiplexing in optical fibres, Nat. Photon. **7**, 354 (2013).

[19] C. D. Poole and R. E. Wagner, Phenomenological approach to polarisation dispersion in long single-mode fibres, Electron. Lett. **22**, 1029 (1986).

[20] S. Fan and J. M. Kahn, Principal modes in multimode waveguides, Opt. Lett. **30**, 135 (2005).

[21] J. Carpenter, B. J. Eggleton and J. Schröder, Observation of Eisenbud-Wigner-Smith states as principal modes in multimode fibre, Nat. Photon. **9**, 751 (2015).

[22] S. Fan, & J. M. Kahn, Principal modes in multimode waveguides. Opt. Lett. **30**, 135-137 (2005).

[23] V. Arrizón, U. Ruiz, R. Carrada and L. A. González, Pixelated phase computer holograms for the accurate encoding of scalar complex fields, J. Opt. Soc. Am. A **24**, 3500 (2007).

[24] K. P. Ho and J. M. Kahn, Statistics of group delays in multimode fiber with strong mode coupling, J. Lightwave Technol. **29**, 3119-3128 (2011).

[25] K. P. Ho and J. M. Kahn, Linear propagation effects in mode-division multiplexing systems, J. Lightwave Technol. **32**, 614 (2014).

[26] A. F. Garito, J. Wang and R. Gao, Effects of random perturbations in plastic optical fibers, Science **281**, 962-967 (1998).

[27] R. A. Jalabert, H. U. Baranger, and A. D. Stone, Conductance fluctuations in the ballistic regime: A probe of quantum chaos? Phys. Rev. Lett. **65**, 2442 (1990).

[28] M. Brack and R. K. Bhaduri, *Semiclassical Physics* (Addison-Wesley, 1997).

[29] S. Rotter, J.-Z. Tang, L. Wirtz, J. Trost, and J. Burgdörfer, Modular recursive Green's function method for ballistic quantum transport, Phys. Rev. B. **62**, 1950 (2000).

[30] N. K. Fontaine, R. Ryf, M. Hirano, and T. Sasaki, Experimental investigation of crosstalk accumulation in a ring-core fiber, Proc. IEEE Summer Topicals 2013, Waikoloa, HI, USA, paper TuC4.2.

[31] M. B. Shemirani, W. Mao, R. A. Panicker, and J. M. Kahn, Principal modes in graded-index multimode fiber in presence of spatial- and polarization-mode coupling, J. Lightwave Technol. **27**, 1248-1261 (2009).

Chapter 3

Super- and anti- principal modes

3.1 Introduction

[1] In chapter 2, we studied principal modes (PMs) in multimode fibers. In spite of their promising potential, PMs suffer from two major shortcomings. First, they have a finite spectral width, limiting the bandwidth of input signals that can maintain the temporal pulse shape and spatial coherence after being transmitted. This limitation is severe for MMFs with strong mode mixing as well as for disordered media, where the bandwidth of PMs is particularly narrow. Secondly, PMs are non-orthogonal to each other in non-Hermitian systems like an MMF with mode-dependent loss (MDL), resulting in the crosstalk between them. A fundamental question is thus whether an orthogonal set of states exist that outperform PMs in terms of the spectral correlation width, especially in the restrictive regime of strong mode coupling where a gain in bandwidth is in the highest demand. If such special states indeed exist, a practical question is how to generate them experimentally. Such an operational procedure could have a broad impact on all of the different complex wave scattering systems where

1. This chapter is primarily based on the work published in ref. [1]. P. Ambichl developed the optimization algorithm. W. Xiong performed the experiment and analysis. S. Rotter and H. Cao supervised the project.

PMs can be generated and specifically for photonic applications in communication, imaging, nonlinear microscopy, laser amplifiers, and quantum technology.

In a seemingly unrelated context, it has recently been shown that a disordered medium [2] or an MMF [3–5] can function as a spectrometer with ultrahigh resolution, broad bandwidth and low loss. The output speckle pattern of these systems is formed by multi-path interference and thus changes with the input frequency. The working principle of these spectrometers is to use the frequency-dependent speckle pattern as a fingerprint to recover the input spectrum. To further increase the resolving power of these devices, one needs to enhance the frequency sensitivity of output speckle patterns. The key question here is whether it is possible to achieve this by creating a special input state whose output field pattern is considerably more sensitive to a frequency change than that of a typical input. The crucial point is, in other words, whether one can use the spatial degree of freedom at the input to accelerate the spectral decorrelation at the output of a disordered medium or of an MMF.

Another practical application of MMFs in biomedical imaging is to reduce the spatial coherence of a broadband light source for parallel optical coherence tomography (OCT) [6]. When imaging through turbid media such as biological tissue, the suppression of spatial coherence of the illuminating light prevents resolution loss from crosstalk due to coherent multiple scattering. If it was possible to create a state in the MMF with much reduced spectral correlation, one could greatly suppress the spatial coherence at the MMF output by launching broadband light into such a state.

Here we introduce such novel states of light that have the aforementioned unique characteristics. As we demonstrate explicitly, exceeding the already efficient performance of PMs is possible by making use of the information stored in the multi-spectral transmission matrix of an MMF. Based on an optimization procedure operating on such a matrix [7], we are able to create a set of "super-PMs" that not only have a significantly increased spectral stability as compared to the most stable PM available in the same fiber, but that also have the great advantage of being mutually orthogonal even in the presence of MDL. Moreover, our optimization procedure can be applied to generate "anti-PMs" featuring an extremely narrow spectral correlation width – a property that holds promise for spectroscopy and sensing applications with MMFs.

Intuitively, the physical mechanisms for the formation of both "super-PMs" and "anti-PMs" can be understood in the basis of PMs. In the absence of MDL, "super-PMs" are formed by PMs with similar delay times and the interference effect between them brings about a broader bandwidth for the "super-PMs". On the contrary, "anti-PMs" are composed of PMs with extremely different delay times, which directly results in a bandwidth even narrower than that of random inputs. More importantly, our analysis illustrates that the PMs provide a powerful basis for synthesizing new types of states with unique spatial, temporal and spectral characteristics.

3.2 Super-principal modes

3.2.1 Increase the correlation bandwidth

The first question we address here is whether it is possible to increase the correlation width beyond the values obtained for PMs. To achieve this goal, we revisit the design principle of PMs, which are generated by the operator

$$q\,\hat{\phi} = -i\,t^{-1}(\omega_0)\,\frac{dt}{d\omega}|_{\omega=\omega_0}\,\hat{\phi} = \tau\,\hat{\phi}, \tag{3.1}$$

such that their output field patterns do not change when changing the input frequency incrementally by $d\omega$ from the reference value ω_0. In a first step we modify this approach to produce a state whose output pattern stays invariant when the input frequency is changed by a finite shift $\Delta\omega$ rather than by the infinitesimal value $d\omega$.

To implement such a strategy, we introduce a new operator that aligns the output vectors of its eigenstate at two arbitrarily spaced frequencies ω_0 (1550 nm, 193.4 THz) and ω (with $\omega - \omega_0 = \Delta\omega$). This new operator $\rho(\omega, \omega_0)$ takes the following form,

$$\rho(\omega, \omega_0) := -i\, t^{-1}(\omega_0)\, \frac{t(\omega) - t(\omega_0)}{\omega - \omega_0}\,. \tag{3.2}$$

It approaches the time-delay operator q for small frequency spacing between ω_0 and ω, i.e., $q = \lim_{\Delta\omega \to 0} \rho(\omega, \omega_0)$. An eigenstate of this new operator $\rho(\omega, \omega_0)$ features an output correlation function $C(\omega, \omega_0)$, which peaks not only at ω_0 but also at ω. With a gradual increase of $|\Delta\omega|$, the two correlation peaks move further apart, suggesting the possibility of extending the correlation bandwidth beyond that of the PM. We thereby use the term "super-PM" to label a state that has a correlation bandwidth of the output field pattern exceeding that of the widest PM in a given fiber.

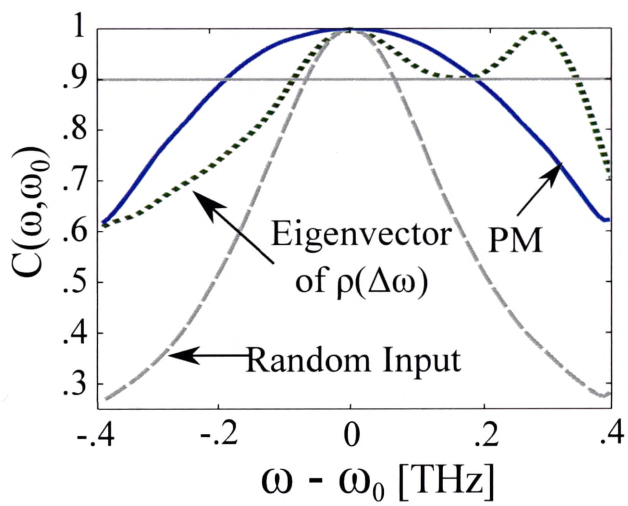

Figure 3.1: Experimentally measured autocorrelation function $C(\omega, \omega_0)$ for the most stable PM (blue solid line). For comparison, we also show the measured average correlation of 20 random inputs (gray dashed line) with a narrower bandwidth. A super-PM eigenvector of $\rho(\Delta\omega)$ with $\Delta\omega = 0.28$ THz is evaluated using the measured transmission matrix and its correlation function (green dotted curve). The horizontal solid gray line indicates the threshold value $C(\omega, \omega_0) = 0.90$ that sets the correlation width.

From the experimentally measured transmission matrix $t(\omega)$, we numerically generate the super-PMs as the eigenstates of $\rho(\omega, \omega_0)$ in Eq. (3.2), and find the anticipated two peaks at ω and ω_0 in the correlation function, as shown by the green dotted curve in Fig. 3.1. The width of each peak is given approximately by the spectral correlation width $\delta\omega$ of the transmission matrix (i.e., the correlation width associated with random input). As the frequency spacing between the two peaks at ω and ω_0 exceeds the peak width $\delta\omega$, a dip develops in between the two peaks. To maximize the correlation bandwidth, we choose the spacing $\omega - \omega_0$ such that $C(\omega, \omega_0)$ drops to the threshold value of 0.9 in between the two peaks in Fig. 3.1(b). In this case, the correlation width is about 18% wider than the width of the widest PM. A further increase of $\Delta\omega$ makes the dip in between the two peaks drop to below 0.9, causing a sudden decrease in bandwidth.

To reach the ideal case of a flat correlation function $C(\omega, \omega_0) \approx 1$ over the entire interval $[\omega_0, \omega]$, $\Delta\omega$ must be less than $\delta\omega$. The fundamental reason that prevents such a flat correlation curve from being realized in a broader frequency interval can be understood from the construction principle of $\rho(\omega, \omega_0)$ and of its eigenstates: a state with a flat correlation function $C(\omega, \omega_0) \equiv 1$ in a finite interval $[\omega_0, \omega]$ would have to be a simultaneous eigenstate of *all* operators $\rho(\omega, \omega_0)$ in this ω-interval. The relevant commutator that would have to vanish for this to be possible is, however, non-zero in general: $[\rho(\omega_1, \omega_0), \rho(\omega_2, \omega_0)] \neq 0$ with $|\omega_1 - \omega_2| > \delta\omega$.

3.2.2 Nonlinear optimization

In spite of this restriction, we will now show how to create a set of states with correlation bandwidth considerably exceeding that of conventional PMs. In addition, we will make such "super-PMs" mutually orthogonal, even when the fiber has MDL. Both the PMs and super-PMs described above are non-orthgonal, as the operators $q(\omega_0)$ and $\rho(\omega, \omega_0)$ become non-Hermitian in the presence of MDL. We will thus work with a new approach that constructs the desired set of super-PMs as approximate rather than as perfect simultaneous eigenvectors of the operators $\rho(\omega, \omega_0)$ within a

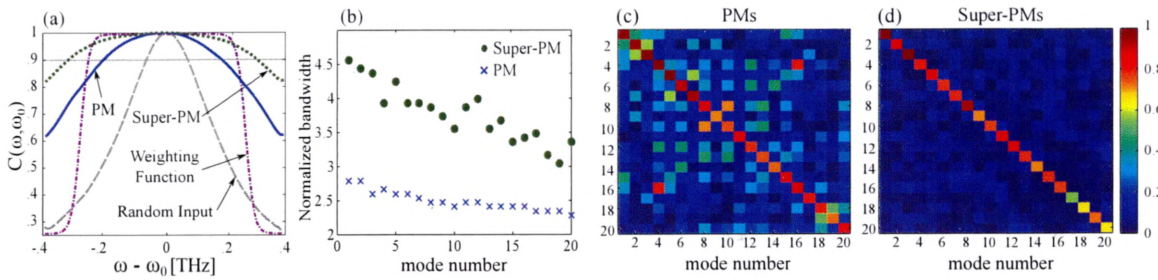

Figure 3.2: Bandwidth comparison of PMs and super-PMs. (a) Measured spectral correlation function $C(\omega, \omega_0)$ for the output signals of the widest PM (blue solid line), and for the widest super-PM obtained from our bandwidth optimization (green dotted line). The weighting function $W(\omega)$ used in the cost function of Eq. (3.3) is shown as purple dash-dotted line. The gray dashed line shows the spectral correlation of a random input. The horizontal solid gray line indicates the threshold value $C(\omega, \omega_0) = 0.90$ that sets the correlation width. (b) Spectral correlation width of super-PMs and PMs normalized by that of a random input. Our optimization scheme found 20 super-PMs that have a larger bandwidth than the widest PM. The orthogonality of the output field patterns for the 20 widest PMs (c) and the 20 super-PMs (d). In the presence of loss, the PMs are not orthogonal but the super-PMs are.

desired spectral interval. Achieving this objective calls for the implementation of an optimization procedure with a non-linear cost function involving the multi-spectral transmission matrix $t(\omega)$ and the operators $\rho(\omega, \omega_0)$. Given the dimensionality of the problem determined by the number of fiber modes and the width of the spectral region of interest, such an optimization is a very demanding task even numerically.

In the following we take a shortcut to create orthogonal super-PMs by working with a considerably reduced optimization functional $\mathcal{T}$ (cost function),

$$\begin{aligned}\mathcal{T}\left(\hat{\phi}\right) &:= \int d\omega \, \left[1 - C(\omega, \omega_0)^2\right] W(\omega) \\ &= \int d\omega \left[1 - \frac{\left|\vec{\psi}^{\dagger}(\omega) \cdot \vec{\psi}(\omega_0)\right|^2}{\left|\vec{\psi}(\omega)\right|^2 \left|\vec{\psi}(\omega_0)\right|^2}\right] W(\omega) \,. \end{aligned} \tag{3.3}$$

The spectral range that is effectively taken into account in this functional is defined by the weighting function $W(\omega)$, which is chosen to be a step-like, but continuous function centered around ω_0, see Fig. 3.2(a) (purple dash-dotted curve). To maximize the width of the correlation function $C(\omega, \omega_0)$, the (scalar) value of $\mathcal{T}$ needs to be minimized depending on the input state $\hat{\phi} = t^{-1}(\omega)\, \vec{\psi}(\omega)$. We implement an efficient minimization of $\mathcal{T}$ using a simple gradient-based scheme.

The gradient with respect to $\hat{\phi}^\dagger$ using $\vec{\psi}(\omega) = t(\omega)\, \hat{\phi}$ for the cost function

$$
\begin{aligned}
\mathcal{T}\left(\hat{\phi}\right) &= \int d\omega \left(1 - \frac{\left|\vec{\psi}^\dagger(\omega) \cdot \vec{\psi}(\omega_0)\right|^2}{\left|\vec{\psi}(\omega)\right|^2 \left|\vec{\psi}(\omega_0)\right|^2}\right) W(\omega) \\
&= \int d\omega \left(1 - \frac{\left|\hat{\phi}^\dagger t^\dagger(\omega)\, t(\omega_0)\, \hat{\phi}\right|^2}{\left|t(\omega)\, \hat{\phi}\right|^2 \left|t(\omega_0)\, \hat{\phi}\right|^2}\right) W(\omega),
\end{aligned}
\tag{3.4}
$$

reads

$$
\begin{aligned}
\frac{\delta \mathcal{T}}{\delta \hat{\phi}^\dagger} &= \int d\omega \Bigg[\left(t^\dagger(\omega)\, t(\omega_0) + t^\dagger(\omega_0)\, t(\omega)\right) \\
&\quad + \hat{\phi} \frac{-\hat{\phi}^\dagger t^\dagger(\omega_0)\, t(\omega)\, \hat{\phi}}{\left|t(\omega)\, \hat{\phi}\right|^2 \left|t(\omega_0)\, \hat{\phi}\right|^2} \\
&\quad + t^\dagger(\omega)\, t(\omega)\, \hat{\phi}\, \frac{\left|\hat{\phi}^\dagger t^\dagger(\omega)\, t(\omega_0)\, \hat{\phi}\right|^2}{\left|t(\omega)\, \hat{\phi}\right|^4 \left|t(\omega_0)\, \hat{\phi}\right|^2} \\
&\quad + t^\dagger(\omega_0)\, t(\omega_0)\, \hat{\phi}\, \frac{\left|\hat{\phi}^\dagger t^\dagger(\omega)\, t(\omega_0)\, \hat{\phi}\right|^2}{\left|t(\omega)\, \hat{\phi}\right|^2 \left|t(\omega_0)\, \hat{\phi}\right|^4} \Bigg] W(\omega).
\end{aligned}
\tag{3.5}
$$

Please note that $|t(\omega)\, \hat{\phi}|^2 = \hat{\phi}^\dagger t^\dagger(\omega)\, t(\omega)\, \hat{\phi}$ and that a derivative with respect to $\hat{\phi}$ does not lead to equations linearly independent from the set of equations (3.6), since $\mathcal{T}(\hat{\phi})$ is a real quantity.

The $n+1$-th optimization step for the vector $\hat{\phi}$ that is optimized for is then calculated from the n-th step according to

$$\hat{\phi}_{n+1} = \frac{1}{N_{n+1}} \left(\hat{\phi}_n - \frac{\delta \mathcal{T}}{\delta \hat{\phi}^\dagger} |_{\hat{\phi}_n} \Delta s \right), \tag{3.6}$$

with a suitably chosen stepsize Δs and the normalization constant N_{n+1} assuring $|\hat{\phi}_{n+1}| = 1$. The starting guess for each super-PM optimization is the respective projection of the widest PM onto the subspaces orthogonal to each of the previously calculated super-PMs. In the first iteration step, we start directly from the widest PM.

We note that our optimization scheme is a purely numerical optimization based on the experimentally measured transmission matrices rather than an experimental feedback loop. We typically obtain the widest super-PM with an optimization loop that is initiated with the widest PM as a starting point for the corresponding iteration. Next, a whole cascade of optimizations of Eq. (3.3) is carried out, where in each optimization loop for a single super-PM the cost function $\mathcal{T}$ is minimized in the vector space orthogonal to each of the super-PMs obtained in the preceding steps. In this way, a strictly orthogonal set of super-PMs is obtained.

The input states for these super-PMs are created by the SLM and injected into the fiber. Figure 3.2(a) shows the widest super-PM (green dotted line). Its spectral correlation width is about 70% larger than that of the widest PM. Out of the total 90 modes in the fiber after the matrix truncation, we find 20 super-PMs that outperform the widest PM in terms of the correlation width. Figure 3.2(b) shows the spectral width of super-PMs normalized by that of random input wavefronts. The widest super-PM has a bandwidth increase of 4.5 times as compared to the random input. In addition, we also plot the 20 PMs with the largest bandwidth and find that the bandwidth enhancement for super-PMs is well above that of the PMs.

Because of fiber absorption and scattering loss, the PMs are non-orthogonal already at the fiber input, since they are the eigenstates of the non-Hermitian operator q. The propagation through the fiber will further increase this non-orthogonality, thus PMs are non-orthogonal both at the fiber input and output ends. By contrast, the super-PMs, in the way we construct them, are orthogonal at the input. We also observe that the orthogonality of the super-PMs at the input facet is well sustained during propagation through the fiber. The overlap of the output field patterns is defined as $O_{mn} := |\hat{\psi}_m^\dagger(\omega_0) \cdot \hat{\psi}_n(\omega_0)|$ for the m-th and n-th super-PM. For a perfectly orthonormal set of vectors we would have $O_{mn} = \delta_{mn}$, where δ_{mn} is the Kronecker delta. The 20 widest PMs we consider are rather far away from this ideal case, as shown in Fig. 3.2(c). The average off-diagonal element of O is 0.188. The super-PMs preserve their initial orthogonality to a large extent as shown in Fig. 3.2(d). On average we find for the off-diagonal elements of O a reduced value of 0.068. Thus the crosstalk between different super-PMs is strongly suppressed as compared to the PMs.

To validate our initial hypothesis that the enhanced bandwidth of super-PMs is linked to the property that they mimic mutual eigenstates of all $\rho(\omega, \omega_0)$ operators in the spectral region of interest, we work out a corresponding measure that quantifies how close an input state is to a simultaneous eigenvector of these operators. As briefly discussed there, an eigenstate of all ρ-operators in the spectral region of interest would feature a perfectly flat correlation function. As we will see in the following, the super-PMs, indeed, are closer to being such mutual eigenstates than random inputs or even the PMs. For our purposes, we define the expectation value of $\rho(\omega, \omega_0)$ for a state $\hat{\phi}$ analogously to that of a Hermitian operator like $\langle \rho(\omega, \omega_0) \rangle = \hat{\phi}^\dagger \rho(\omega, \omega_0)\, \hat{\phi}$. In contrast to a Hermitian operator, this expectation value is a complex number in general. The variance for the non-Hermitian operator $\rho(\omega,\omega_0)$, however, can be computed,

$$\begin{aligned}\langle|\rho(\omega,\omega_0)-\langle\rho(\omega,\omega_0)\rangle|^2\rangle &= \hat{\phi}^\dagger\rho(\omega,\omega_0)^\dagger\,\rho(\omega,\omega_0)\,\hat{\phi} \\ &- |\hat{\phi}^\dagger\rho(\omega,\omega_0)\,\hat{\phi}|^2,\end{aligned} \tag{3.7}$$

and gives a purely real number. Note that for an eigenstate of $\rho(\omega,\omega_0)$, the expectation value is equal to the corresponding (complex) eigenvalue, and the variance vanishes. We define a measure that quantifies how close an input state is to being a simultaneous eigenvector of all $\rho(\omega,\omega_0)$ operators,

$$B\left(\hat{\phi}\right) := \frac{1}{\bar{N}_r}\int d\omega\,\frac{\left\langle|\rho(\omega,\omega_0)-\langle\rho(\omega,\omega_0)\rangle|^2\right\rangle}{|\langle\rho(\omega,\omega_0)\rangle|^2}W(\omega)\,. \tag{3.8}$$

The constant $\bar{N}_r$ normalizes B such that the average over a large number (10^5) of random inputs $\bar{B}_r = 1.0$. If $\hat{\phi}$ is a perfect common eigenstate to all $\rho(\omega,\omega_0)$ within the spectral range for optimization, all variances and, therefore, B vanishes. The average for the 20 widest PMs evaluates to $\bar{B}_{\mathrm{PM}} = 3.1\times10^{-4}$ which is almost 4 orders of magnitude smaller than $\bar{B}_r$. The corresponding average for the 20 measured super-PMs, however, is $\bar{B}_{\mathrm{SPM}} = 1.3\times10^{-4}$ which is 2.4 times smaller than for the PMs. We therefore draw the conclusion that although the PMs are already close to being a mutual eigenstate of all relevant $\rho(\omega,\omega_0)$, the super-PMs fulfill this property even better and thereby manage to have an even broader bandwidths.

3.2.3 Decomposition into principal mode basis

Can we also understand on a more intuitive level why and how super-PMs manage to outperform PMs? To answer this question we first decompose both the PMs as well as the super-PMs realized in the experiment in the basis of LP modes of the fiber. In the regime of strong mode coupling where all of the results shown above were obtained, we find that both PMs and super-PMs consist of nearly all LP modes, and the higher-order LP modes have smaller contributions due to higher loss. While this finding confirms that PMs as well as super-PMs are really non-trivial combinations of fiber modes in the strong-coupling regime, it does not shed any light on the difference between PMs and super-PMs. We therefore change the basis from the LP-modes to the PMs themselves, which constitute the natural basis to capture the dynamical aspects of light scattering as each PM is associated with a proper delay time. Also their greatly reduced wavelength dependence makes PMs very suitable to describe the transmitted light in a broad frequency window. When decomposing the super-PMs into the basis of PMs (with the bi-orthogonal basis vectors being sorted according to the delay times of the PMs), we observe clearly that the super-PMs are composed of PMs with neighboring delay times, as shown in Fig. 3.3(a).

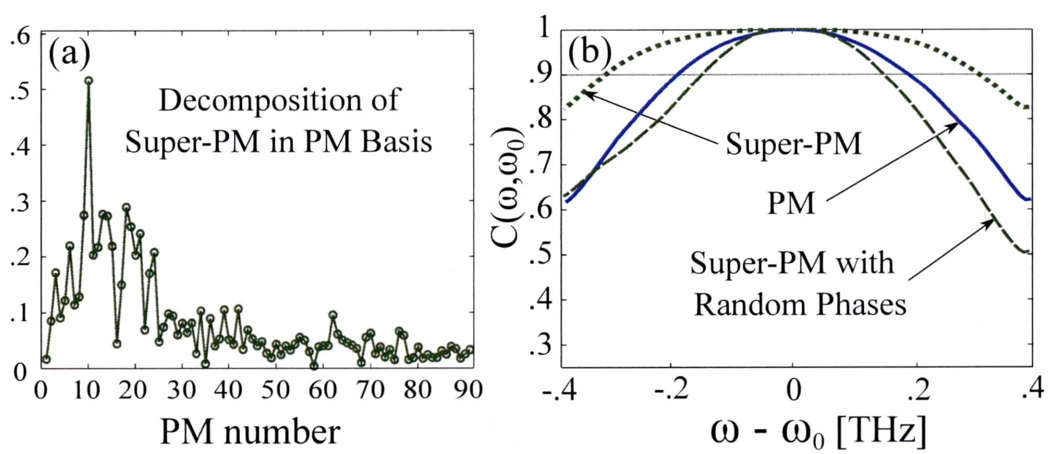

Figure 3.3: (a) Decomposition of the widest super-PM in the basis of PMs, which are numbered from short to long delay time. The super-PM bundles together PMs with similar delay times. (b) Spectral correlation functions of the widest super-PM (green dotted line), the widest PM (blue solid line) and the widest super-PM with phases of constituent PMs randomized (green dashed line). The bandwidth enhancement of super-PMs is sensitive to the phases of constituent PMs, indicating that super-PMs are formed by interference of PMs.

The physical interpretation of this result is that super-PMs build on a very narrow distribution of delay times and enhance the spectral correlation width via in-

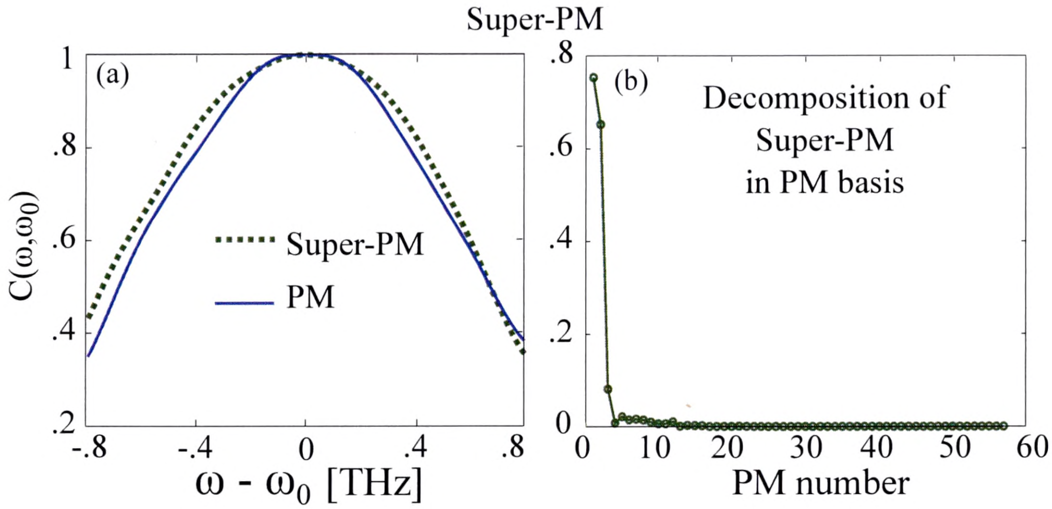

Figure 3.4: Decomposition of super-PMs in the weak mode coupling regime into the basis of PMs. (a) Spectral correlation function of the widest super-PM and the widest PM. They have similar spectral correlations. (b) Decomposition of the widest super-PM in the basis of PMs, which are numbered from short to long delay time. The super-PM is mainly composed of two PMs with the shortest delay times and the widest spectral correlations.

terference of several time-delay eigenstates. To demonstrate that the relative phases of constituent PMs are essential, we also plot in Fig. 3.3(b) the correlation functions after adding random phases to the decomposition coefficients of the PMs (while maintaining the absolute magnitudes). It is evident that randomizing the phase significantly decreases the correlation width. The sensitivity to the relative phase of constituent PMs indicates that the interference of the PMs involved in the formation of a super-PM is essential.

Another relevant aspect is that the mixing of neighboring PMs to create super-PMs requires that a sufficient number of PMs are available with similar delay times. In an MMF with weak mode coupling, the values of the delay times are spread over a much broader time range, and hence the super-PM is composed of only one or two PMs with neighboring delay times. Therefore, the bandwidth of a super-PM is typically not significantly different from its constituent PMs for weak mode coupling. To test this conjecture, we apply the same optimization algorithm as above to fibers in the weak mode coupling regime. As shown in Fig. 3.4, the results indicate that in this case the super-PMs are very similar to individual PMs and no significant admixture from several PMs is seen. Consequently, the correlation width of even the widest super-PM barely exceeds that of the widest PM. Super-PMs thus realize their full potential in the regime of strong-mode coupling where a gain in bandwidth is also most relevant since the PM-bandwidths in the strong-coupling limit are much narrower than for weak mode-coupling [8].

3.3 Anti-principal modes

We will now investigate whether special states of light may also be found when turning the concept of principal modes on its head. Specifically, we will address the question, whether it is possible to create not only states with a very broad spectral correlation width such as the PMs or the super-PMs studied above, but also states with a drastically reduced bandwidth as compared to the values associated with a typical or random input wavefront. Such "anti-PMs" would have an enhanced frequency sensitivity as desired, e.g., for fiber-based spectrometers whose operation principle relies on a very narrow correlation bandwidth [3]. The optimization algorithm presented above now allows us to generate such highly sensitive states by just maximizing instead of minimizing the functional $\mathcal{T}$ in Eq. (3.3).

We first apply the algorithm for anti-PMs on an ideal MMF with no MDL. The corresponding unitary transmission matrix is obtained numerically with the concatenated fiber model. For simplicity, we consider a planar waveguide with a core width of 200 μm and a numerical aperture of 0.22, supporting 57 guided modes [9]. The total length of the waveguide is one meter, divided into 20 segments in each of which light propagates without mode coupling. Between adjacent segments, all modes are randomly coupled, as simulated by a unitary random matrix introduced in chapter 1.

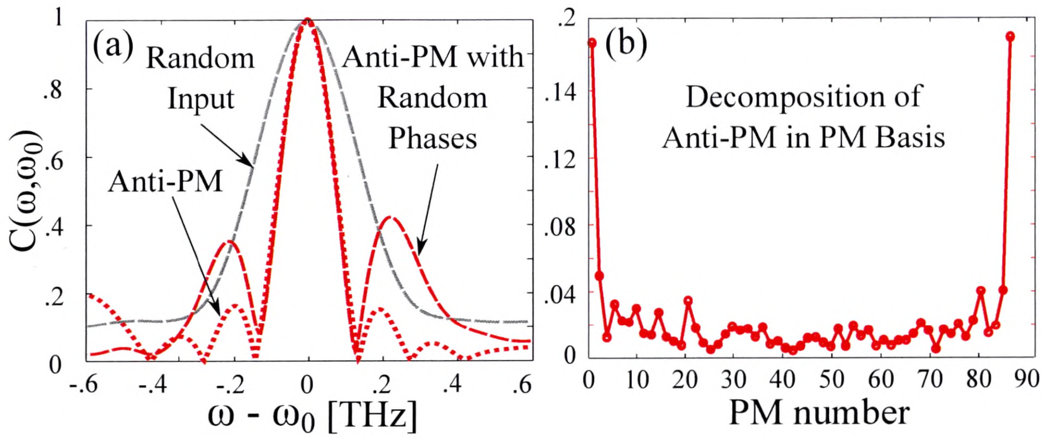

Figure 3.5: Numerically determined anti-PM in a fiber without MDL. (a) Spectral correlation function of the narrowest anti-PM (red dotted line), which is significantly narrower than that of the random input (gray dashed line). The red dashed line is obtained by randomizing the phases of constituent PMs in the anti-PM. The phase randomization does not change the main peak, but enhances the two side peaks. (b) The decomposition of this anti-PM in the PM basis shows two pronounced maxima at the extreme values of the involved PMs, indicating that anti-PMs are efficiently formed by combining the fastest and the slowest PMs. The data shown here result from the numerical simulation of a waveguide with 200 μm width, 0.22 numerical aperture, 1-meter length and no loss.

The results obtained by applying the optimization algorithm to this numerical model are shown in Fig. 3.5(a), displaying a significant reduction of the spectral correlation width of the anti-PM as compared to random inputs. Moreover, when decomposing the anti-PM in the basis of PMs, we immediately see that the narrowest anti-PM consists mainly of admixtures between the fastest and slowest PMs [see Fig. 3.5(b)]. These PMs have the largest achievable temporal difference in the MMF and mixing them with similar weight thus leads to an efficient decorrelation when changing the input frequency. Quite intuitively, the anti-PMs thus not only form the antipodes of the super-PMs in terms of their correlation bandwidth, but also in terms of the way they are constructed: while super-PMs group together several PMs with similar time delay, the anti-PMs combine those PMs with the most different time delay available. Whereas the relative phase with which this superposition of PMs is implemented clearly matters for super-PMs [see Fig. 3.3(b)], we find that for anti-PMs the correlation bandwidth is barely affected when changing the phases of constituent PMs [see the red dashed curve in Fig. 3.5(a)].

The reason behind this observation is that for PMs associated with very different delay times adjusting their relative phase cannot mend these states' intrinsic tendency to decorrelate with frequency, while for states with nearby delay times the appropriate phases will optimize the interferences for specific mode-coupling in the MMF such as to increase the correlation width. As shown by the red dashed curve in Fig. 3.5(a), the correlation function features two enhanced side peaks adjacent to the main peak for the anti-PM with phases of constituent PMs randomized. After reaching zero, the correlation revives as ω is tuned further from ω_0. This revival is caused by the beating of the slowest and fastest PMs, the two main components of the anti-PM. When the relative phase of the fastest and slowest PMs accumulates 2π, the output field should be the same as the one when the relative phase is zero. However, small contributions from PMs with intermediate delay times give rise to multi-path interference that suppresses the side peaks in the anti-PM in a phase-sensitive way.

To connect with the experimental case of anti-PMs, it is essential to take into account the mode dependent loss (MDL) in the fiber. We gradually increase the MDL in the numerical simulations up to the value close to the MMF used in the experiment. The narrowest anti-PM displays a narrowing of the spectral correlation function, and its bi-modal composition in the PM-basis changes drastically, as shown in Fig. 3.6. In particular, the increase of MDL enhances the weight of the slowest PMs, and the composition of the anti-PM in the PM-basis becomes much broader. This can be explained by considering that the MDL attenuates the slowest PMs most strongly since they stay longest inside the fiber. The broadening of the PM-composition can then be understood as a mechanism to compensate for the reduced contributions from the slow PMs. Since the constituent PMs with similar delay times overlap in

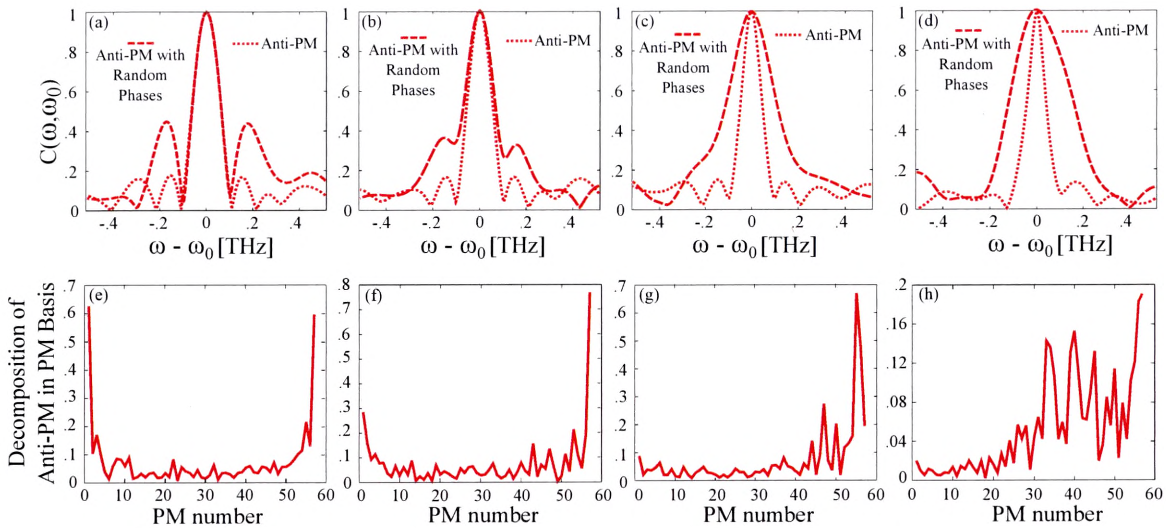

Figure 3.6: Effect of MDL on the bandwidth and decomposition of anti-PMs. (a)-(d) Spectral correlation function of the narrowest anti-PM (red dotted line) in a multimode waveguide with MDL = 0 dB, -3.5 dB, -7.5 dB and -20 dB correspondingly. The red dashed line is obtained by randomizing the phases of constituent PMs in the anti-PM. The phase randomization significantly increases the spectral correlation width at large MDL, where the formation of anti-PM relies more on the interference of constituent PMs. (e-h) Decomposition of the anti-PMs in (a-d) in the basis of PMs, which are numbered from short to long delay times. As the MDL increases, the PM with long delay time gains weight to compensate for the stronger loss.

time, their relative phases become important. When randomizing their phases, the bandwidth of anti-PMs is increased (Fig. 3.6).

When generating the anti-PMs in the MMF we find 62 anti-PMs out of 90 fiber modes, whose spectral correlation width is narrower than that of random inputs. Fig. 3.7 shows the data for the narrowest anti-PM. Due to the MDL, it is broadly spread in the PM basis, but it still decorrelates much more quickly than the random input with frequency detuning. Only when moving from the strong to the weak mode-coupling limit do we find that anti-PMs have about the same correlation width as a random input even without MDL, as shown in Fig. 3.8. This is because in the weak mode coupling regime, the fastest PM and the slowest PM have very different delay times. The beating between the two PMs is so strong that it causes significant side peaks of the spectral correlation function. To reduce the side peaks, additional PMs

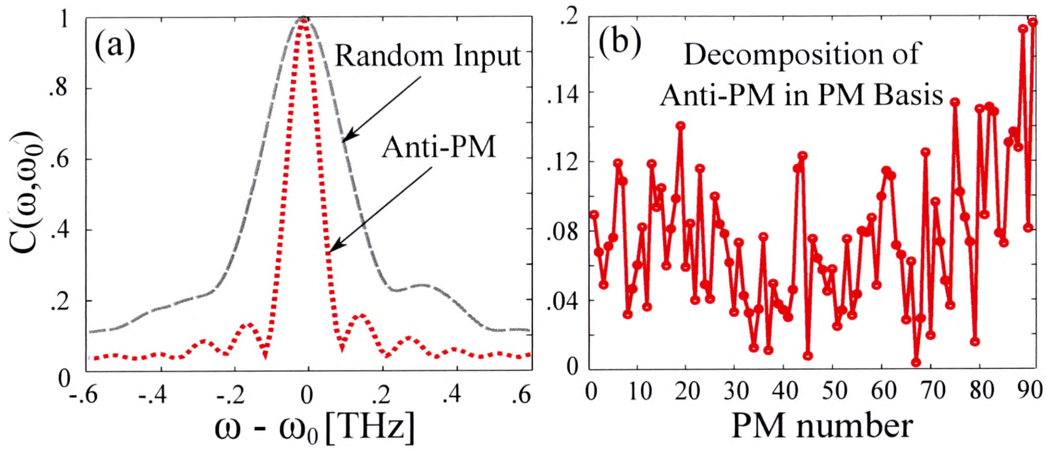

Figure 3.7: Experimentally measured anti-PM in the same fiber as in Fig. 1. (a) The spectral correlation function of the narrowest anti-PM (red dotted line), which is notably narrower than that for a random input (gray dashed line). (b) Due to mode-dependent loss, the decomposition of this anti-PM in the PM basis does not give the bi-modal distribution as in Fig. 3.5(b), but rather a broad distribution over all available PMs. This result agrees with the numerical simulation that includes the MDL (Fig. 3.6)

with intermediate delay times must be included. The inclusion of many intermediate PMs makes the correlation width of the anti-PM similar to that of a random input. Therefore, both super-PMs and anti-PMs have in common that they unfold their full potential in the limit of strong mode coupling.

3.4 Conclusion

In summary, we present a special set of light states in multi-mode fibers that have either a significantly broader spectral correlation than the principal modes or a significantly narrower spectral correlation than a random input wavefront, respectively. We thus term these special states super- and anti-principal modes, and demonstrate how to generate them with a simple gradient-based algorithm based on the experimentally measured multi-spectral transmission matrix. Our optimization algorithm allows us to determine a whole set of such super- or anti-PMs, which are mutually orthogonal

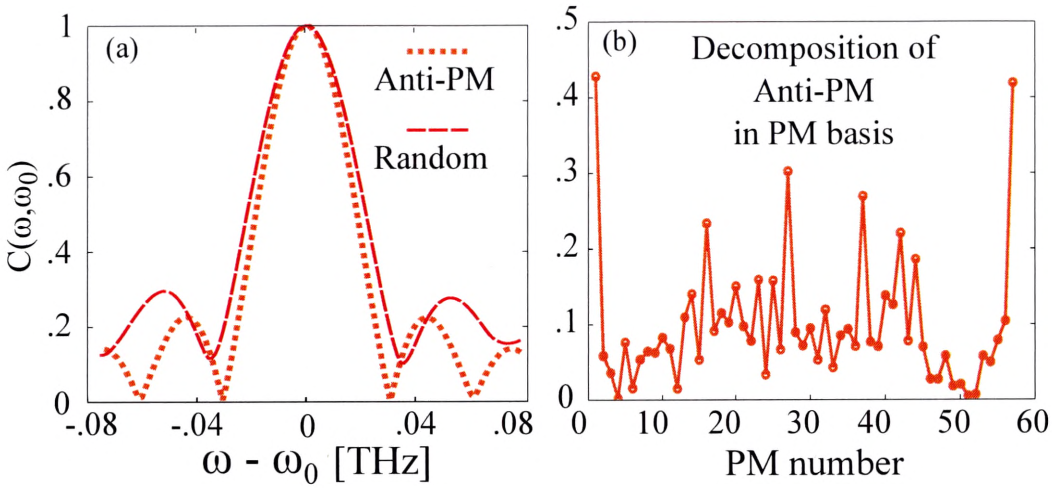

Figure 3.8: Anti-PMs in the weak mode coupling regime. (a) In the weak mode coupling regime, the anti-PM yields a similar spectral correlation as the random input. (b) Decomposition of the anti-PM in the PM basis. PMs with intermediate delay times are involved to reduce the side peaks of spectral correlation function.

to each other even in the presence of mode-dependent loss and thus feature much reduced crosstalk. By overcoming the limitations of PMs, super-PMs outperform the PMs in terms of bandwidth and orthogonality. The performance gain is the highest in the regime of strong mode coupling as for very long fibers, where an increase in bandwidth is also most sought-after. For fibers with high mode numbers we still see considerable room for improving our optimization strategy to identify super- and anti-PMs and expect follow-up studies to propose more efficient and problem-specific optimizers that outperform the all-purpose gradient-descent routine we used here. Another interesting topic for further study is the sensitivity of super- and anti-PMs with respect to fiber bending and whether one can predict in which way they change when parts of the fiber are moved [10].

Our work also provides a physical understanding of how these states are formed by decomposing them in the PM basis. Super-PMs tend to combine several PMs with nearby delay times in a super-position with optimized phases. Anti-PMs, on the contrary, tend to combine PMs with the most different delay times available in the fiber. The presence of MDLs leads to modifications of these states, which are analyzed in detail.

On the one hand, the large bandwidth and mutual orthogonality of super-PMs pave the way for their application to dispersion-free transmission of pulses through complex media. On the other hand, the high spectral sensitivity of anti-PMs makes them ideally suited for optimizing the resolution of speckle spectrometers based on disordered media or on MMFs as well as for reducing the spatial coherence of a broadband light source for crosstalk-free imaging [11]. Since neither the concept of super- or anti-PMs nor the ability to create complex wave fields with wavefront shaping are restricted to a specific type of scattering system or to a specific type of wave, we expect our results to be easily transferable to other experimental platforms. In this context we note that we restricted ourselves here to just one polarization both at the in- and output of the fiber and that we did require any information about the light scattered in the undetected polarization degree of freedom of the MMF. Since neglecting this part is conceptually similar to neglecting the light that is back-reflected from a disordered medium, we do not foresee any major obstacle to transfer the concepts of PMs, super-PMs and anti-PMs to disordered media based on the medium's transmission matrix alone.

Bibliography

[1] P. Ambichl, W. Xiong, Y. Bromberg, B. Redding, H. Cao and S. Rotter, Super- and anti-principal-modes in multimode waveguides, Phys. Rev. X **7**, 041053 (2017).

[2] B. Redding, S. F. Liew, R. Sarma and H. Cao, Compact spectrometer based on a disordered photonic chip, Nat. Photon. **7**, (2013).

[3] B. Redding and H. Cao, Using a multimode fiber as a high-resolution, low-loss spectrometer, Opt. Lett. **37**, 3384-3386 (2012).

[4] N. Coluccelli, M. Cassinerio, B. Redding, H. Cao, P. Laporta and G. Galzerano, The optical frequency comb fibre spectrometer, Nat. Commun. **7**, 12995 (2016).

[5] G. C. Valley, G. A. Sefler and T. J. Shaw, Multimode waveguide speckle patterns for compressive sensing, Opt. Lett. **41**, 2529-2532 (2016).

[6] A. H. Dhalla, J. V. Migacz and J. A. Izatt, Crosstalk rejection in parallel optical coherence tomography using spatially incoherent illumination with partially coherent sources, Opt. Lett. **35**, 2305-2307 (2010).

[7] D. Andreoli, G. Volpe, S. Popoff, O. Katz, S. Grsillon & S. Gigan, Deterministic control of broadband light through a multiply scattering medium via the multispectral transmission matrix, Sci. Rep. **5**, 10347 (2015).

[8] W. Xiong, P. Ambichl, Y. Bromberg, B. Redding, S. Rotter and H. Cao, Principal modes in multimode fibers: exploring the crossover from weak to strong mode coupling. Opt. Express **25**, 2709-2724 (2017).

[9] K. Okamoto, Fundamentals of Optical Waveguides (Elsevier, New York, 2005)

[10] M. Plöschner, T. Tyc and T. Čižmár, Seeing through chaos in multimode fibres, Nat. Photon. **9**, 529 (2015).

[11] H. Cao, Perspective on speckle spectrometers. J. Opt. **19**, 060402 (2017).

Chapter 4

Long-range spatio-temporal correlations in multimode fibers for pulse delivery

4.1 Introduction

[1]In this chapter, we first study long-range correlation in MMFs. The topic is slightly different from the last two chapters, but as we will show, the long-range correlation plays an important role in energy delivery of an optical pulse through an MMF. This pulse delivery process is related to principal modes and super-principal modes in the narrow frequency range, but outperforms the latter two when the frequency range of the input pulse is broad. An analytical relation between pulse delivery and principal modes will be presented at the end of this chapter.

Coherent transport of classical and quantum waves in disordered media exhibits long-range correlations, which exist in space, angle, frequency, time, and polariza-

1. This chapter is primarily based on the work published in ref. [1]. W. Xiong performed the experiment and numerical simulations. C. W. Hsu derived the theory. H. Cao supervised the project.

tion [2–16]. Such correlations, resulting from the crossing of wave paths, are responsible for the formation of highly transmitting channels in diffusive systems [17–20]. In the frequency domain, long-range correlations enable broadband enhancement of transmission through disordered media by wavefront shaping [21]. Spatially, long-range correlations significantly increase the efficiency of wave focusing to a target of size much larger than the wavelength in strongly scattering media [22]. However, long-range correlations also increase the background when optimizing the energy delivered to a single speckle grain for continuous waves [23, 24] and pulses [25].

From the aspect of scattering, a multimode fiber (MMF) with strong mode mixing shares similarities with a disordered medium. Inherent imperfections and environmental perturbations introduce random mode coupling in an MMF, and its effect grows with the length of the fiber [26, 27]. Such coupling can be regarded as scattering in the fiber mode space, leading to energy transfer from the input mode to the other transverse modes. An MMF has a significant difference from the disordered medium: negligible reflection and low propagation loss leading to near-unity transmission. For a continuous wave input, energy conservation dictates that the intensity increase in one mode must be accompanied by intensity decreases in other modes, resulting in negative correlation among the transmitted spatial modes, similar to those found in weak-scattering (ballistic) systems and chaotic cavities [9, 28, 29]. If the MMF has a large number of modes, such static correlations are very weak. When the input is a short pulse, however, energy is no longer conserved at any particular time, and correlation may be modified and become time-dependent. Nevertheless, little is known about such dynamic correlation in MMFs.

In this chapter, we discover long-range spatio-temporal correlations in MMFs with strong random mode mixing. For a short pulse input, the transmitted intensities in different spatial channels are generally positively correlated at a given arrival time. The correlation is enhanced at arrival times away from the center of the transmitted pulse, which we attribute to the reduced number of propagation paths at early or late arrival times. The transmitted powers at different delay times are positively correlated for short separation of the delays, and become negatively correlated for distant delays. Such dynamic correlations in an MMF are distinct from those in diffusive or localized random media where the long-range correlations in transmission are always positive [10, 25].

The spatio-temporal correlations play a crucial role in the coherent control of short pulses transmitting through an MMF. The positive correlations among spatial channels enable a global enhancement of transmitted energy at a selected arrival time by shaping the incident wavefront. Experimentally, we achieve a higher enhancement when the target time is before or after the mean arrival time, as a result of stronger long-range correlations. Theoretically, we provide a quantitative relation between spatio-temporal correlations and the time-dependent enhancement of transmitted power, which agrees well with our experimental data. Our results show that the maximal power that can be delivered through an MMF at a well-defined time is much higher than what is achievable without long-range correlations.

4.2 Correlations

In this section, we review the mathematics behind the known static correlations in disordered media, and then discuss their consequences for the spatio-temporal correlations in MMFs.

The propagation of monochromatic light through a system with N input and N output channels is described by an N-by-N transmission matrix u, where the matrix element u_{ba} is the flux-normalized field transmission coefficient from input channel a to transmitted channel b. We denote $U_{ba} \equiv |u_{ba}|^2$. We consider the singular-value decomposition $u = W\sqrt{\tau}V^\dagger$; here W and V are N-by-N unitary matrices, and τ is a diagonal matrix whose elements $\{\tau_n\}_{n=1}^{N}$ are the eigenvalues of $u^\dagger u$. For disordered media, the intensity correlation between the transmitted speckles is defined in channel space as

$$C_{aa',bb'} \equiv \frac{\langle U_{ba} U_{b'a'} \rangle}{\langle U_{ba} \rangle \langle U_{b'a'} \rangle} - 1 \tag{4.1}$$

where $\langle \cdots \rangle$ denotes ensemble average over different disorder realizations. If the matrices u are isotropic, the correlations must take on the form [6, 30]

$$C_{aa',bb'} = \delta_{aa'}\delta_{bb'} C_1 + (\delta_{aa'} + \delta_{bb'}) C_2 + C_3, \tag{4.2}$$

where the constants C_1, C_2, C_3 are commonly referred to as the magnitudes of the short-range, long-range, and infinite-range correlations. Typically $C_1 \gg C_2 \gg C_3$. Mathematically, the transmission matrices u are "isotropic" when the matrices W and V are sampled uniformly and independently from the space of all random unitary matrices in the ensemble average. Physically, isotropy means that all input modes and all output modes are fully mixed, and that all modes are statistically equivalent.

Spatially, a similar structure emerges for intensity correlation function. Denote $I(\mathbf{r}_b, \mathbf{r}_a)$ as the transmitted intensity at position $\mathbf{r}_b$ on the back surface given a point-source excitation at position $\mathbf{r}_a$ on the front surface. For isotropic disordered media, the correlation between $I(\mathbf{r}_b, \mathbf{r}_a)$ and $I(\mathbf{r}_{b'}, \mathbf{r}_{a'})$ takes on the form [31, 32]

$$\begin{aligned} C(\mathbf{r}_{a'} - \mathbf{r}_a, \mathbf{r}_{b'} - \mathbf{r}_b) = [F(\mathbf{r}_{a'} - \mathbf{r}_a) F(\mathbf{r}_{b'} - \mathbf{r}_b)] C_1 \\ + [F(\mathbf{r}_{a'} - \mathbf{r}_a) + F(\mathbf{r}_{b'} - \mathbf{r}_b)] C_2 + C_3, \end{aligned} \tag{4.3}$$

where the coefficients C_1, C_2 and C_3 are the same as in Eq. (4.2). Given a fixed input such that $\mathbf{r}_{a'} = \mathbf{r}_a$, we obtain

$$\frac{\langle I(\mathbf{r}) I(\mathbf{r} + \Delta\mathbf{r}) \rangle}{\langle I(\mathbf{r}) \rangle \langle I(\mathbf{r} + \Delta\mathbf{r}) \rangle} - 1 = F(\Delta\mathbf{r}) \tilde{C}_1 + \tilde{C}_2, \tag{4.4}$$

where we define $\tilde{C}_1 \equiv C_1 + C_2 \approx C_1$ and $\tilde{C}_2 \equiv C_2 + C_3 \approx C_2$. The constant $\tilde{C}_1$ gives the strength of short-range correlation, as the normalized function $F(\Delta\mathbf{r})$ decays to zero at the distance $|\Delta\mathbf{r}|$ larger than the speckle size [33]. The constant $\tilde{C}_2$ represents the long-range correlation that results from path crossings [2,5] and is independent of distance.

The statistics of the transmission eigenvalues uniquely determines the magnitudes of the correlations. It was shown rigorously that [6,30]

$$\begin{aligned}
C_1 &= \frac{N^2(N^2+1)}{(N^2-1)^2}\left(\frac{\langle\alpha^2\rangle}{\langle\alpha\rangle^2} - \frac{2N}{N^2+1}\frac{\langle\alpha_2\rangle}{\langle\alpha\rangle^2}\right), \\
C_2 &= \frac{N^2(N^2+1)}{(N^2-1)^2}\left(\frac{\langle\alpha_2\rangle}{\langle\alpha\rangle^2} - \frac{2N}{N^2+1}\frac{\langle\alpha^2\rangle}{\langle\alpha\rangle^2}\right), \\
C_3 &= C_1 - 1,
\end{aligned} \tag{4.5}$$

where $\alpha \equiv \sum_{n=1}^{N} \tau_n$ and $\alpha_2 \equiv \sum_{n=1}^{N} \tau_n^2$.

Pulsed inputs introduce time dependences and non-trivial magnifications to the correlations in MMFs. We consider correlations of the transmitted intensity $I(\mathbf{r}, t)$ between different output positions $\mathbf{r}$ and $\mathbf{r} + \Delta\mathbf{r}$ at arrival times t and t',

$$C(\Delta\mathbf{r}, t, t') \equiv \frac{\langle I(\mathbf{r}, t) I(\mathbf{r} + \Delta\mathbf{r}, t')\rangle}{\langle I(\mathbf{r}, t)\rangle\langle I(\mathbf{r} + \Delta\mathbf{r}, t')\rangle} - 1. \tag{4.6}$$

In the $t = t'$ case, when $C(\Delta\mathbf{r}, t, t)$ is positive, the transmitted power at time t can be efficiently enhanced by wavefront shaping, since enhancing the intensity at one position will simultaneously enhance the intensities at other positions. If the time-dependent transmission matrix at arrival time t is sufficiently isotropic, we expect the same structure as Eq. (4.3). When $t \neq t'$, the correlation governs the transmitted intensities at time t when the transmission at time t' is modified by changing the incident wavefront; therefore it is related to the temporal shape of the output pulse when the transmitted power is optimized at a given time.

4.3 Time-resolved transmission matrix

To characterize such spatio-temporal correlation, we measure the transmission matrix of an MMF with strong mode mixing. We use an off-axis holographic setup schematically shown in Fig. 4.1(a). A spatial light modulator (SLM; Hammamatsu X10468) scans the incident angle of a laser beam (Agilent 81940A) onto the MMF, to excite different spatial modes with horizontal polarization. The plane wave of the reference arm and the light transmitted through the fiber interfere to form fringes on the camera, from which we extract the horizontally polarized transmitted field. We use a one-meter-long 0.22-NA graded-index fiber with a core radius of 50 μm and 84 guided modes per polarization. To introduce strong mode mixing into such a short fiber, we use clamps to create micro-bendings. The path lengths of the two arms are matched so the mean arrival time of the pulse (relative to the reference) is zero. The spectral correlation width of the fiber is 0.20 nm at the wavelength of 1550 nm. We measure the field transmission matrices over a wavelength range of 6.4 nm with a step of 0.04 nm. We then perform a Fourier transform to obtain the time-dependent transmission matrices $u(t)$ relating the incident wavefront $|\psi_{\text{in}}\rangle$ to the transmitted wavefront $|\psi_{\text{out}}(t)\rangle = u(t)|\psi_{\text{in}}\rangle$ at different arrival times t, considering a Gaussian transform-limited input pulse centered at wavelength 1550 nm with a full width at half maximum (FWHM) of 2.0 nm (temporal FWHM = 2.6 ps). The input bandwidth is 10 times of the spectral correlation width of the fiber. Thus for random input wavefronts the transmitted pulse would be 10 times longer than the input pulse.

The total output intensity at time t is $\langle\psi_{\text{out}}(t)|\psi_{\text{out}}(t)\rangle = \langle\psi_{\text{in}}|u^\dagger(t)u(t)|\psi_{\text{in}}\rangle$. The mean eigenvalue of $u^\dagger(t)u(t)$, shown in Fig. 4.1(b), represents the total transmitted power for random spatial input wavefronts as a function of arrival time t. Comparing to the input pulse width (Fig. 4.1(b), black dotted line), the output pulse is significantly stretched and distorted due to strong modal dispersions that different modes propagate at different group delays. The strong random mode coupling is

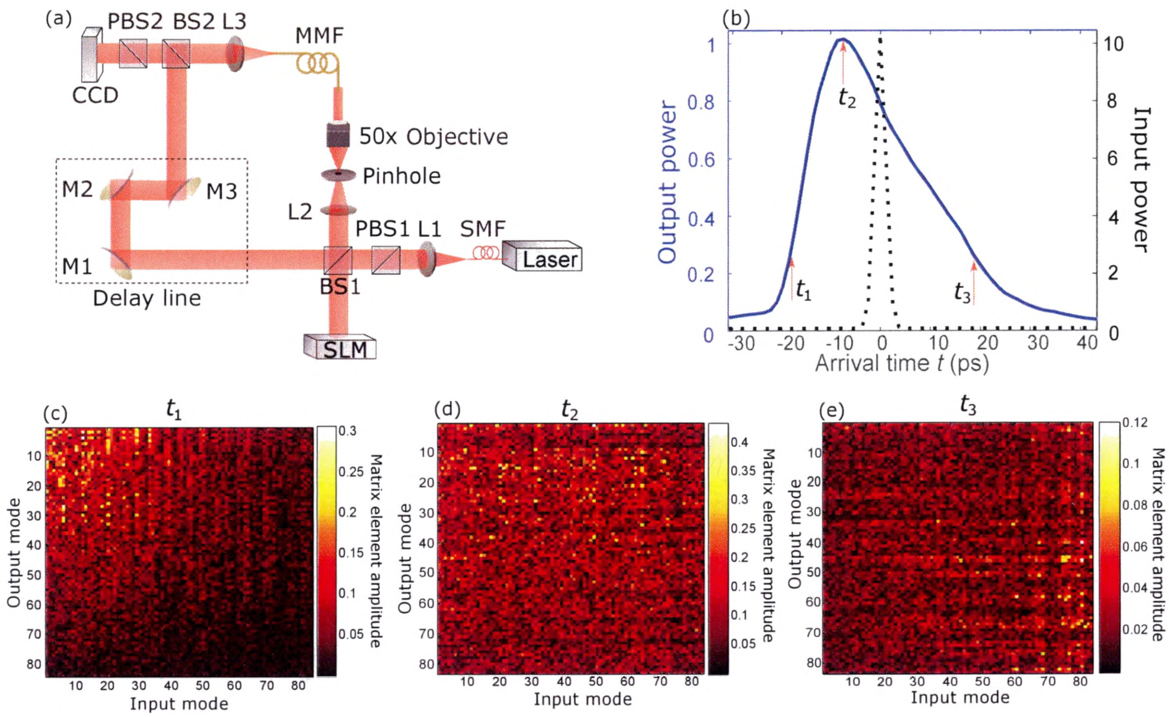

Figure 4.1: Time-dependent transmission matrices of a multimode fiber. (a) Schematics of experimental setup for both transmission matrix measurement and wavefront shaping. A laser beam with tunable frequency is collimated, and its horizontal polarization is selected and split into two arms, with one being the reference and the other propagating through the MMF after reflecting off a spatial light modulator (SLM). The SLM is demagnified and imaged onto the MMF facet. Light transmitted through the MMF is recombined with the reference plane wave, and its horizontal polarization is imaged onto a CCD camera. The path lengths of the two arms are matched by tuning the delay line formed by mirrors M1–M3. L, lens; BS, beam splitter; PBS, polarizing beam splitter. (b) Temporal shapes of the input pulse (black dotted line, right axis) and the mean eigenvalue of $u^{\dagger}(t)u(t)$ (blue solid line, left axis) representing the transmitted intensities of random spatial inputs. The two curves are normalized to have the same area. (c-e) Magnitudes of the measured time-dependent transmission matrices at three arrival times (marked by red arrows in (b)), showing strong mode mixing in the fiber. The transmission matrices are measured in $\mathbf{k}$ space at input and real space $\mathbf{r}$ at output, and subsequently converted to the fiber mode basis.

evident from the magnitude of the time-dependent transmission matrix, shown in Fig. 4.1(d) for central arrival time; no matter which mode is launched at the input, light is scattered to all spatial modes at the output. The absence of a dominant diagonal reveals negligible ballistic light at fiber output. The transmission matrix at early (late) arrival time in Fig. 4.1(c) (Fig. 4.1(e)) has larger contributions from lower-order (higher-order) modes which have shorter (longer) group delay.

Now we discuss the isotropic approximation of the time-resolved transmission matrix. At the central (mean) arrival time, the higher-order modes have slightly smaller magnitude than the lower-order modes (Fig. 4.1(d)). This is caused by the mode-dependent-loss (MDL) in the fiber. Even with strong mode coupling, the distribution of mode intensities depends on the relative strength of mode coupling and MDL. Since random mode coupling can be regarded as scattering in the fiber mode space, we define the transport mean free path l_t as the propagation length at which light originally injected to a single fiber mode is scattered to all spatial modes. If the fiber length $L \gg l_t$ and l_t is much smaller than the absorption length l_a for any fiber mode, mode mixing dominates over dissipation, then all modes would have similar magnitudes. However, such conditions are not met for the multimode fiber in our experiment. Because the higher-order modes experience significantly more loss, they have shorter l_a than the lower-order modes. As their l_a becomes shorter than l_t, the higher-order modes dissipate faster than mode coupling. Thus their magnitudes become smaller than those of the lower-order modes.

Furthermore, Fig. 4.1(c) shows the transmission matrix at early arrival time has more contributions from the lower-order modes than the higher-order modes. In order to have a short delay, the pulse must travel mostly in the lower-order modes that have smaller group delay. Thus the lower-order modes contribute more to the transmission matrix at earlier arrival time. Similarly, the higher-order modes contribute more to the transmission matrix at later arrival times. Therefore, even if the mode-dependent

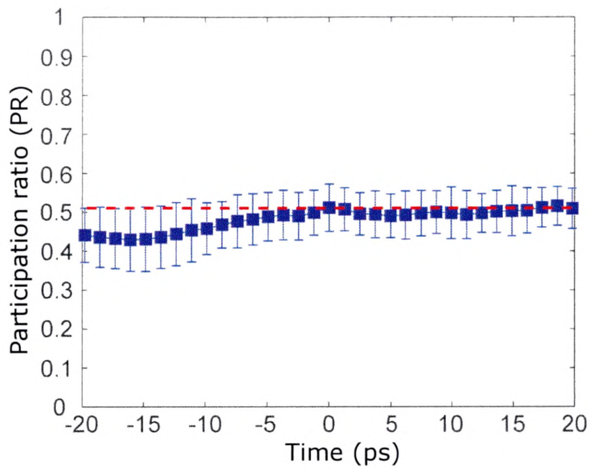

Figure 4.2: Participation ration (PR) of the time-resolved transmission matrices at different arrival times. The error bar is the standard deviation for different input modes at a fixed arrival time. Red dashed line: the PR of isotropic random matrices.

loss is negligible, the transmission matrices at very early or very late arrival times are not expected to be isotropic.

Clearly "isotropy" is an approximation for the time-resolved transmission matrices. To check how good the approximation is, we compute the participation ratio PR $= \frac{(\sum_{i=1}^{N} I_i)^2}{N\sum_{i=1}^{N} I_i^2}$, where I_i is the transmitted intensity in mode i. The larger the PR, the more uniform the transmitted light is spread to all modes. For the measured transmission matrix at a fixed delay time, we calculate the PR for light injected to each fiber mode (each column) and average the PR over all input modes (all columns). To quantify the fluctuations of PR for different input modes, we compute the standard deviation of PR for all columns of the transmission matrix. The mean value and the standard deviation of PR are plotted versus the arrival time in Fig. 4.2. For comparison, we also compute the PR for isotropic random matrices. Each column of the matrix is normalized to unity and consists of N complex numbers that are randomly chosen from the normal distribution. The ensemble-averaged PR is 0.51. The mean value of PR at different arrival times is fairly close to 0.51 (red dashed line) in Fig. 4.2. Hence, isotropy is a good approximation for the time-resolved transmission matrices of our fiber within the measurement range of delay times.

4.4 Measured long-range spatio-temporal correlation

We calculate the spatio-temporal correlations $C(\Delta\mathbf{r}, t, t')$ from the measured time-dependent transmission matrices, replacing the ensemble average in Eq. (4.4) with an average over random input spatial profiles. Figure 4.3(a)-(b) plot $C(\Delta r, t) \equiv C(|\Delta\mathbf{r}|, t, t' = t)$ and two cross sections of it along Δr at $t = -17.3$ ps and $t = 3.7$ ps. We observe a short-range correlation that starts from one and vanishes at the speckle size of about 3 μm, beyond which we see a long-range correlation that is approximately constant with respect to Δr. This indicates $C(\Delta r, t) = F(\Delta r)C_1(t)+C_2(t)$, consistent with Eq. (4.3). Figure 4.3(c) shows the arrival-time dependence of the long-range correlation $C_2(t)$; it is small at the central arrival time but increases toward early or late arrival times.

The time dependence of $C_2(t)$ can be understood through the optical path-length distribution in the multimode fiber. Due to strong mode coupling, there are numerous paths that light can take to travel through the fiber. By exciting the fiber with many random incident wavefronts, all paths are explored and the averaged temporal shape of transmitted pulse in Fig. 4.1(b) reflects the number of propagation paths with varying lengths. The larger $C_2(t)$ at early and late arrival times is consistent with the lower number of paths for such times. Conceptually, if there is only one path of length corresponding to the arrival time t, the output intensities $I(\mathbf{r}, t)$ at different positions $\mathbf{r}$ must be fully correlated: varying the incident wavefront can only change how much light is coupled into that one path, which will increase or decrease $I(\mathbf{r}, t)$ at all positions in the same way. Therefore, the fewer paths for the arrival time t, the stronger $C_2(t)$.

Long-range correlation between far-away speckle grains exists not only between speckle grains at the same arrival time, but also between speckle grains at different

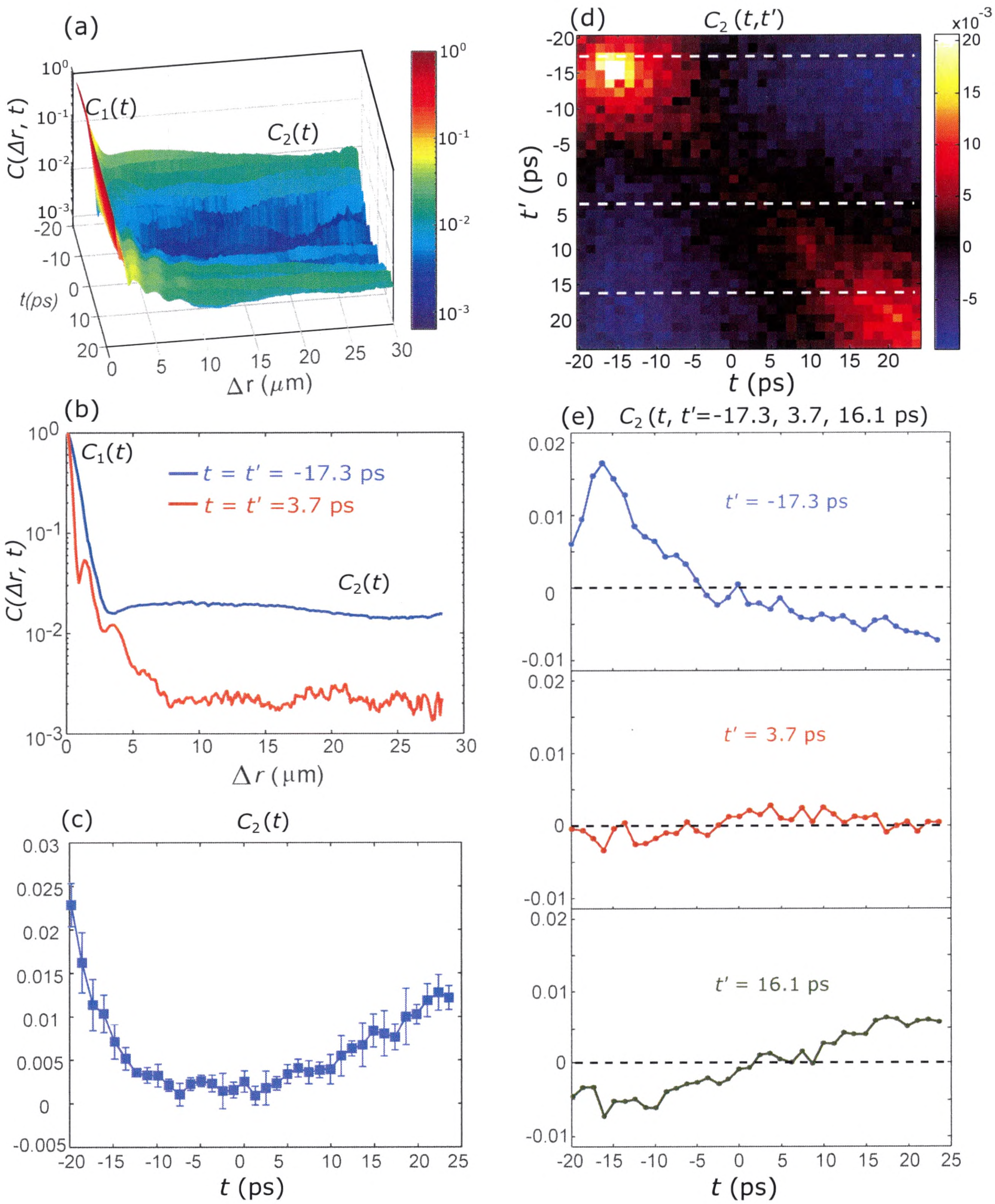

Figure 4.3: Spatio-temporal correlations in MMF with strong random mode mixing. (a) Intensity correlations $C(\Delta r, t) \equiv C(|\Delta \mathbf{r}|, t, t' = t)$, revealing a short-range component $C_1(t) \approx 1$ at spatial distance within one speckle ($\Delta r \lesssim 3$ μm) and a long-range component $C_2(t)$ that persists at large distance. (b) Two cross sections of $C(\Delta r, t)$ at arrival times $t = -17.3$ ps and $t = 3.7$ ps. (c) Time dependence of the long-range component $C_2(t)$, averaging over Δr for $\Delta r > 5$ μm. (d) Long-range correlations $C_2(t, t')$ between spatio-temporal speckle grains at different arrival times t and t'. (e) Cross sections of $C_2(t, t')$ at $t' = -17.3$ ps, 3.7 ps and 16.1 ps (marked by white dashed lines in (d)).

arrival times. This is quantified by $C(\Delta\mathbf{r}, t, t')$ as defined in Eq. (4.6). At large $|\Delta\mathbf{r}|$, this quantity again becomes independent of $|\Delta\mathbf{r}|$ and approaches the asymptotic value $C_2(t, t')$. In Fig. 4.3(d), we show $C_2(t, t')$ for t and t' from -20 ps to 25 ps. The long-range correlation is positive close to the diagonal, namely close to the $C_2(t)$ discussed earlier. When t and t' are far apart, however, the long-range correlation becomes negative. Fig. 4.3(e) show three cross-sections. Near the central arrival time ($t' = 3.7$ ps), $C_2(t, t')$ is close to zero at all t. Meanwhile, at $t' = -17.3$ ps, $C_2(t, t')$ peaks at $t \approx t'$ and decays away from it, eventually becoming negative. The trend, however, is opposite at $t' = 16.1$ ps. The correlation is negative at early delay times and becomes positive at late arrival time. Such a negative correlation is a result of the conservation of transmitted pulse energy, which requires an increase of spatially integrated intensity (power) at arrival time $t = t'$ to be compensated by a decrease of power at other arrival times.

The positive spatio-temporal correlation $C_2(t)$ at early or late arrival times will lead to a higher achievable enhancement at such times. Because the matrix $u^\dagger(t_0)u(t_0)$ is Hermitian, the global optimum, which determines the maximum power that can be delivered at time t_0, is given by the largest eigenvalue of $u^\dagger(t_0)u(t_0)$, and the corresponding eigenvector is the desired incident wavefront [21]. By shaping the incident wavefront with the SLM [34, 35], we can enhance the total transmitted power at a target arrival time and compensate for the strong modal dispersion in the fiber. Experimentally, we determine such optimal transmission channels from the measured time-dependent transmission matrices, and then generate the desired wavefront with the same setup, using computer-generated phase holograms to simultaneously modulate the phase and amplitude profiles [36]. By scanning the wavelength and Fourier transforming the spectral measurements to the time domain, we obtain the spatially integrated temporal pulse shapes of such optimal transmission channels.

The pulses optimized for arrival times $t_0 = -5$ ps and $t_0 = 16.1$ ps are shown

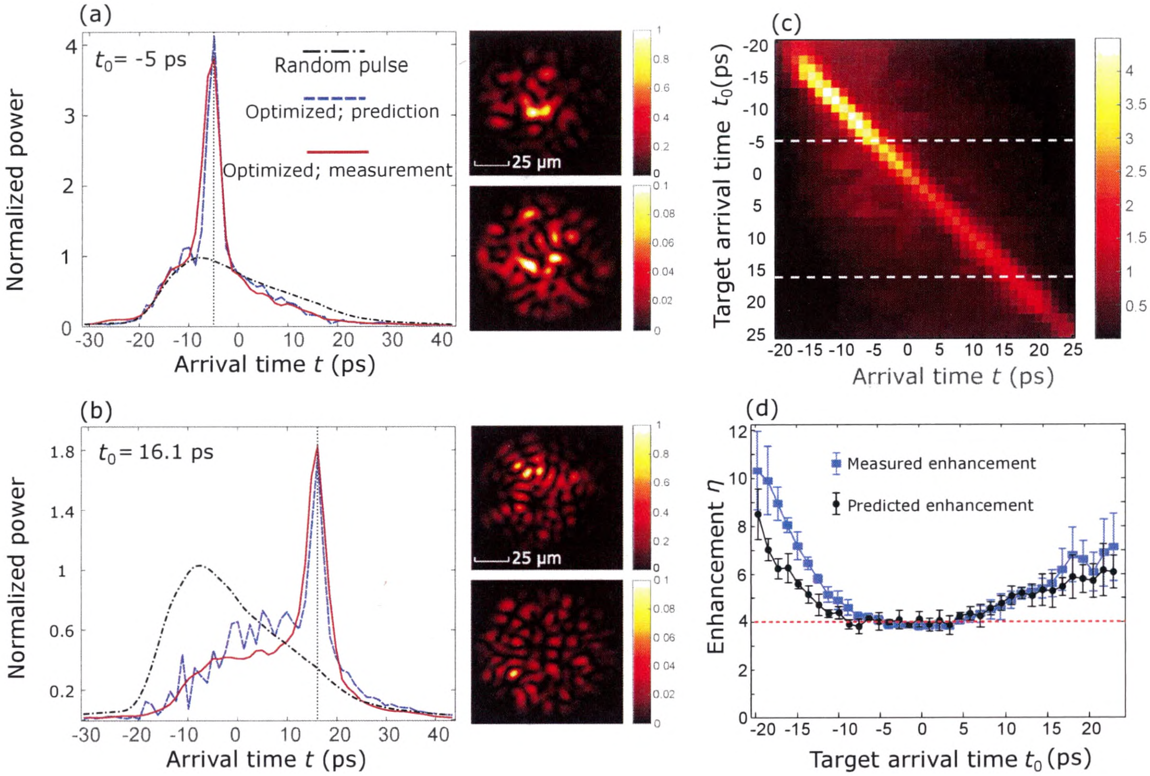

Figure 4.4: Enhancing transmitted power at selected arrival time. (a-b) Temporal shapes of the output pulse when the spatially integrated intensity (power) is optimized at arrival time (a) t_0 = -5 ps and (b) t_0 = 16.1 ps. Red solid lines are the measured pulse shapes with optimized input wavefronts, the blue dotted lines are predicted from measured correlations $C_2(t, t')$. They exhibit strong enhancement compared to the mean eigenvalues of $u^\dagger(t)u(t)$, which represents the mean output pulse shape for random input wavefronts (black dash-dotted lines). Transmitted powers are all normalized by the peak power of the transmitted pulse with random input wavefronts. The insets are spatial intensity patterns at t_0 for the optimized wavefront (upper panel) and a random wavefront (lower panel). The speckle grains at t_0 = - 5 ps are larger than those at t_0 = 16.1 ps, due to larger contributions from the lower-order modes at earlier arrival time. (c) Temporal shapes of pulses optimized at different t_0, ranging from -20 ps to 25 ps. The target time of (a) and (b) are marked by the white dashed lines. (d) Enhancement factor η of the transmitted power at the target arrival time t_0. Blue squares: experimentally measured enhancement. Black circles: enhancement predicted from $C_2(t)$. Error bars represent the standard deviation among four measurements of the fiber in different bending configurations. Red dashed line indicates 4 times enhancement if $C_2(t) = 0$.

in Fig. 4.4(a-b) (red solid curve), in comparison to the averaged pulse of random spatial inputs (black dash-dotted curve). The sharp peak at the selected arrival time, as marked by the vertical black dotted line, illustrates that the transmitted power can be effectively enhanced at different target times, even in the presence of strong modal dispersions in the fiber. The peak width equals the input pulse width. The spatial intensity patterns of the optimized pulse and the non-optimized one at the target arrival times, shown in Fig. 4.4(a-b), are obtained from the Fourier transform of the frequency-resolved field patterns measured with the optimized and random incident wavefronts. It is distinct from spatio-temporal focusing [25, 37–41] where only one speckle is enhanced. Figure 4.4(b) shows that the transmitted power after the target time increases, but well before the target time it decreases. Such changes are determined by correlation $C_2(t, t' = 16.1\text{ps})$ shown in Fig. 4.3(e). The negative correlation at early arrival time suppresses the background and the positive correlation at late arrival time enhances the background. Figure 4.4(c) plots the pulse shapes optimized for different arrival times from t_0 = -20 ps to 25 ps. The peak follows the target time t_0, and notably, the background also shifts with the target time.

4.5 Pulse delivery enhancement factor

To evaluate the effectiveness of the transmitted power optimization, we define an enhancement factor $\eta(t_0) \equiv I_{\text{enh}}(t_0)/I_{\text{random}}(t_0)$, where $I_{\text{enh}}(t_0)$ and $I_{\text{random}}(t_0)$ are the spatially integrated intensities of the optimized pulse and the random pulse at the target time t_0. We plot the measured enhancement factor η (blue square) in Fig. 4.4(d). The standard deviation of the enhancement between measurements on four different days is shown by the error bars. The deviation is larger at early or late arrival times as the weaker pulse intensities there lead to smaller signal-to-noise ratio. The average enhancement is about 4 times around the central arrival time, which is what one expects through the quarter-circle law for the singular values of a square random matrix with uncorrelated elements [42]. At early or late arrival times, we achieve power enhancements much larger than 4; such increase is consistent with the large long-range correlation $C_2(t)$ that we observed (Fig. 4.3(c)).

Finally, we provide a quantitative connection between the long-range spatio-temporal correlation $C_2(t)$ and the enhancement factor $\eta(t_0)$ of transmitted power at arrival time t_0. We use a heuristic model similar to that employed in Ref. [22], capturing the correlation between output channels at arrival time t_0 through a reduction in the effective number of output channels. Specifically, we consider an effective random matrix with N input channels and $N^{(\mathrm{eff})}(t_0)$ output channels, and we consider all elements of this matrix to be identically independently distributed. The enhancement η is determined by the largest eigenvalue, which is related to the spread of the eigenvalues characterized by the eigenvalue variance. As detailed in the Supplementary Section I, the normalized eigenvalue variance associated with the reduced matrix is given by the Marčhenko–Pastur distribution [42] to be $N/N^{(\mathrm{eff})}(t_0)$, while that associated with the actual time-resolved transmission matrix is $1 + NC_2(t_0)$. Therefore, we choose

$$N^{(\mathrm{eff})}(t_0) = \frac{N}{1 + NC_2(t_0)} \tag{4.7}$$

to match the two corresponding eigenvalue variances. This relation quantifies how long-range correlation effectively reduces the number of output channels. The enhancement is the normalized maximal eigenvalue, which for an uncorrelated matrix is $\tau_{\max}/\bar{\tau} = \left(1 + \sqrt{N/N^{(\mathrm{eff})}(t_0)}\right)^2$ (Ref. [42]). Inserting Eq. (4.7), we obtain a simple equation

$$\eta(t_0) = \left(1 + \sqrt{1 + NC_2(t_0)}\right)^2 \tag{4.8}$$

that relates the maximal enhancement to the long-range spatio-temporal correlation.

In Fig. 4.4(d), we compare the measured enhancement to the enhancement predicted through the measured $C_2(t)$ via Eq. (4.8) (black circles). Overall, the two curves agree well, especially around the central arrival time. Some differences at early or late arrival times may be due to the fact that the time-dependent transmission matrix is not as isotropic as that at the central time (as shown in Fig. 4.1(c-e)). We further generalize the relationship in Eq. (4.8) to predict the whole output pulse (both the peak at the target time and the background) via $C_2(t,t')$. We construct a heuristic model based on two observations. First, the normalized power $\eta(t,t_0)$ should be identical to Eq. (4.8) when $t=t_0$. Second, when the correlation $C_2(t,t_0)\approx 0$, the power at t should be equal to that of random incident wavefront, giving $\eta(t,t_0)\approx 1$. To satisfy these two constraints, we propose

$$\eta(t,t_0) = 2C_1(t,t_0) + NC_2(t,t_0) + 2\sqrt{1+NC_2(t,t_0)} - \beta[1-C_1(t,t_0)]. \tag{4.9}$$

$C_1(t,t_0) = 1$ for $t=t_0$, and $C_1(t,t_0)=0$ for $t\neq t_0$. The parameter β is chosen such that the temporally-integrated output power (pulse energy) equals that from a random input. From numerical simulations of a multimode waveguide without loss, we find that $\beta\approx 1$. With loss, both numerical and experimental results confirm that Eq. (4.9) is still an excellent model with $\beta=1$.

In Figs. 4.4(a-b), we plot the predicted temporal shapes (blue dotted curves) of the optimized pulses with $t_0=-5$ ps and $t_0=16.1$ ps on top of the measured pulse shapes. As $C_2(t,t_0)$ changes from positive correlation for the arrival time t close to the target time t_0 to negative correlation for t far from t_0, the transmitted power is enhanced near the peak at t_0 and suppressed away from the peak. Consequently, the background shifts toward the peak due to long-range correlation.

Local and nonlocal correlations have been studied extensively in scattering media, but there are few observations in other complex photonic systems. Short-range correlation introduces the rotational memory effect that has been observed in an

MMF with weak mode coupling [43]. Here we observe long-range spatio-temporal correlation in a multimode fiber with strong mode mixing when a pulse propagates through the fiber. The correlation not only determines the effectiveness of enhancing the transmitted power at a target time, but also captures the temporal shape of the resulting pulse. Enhancing the transmitted power in time can be utilized in many fiber applications from communication to imaging. The maximum eigenmode (EM) of the time-resolved transmission matrix provides the incident wavefront for focusing the transmitted pulse to a chosen delay time. This method is effective for any input pulse with arbitrarily broad spectrum, and it guarantees the maximal power delivery at any selected time. Especially when the spectral width of an input pulse is much larger than the spectral correlation width of the fiber, the EM outperforms the principal mode (PM) and super-principal mode (SPM) in achieving the highest peak power of the transmitted pulse, as we will show in the following section.

4.6 Comparison to principal modes

As we discussed in chapter 2, PMs are the eigenmodes of the time-delay matrix for a multimode fiber. It retains the transmitted spatial field profile to the first order of frequency variation. If random mode coupling is strong in a fiber ($L \gg l_t$), the spectral window, over which the transmitted field pattern remains nearly unchanged with frequency, has a width about twice of the spectral correlation width of the fiber. To further enhance spectral correlation, in chapter 3, SPMs are created by minimizing the variation of output field pattern with frequency, i.e., by maximizing the area underneath the curve for the spectral correlation function over a chosen frequency range. The spectral bandwidth of the SPM is about four times of the spectral correlation width of the fiber with strong mode mixing. Both PMs and SPMs aim to achieve an output spatial profile that is invariant in frequency so that

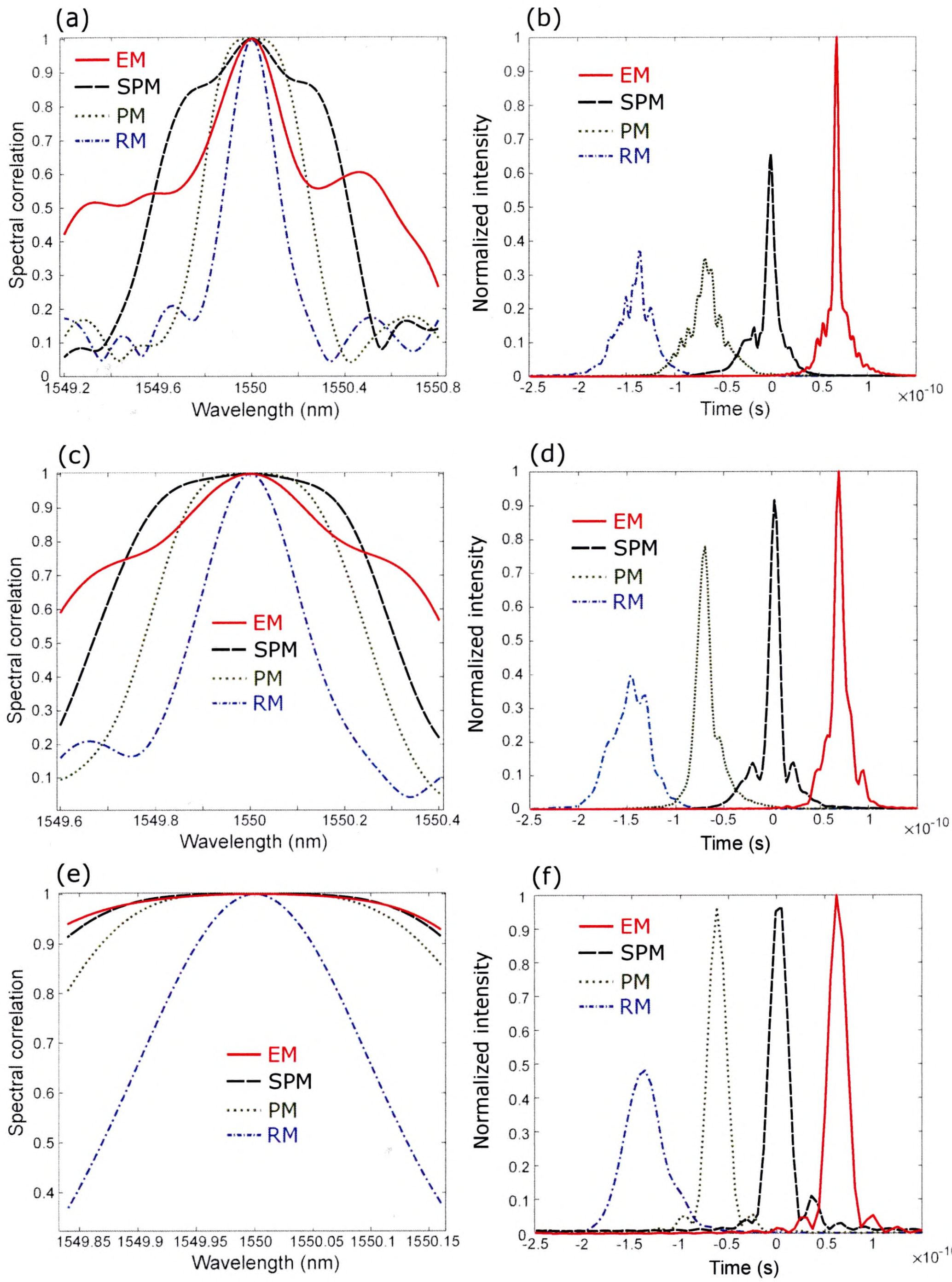

Figure 4.5: Spectral correlation function $C(\Delta\lambda)$ of the output field pattern and the corresponding temporal pulse shape when the input pulse has the spatial wavefront set by an EM, SPM, PM and random wavefront (RM). The input pulse is transform-limited and has a Gaussian spectrum of width equal to (a, b) 10, (c, d) 5 and (e, f) 2 times of the spectral correlation width of the multimode waveguide. For clarity, the transmitted pulses are temporally off-set by 70 ps in (b, d, f).

the output field pattern does not change with the arrival time and maintains the spatial coherence; however, the transmitted power is not necessarily maximized at any arrival time.

The EM with the maximum eigenvalue of the time-resolved transmission matrix generates the highest possible transmitted power at the selected arrival time. It works for input pulses with arbitrarily broad spectra. Therefore, PM, SPM and EM are all suppressing modal dispersion in the fiber, but for different purposes and thus optimizing the incident wavefront with different figures of merit.

Below we compare the spectral correlation and temporal pulse shape of the PM, SPM, EM and random wavefront (RM) for varying bandwidths of the input pulse. Numerically we simulate a multimode waveguide with the concatenated model [44]. The input pulse is assumed to have a Gaussian spectrum. Its spectral width is varied from 2, 5 and 10 times of the correlation width of the fiber (for random incident wavefronts). The spectral correlation function for the transmitted field pattern $|\psi_{out}\rangle$ is given by $C(\Delta\lambda \equiv \lambda - \lambda_0) \equiv \langle\psi_{out}(\lambda_0)|\psi_{out}(\lambda)\rangle$, where $|\psi_{out}\rangle$ is normalized at each wavelength λ.

Figure 4.5 presents the results for three bandwidths of input pulses, which are transform-limited. For the EM, t_0 is set to the mean arrival time. The PM and SPM are chosen to have the intermediate delay time and the broadest bandwidth. When the input bandwidth is 10 times of the spectral correlation width of the fiber (as studied in our experiment), EM clearly outperforms PM and SPM in both the frequency domain and the time domain (a,b). The total area underneath the curve of the spectral correlation function for EM is the largest, indicating the overall spectral decorrelation within the broad range is the least for EM (a). Temporally, EM achieves the highest peak power of the transmitted pulse (b). When the input bandwidth is reduced to 5 times of the spectral correlation width (c,d), the PM still displays notable spectral decorrelation and the output pulse is clearly broadened in time. The SPM and EM are effective in suppressing spectral decorrelation (c) and temporal stretching (d), but EM still outperforms SPM slightly. Only when the input spectrum is reduced to twice of the spectral correlation width of the fiber (e,f), PM, SPM and EM achieve almost equivalent performances. In the frequency domain, PM, SPM and EM barely decorrelate, contrary to RM (e). In the time domain, the output pulse for RM is about twice longer than the input pulse. In contrast, PM, SPM and EM all have transmitted pulses of length comparable to the incident pulse (f).

4.7 Relation between time-dependent transmission matrix and time-delay operator

[2]In this section, we present the connection between the operator $u^\dagger(t)u(t)$ with $u(t) = \int f(\omega)u(\omega)e^{-i\omega t}d\omega$ and the time-delay operator in case of a narrow frequency range. Using the normalized spectral function:

$$f(\omega) = \begin{cases} \frac{1}{\Delta\omega} & \omega_0 - \frac{\Delta\omega}{2} \leq \omega \leq \omega_0 + \frac{\Delta\omega}{2} \ , \\ 0 & \text{otherwise} \ , \end{cases} \tag{4.10}$$

and considering $\Delta\omega$ small we can approximate the integral by

$$u(t) = \Delta\omega \cdot \frac{1}{2} \cdot \frac{1}{\Delta\omega} \left[u(\omega_0 - \Delta\omega/2)e^{-i(\omega_0 - \Delta\omega/2)t} + u(\omega_0 + \Delta\omega/2)e^{-i(\omega_0 + \Delta\omega/2)t} \right] . \tag{4.11}$$

Next, using $u^\dagger(\omega)u(\omega) = \mathbb{1}$ we can write

$$\begin{aligned} u^\dagger(t)u(t) = \frac{1}{4} \Big[& 2 + u^\dagger(\omega_0 - \Delta\omega/2)u(\omega_0 + \Delta\omega/2)e^{-i\Delta\omega t} \\ & + u^\dagger(\omega_0 + \Delta\omega/2)u(\omega_0 - \Delta\omega/2)e^{i\Delta\omega t} \Big] . \end{aligned} \tag{4.12}$$

2. This derivation is provided by Matthias Kuehmayer and Jakob Melchard.

Due to the narrow frequency range, we can expand the above quantities around the center frequency ω_0

$$u(\omega_0 \pm \Delta\omega/2) = u(\omega_0)\left[\mathbb{1} \pm \frac{i\Delta\omega}{2}Q + \frac{\Delta\omega^2}{8}\left(i\frac{dQ}{d\omega} - Q^2\right)\right], \tag{4.13}$$

$$e^{\pm i\Delta\omega t} = 1 \pm i\Delta\omega t - \frac{\Delta\omega^2 t^2}{2}, \tag{4.14}$$

where $Q = -iu^{-1}(\omega_0)\frac{du}{d\omega}(\omega_0)$ is the time-delay operator. Thus, we find

$$u^\dagger(\omega_0 \pm \Delta\omega/2)u(\omega_0 \mp \Delta\omega/2) = \mathbb{1} \pm i\Delta\omega Q - \frac{\Delta\omega^2}{2}Q^2 \tag{4.15}$$

and multiplying this with the corresponding exponential function yields

$$u^\dagger(\omega_0 \pm \Delta\omega/2)u(\omega_0 \mp \Delta\omega/2)e^{\pm i\Delta\omega t} = \mathbb{1} \pm i\Delta\omega(t-Q) - \frac{\Delta\omega^2}{2}(t-Q)^2 . \tag{4.16}$$

We arrive at

$$\begin{aligned} u^\dagger(t)u(t) &= \frac{1}{4}\left[4 - \Delta\omega^2(t-Q)^2\right] \\ &= \mathbb{1} - \left(\frac{\Delta\omega}{2}\right)^2 (t-Q)^2 . \end{aligned} \tag{4.17}$$

Since $[u^\dagger(t)u(t), Q] = 0$, these operators share the same eigenbasis. This can also be seen by letting $u^\dagger(t)u(t)$ act on a time-delay eigenstate $|q_n\rangle$ with $Q|q_n\rangle = \tau_n|q_n\rangle$,

$$u^\dagger(t)u(t)|q_n\rangle = \left[\mathbb{1} - \left(\frac{\Delta\omega}{2}\right)^2 (t-\tau_n)^2\right]|q_n\rangle = \lambda_n|q_n\rangle, \tag{4.18}$$

and thus the eigenvalue of $u^\dagger(t)u(t)$ is given by

$$\lambda_n = \mathbb{1} - \left(\frac{\Delta\omega}{2}\right)^2 (t-\tau_n)^2 . \tag{4.19}$$

Bibliography

[1] W. Xiong, C. W. Hsu and H. Cao, Long-range spatiotemporal correlations in multimode fibers for pulse delivery, Nat. Commun. **10**, 2973 (2019).

[2] E. Akkermans and G. Montambaux, Mesoscopic physics of electrons and photons, (Cambridge Univ. Press, 2007)

[3] P. Sheng, Introduction to wave scattering, localization and mesoscopic phenomena 2nd edn (Springer 2006).

[4] M. J. Stephen and G. Cwilich, Intensity correlation functions and fluctuations in light scattered from a random medium, Phys. Rev. Lett. **59**, 285 (1987).

[5] S. Feng, C. Kane, P. A. Lee and A. D. Stone, Correlations and fluctuations of coherent wave transmission through disordered media, Phys. Rev. Lett. **61**, 834 (1988).

[6] P. A. Mello, E. Akkermans and B. Shapiro, Macroscopic approach to correlations in the electronic transmission and reflection from disordered conductors. Phys. Rev. Lett. **61**, 459 (1988).

[7] P. Sebbah, R. Pnini and Genack, A. Z. Field and intensity correlation in random media, Phys. Rev. E **62**, 7348 (2000).

[8] P. Sebbah, B. Hu, A. Z. Genack, R. Pnini and B. Shapiro, Spatial-field correlation: the building block of mesoscopic fluctuations, Phys. Rev. Lett. **88**, 123901 (2002).

[9] A. García-Martín, F. Scheffold, M. Nieto-Vesperinas and J. J. Sáenz, Finite-size effects on intensity correlations in random media, Phys. Rev. Lett. **88**, 143901 (2002).

[10] S. E. Skipetrov, Enhanced mesoscopic correlations in dynamic speckle patterns, Phys. Rev. Lett. **93**, 233901 (2004).

[11] A. A. Chabanov, B. Hu and A. Z. Genack, Dynamic correlation in wave propagation in random media, Phys. Rev. Lett. **93**, 123901 (2004).

[12] J. Wang, A. A. Chabanov, D. Y. Lu, Z. Q. Zhang and A. Z. Genack, Dynamics of mesoscopic fluctuations of localized waves, Phys. Rev. B **81**, 241101 (2010).

[13] W. K. Hildebrand, A. Strybulevych, S. E. Skipetrov, B. A. Van Tiggelen and J. H. Page, Observation of infinite-range intensity correlations above, at, and below the mobility edges of the 3D Anderson localization transition, Phys. Rev. Lett. **112**, 073902 (2014).

[14] A. Dogariu and R. Carminati, Electromagnetic field correlations in three-dimensional speckles, Phys. Rep,**559**, 1-29 (2015).

[15] F. Riboli, F. Uccheddu, G. Monaco, N. Caselli, F. Intonti, M. Gurioli and S. E. Skipetrov, Tailoring correlations of the local density of states in disordered photonic materials, Phys. Rev. Lett. **119**, 043902 (2017).

[16] I. Starshynov, A. M. Paniagua-Diaz, N. Fayard, A. Goetschy, R. Pierrat, R. Carminati and J. Bertolotti, Non-Gaussian correlations between reflected and

transmitted intensity patterns emerging from opaque disordered media, Phys. Rev. X **8**, 021041 (2018).

[17] O. N. Dorokhov, On the coexistence of localized and extended electronic states in the metallic phase, Solid State Commun. **51**, 381-384 (1984).

[18] Y. V. Nazarov, Limits of universality in disordered conductors, Phys. Rev. Lett. **73**, 134 (1994).

[19] B. Gérardin, J. Laurent, A. Derode, C. Prada and A. Aubry, Full transmission and reflection of waves propagating through a maze of disorder, Phys. Rev. Lett. **113**, 173901 (2014).

[20] R. Sarma, A. G. Yamilov, S. Petrenko, Y. Bromberg and H. Cao, Control of energy density inside a disordered medium by coupling to open or closed channels, Phys. Rev. Lett. **117**, 086803 (2016).

[21] C. W. Hsu, A. Goetschy, Y. Bromberg, A. D. Stone and H. Cao, Broadband coherent enhancement of transmission and absorption in disordered media, Phys. Rev. Lett. **115**, 223901 (2015).

[22] C. W. Hsu, S. F. Liew, A. Goetschy, H. Cao, and A. D. Stone, Correlation-enhanced control of wave focusing in disordered media, Nat. Phys. **13**, 497 (2017).

[23] I. M. Vellekoop and A. P. Mosk, Universal optimal transmission of light through disordered materials, Phys. Rev. Lett. **101**, 120601 (2008).

[24] M. Davy, Z. Shi and A. Z. Genack, Focusing through random media: Eigenchannel participation number and intensity correlation, Phys. Rev. B **85**, 035105 (2012).

[25] Z. Shi, M. Davy, J. Wang and A. Z. Genack, Focusing through random media in space and time: a transmission matrix approach, Opt. Lett. **38**, 2714-2716 (2013).

[26] W. Xiong, C. W. Hsu, Y. Bromberg, J. E. Antonio-Lopez, R. A. Correa and H. Cao, Complete polarization control in multimode fibers with polarization and mode coupling, Light Sci. Appl. **7**, 54 (2018).

[27] P. Chiarawongse, H. Li, W. Xiong, C. W. Hsu, H. Cao and T. Kottos, Statistical description of transport in multimode fibers with mode-dependent loss, New J. Phys. **20**, 113028 (2018).

[28] B. Dietz, H. L. Harney, A. Richter, F. Schäfer and H. A. Weidenmller, Cross-section fluctuations in chaotic scattering, Phys. Lett. B **685**, 263 (2010).

[29] S. Gehler, B. Köber, G. L. Celardo and U. Kuhl, Channel cross correlations in transport through complex media, Phys. Rev. B **94**, 161407 (2016).

[30] P. A. Mello, Averages on the unitary group and applications to the problem of disordered conductors, J. Phys. A **23**, 4061 (1990).

[31] G. Cwilich, L. S. Froufe-Prez and J. J. Sáenz, Spatial wave intensity correlations in quasi-one-dimensional wires, Phys. Rev. E **74**, 045603 (2006).

[32] A. Yamilov, Relation between channel and spatial mesoscopic correlations in volume-disordered waveguides, Phys. Rev. B **78**, 045104 (2008).

[33] J. W. Goodman, Speckle phenomena in optics: theory and applications (Roberts and Company Publishers 2007).

[34] A. P. Mosk, A. Lagendijk, G. Lerosey and M. Fink, Controlling waves in space and time for imaging and focusing in complex media, Nat. Photon. **6**, 283 (2012).

[35] S. Rotter and S. Gigan, Light fields in complex media: Mesoscopic scattering meets wave control, Rev. Mod. Phys. **89**, 015005 (2017).

[36] V. Arrizón, U. Ruiz, R. Carrada, and L. A. González, Pixelated phase computer holograms for the accurate encoding of scalar complex fields, JOSA A **24**, 3500 (2007).

[37] J. Aulbach, B. Gjonaj, P. M. Johnson, A. P. Mosk and A. Lagendijk, Control of light transmission through opaque scattering media in space and time, Phys. Rev. Lett. **106**, 103901 (2011).

[38] O. Katz, E. Small, Y. Bromberg and Y. Silberberg, Focusing and compression of ultrashort pulses through scattering media, Nat. Photon. **5**, 372 (2011).

[39] D. J. McCabe, A. Tajalli, D. R. Austin, P. Bondareff, I. A. Walmsley, S. Gigan and B. Chatel, Spatio-temporal focusing of an ultrafast pulse through a multiply scattering medium, Nat. Commun. **2**, 447 (2011).

[40] M. Mounaix, H. Defienne and S. Gigan, Deterministic light focusing in space and time through multiple scattering media with a time-resolved transmission matrix approach, Phys. Rev. A **94**, 041802 (2016).

[41] I. N. Papadopoulos, S. Farahi, C. Moser and D. Psaltis, Focusing and scanning light through a multimode optical fiber using digital phase conjugation, Opt. Express **20**, 10583-10590 (2012).

[42] V. A. Marčhenko and L. A. Pastur, Distribution of eigenvalues for some sets of random matrices, Math. USSR Sb, **1**, 457 (1967).

[43] L. V. Amitonova, A. P. Mosk and P. W. Pinkse, Rotational memory effect of a multimode fiber, Opt. Express **23**, 20569-20575 (2015).

[44] K. P. Ho and J. M. Kahn, Statistics of group delays in multimode fiber with strong mode coupling, J. Light. Technol **29**, 3119-3128 (2011).

Chapter 5

Complete polarization control in multimode fibers

5.1 Introduction

In the previous chapters, we have demonstrated that spatial degrees of freedom at the input of a multimode fiber can control the temporal profile at the output. [1]In this chapter, we further demonstrate the potential of spatial degrees of freedom in MMFs by spatial-polarization control. The vectorial nature of electromagnetic waves plays an indispensable role in light-matter interaction, optical transmission and imaging. Control over the polarization state of light has been widely exploited in single molecule detection, nanoplasmonics, optical tweezers, nonlinear microscopy and optical coherence tomography. However, a well-prepared state of polarization can be easily scrambled by multiple scattering of light in three-dimensional disordered media. The other side of the coin is that multiple scatterings couple spatial and polarization degrees of freedom, enabling polarization control of the scattered light via wavefront

1. This chapter is primarily based on the work published in ref. [1]. W. Xiong performed the experiment and numerical simulations. C. W. Hsu developed the theory. Y. Bromberg conceived the initial idea. J. E. Antonio-Lopez, R. A. Correa provided the fiber. H. Cao supervised the project.

shaping of the incident beam. Arbitrary polarization states have been attained in a single or a few spatial channels [2–6], transforming the random medium to a dynamic wave plate. For imaging and sensing applications, a full polarization control of all output channels can avoid spatial point scanning and acquire information in parallel. However, it is extremely difficult to control the polarization state of the total transmitted light, and the relatively low transmission through a scattering medium limits the efficiency.

Polarization scrambling also occurs in optical fibers [7]. For a single mode fiber, the output polarization state can be controlled by manipulating the input polarization. Due to refractive index fluctuations introduced by inherent imperfection and environmental perturbation such as eccentricity, bending and twisting, a multimode fiber (MMF) experiences not only polarization mixing but also mode mixing. When light is launched into a single guided mode in the MMF, it will spread to other modes, each of which will experience distinct polarization scrambling. Thus the output polarization state of the modes varies from one mode to another [see Fig. 5.1(a)], prohibiting a control of output polarization states in all modes by adjusting the input polarization of a single mode. One approach to complete polarization control is to measure the full transmission matrix of the MMF and invert it to find the vector fields to be injected into individual modes. This approach requires simultaneous control of both spatial and polarization degrees of freedom at the input, which is technically demanding.

The coupling between spatial and polarization degrees of freedom in an MMF, as in a random scattering medium [8, 9], opens the possibility of utilizing only spatial degrees of freedom of the input wave to control the polarization state of the output field. The key question is whether such a control would be complete, in the sense that not only arbitrary polarization state can be attained for total transmitted light regardless of the input polarization, but also each output mode may have

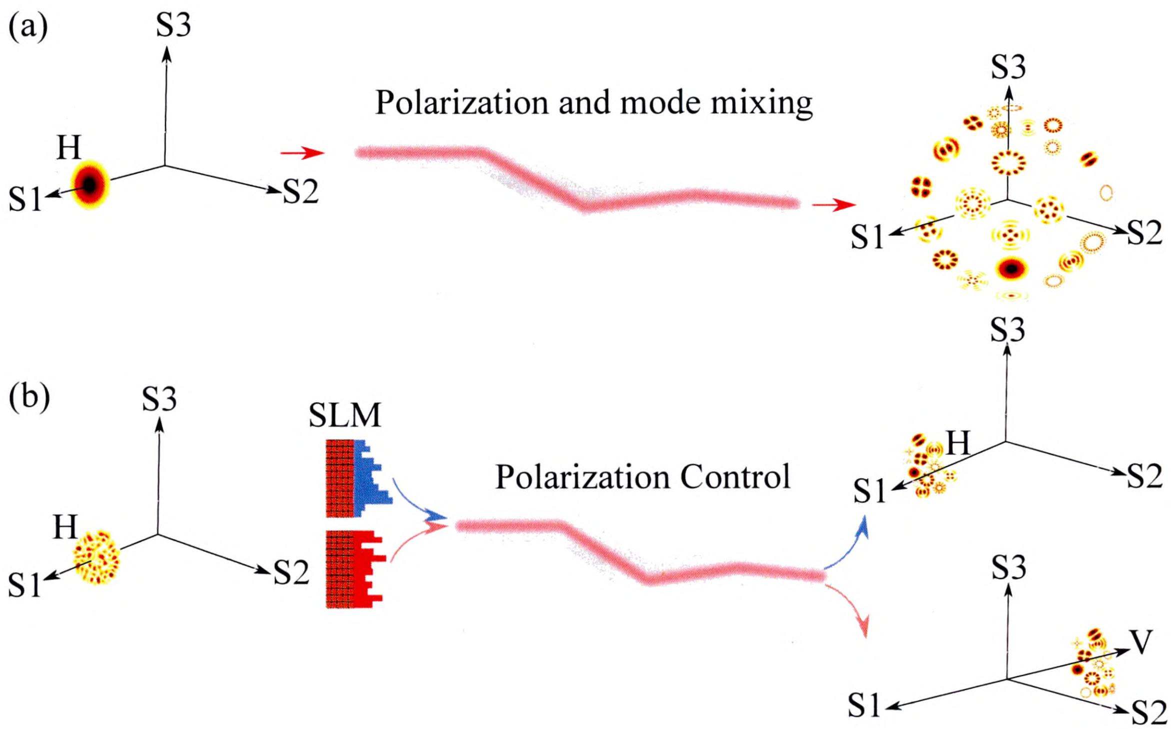

Figure 5.1: [Fiber depolarization and polarization control by wavefront shaping. (a) Light is launched into the fundamental LP mode with the horizontal polarization, and subsequently coupled to other modes with different spatial profiles and polarization states while propagating in the fiber. The transmitted light is composed of all spatial modes in different polarization states, which are randomly spread over the Poincar sphere. (b) Wavefront shaping of the horizontally polarized light by a SLM can overcome depolarization in the fiber, retaining the horizontal polarization for all output modes (top). A different input wavefront can convert all output modes to the vertical polarization (bottom).

a polarization state that differs from each other in a designed manner. If the complete polarization control can be achieved by only shaping the spatial wavefront of an input beam, it would be much easier to realize experimentally, as most spatial light modulators (SLMs) operate for one polarization. A complete control of output polarization states is essential to applications of MMFs in endoscopy [10–18], spectroscopy [19–21], microscopy [22,23], nonlinear optics [24,25], quantum optics [26,27], optical communication [28], and fiber amplifiers [29–31].

Here, in this chapter, we demonstrate the ultimate polarization control of coherent light transmitted through an MMF with strong mode and polarization coupling. By modulating the spatial wavefront of a linearly polarized beam, depolarizations in the MMF is completely eliminated and the transmitted light retains the input polarization. Moreover, a complete conversion of the input polarization to its orthogonal counterpart or any polarization state is achieved. We further tailor the polarization states of individual output channels utilizing spatial degrees of freedom, without constraint on the input polarization state. Our theoretical analysis and numerical modeling illustrate that the full control of polarizations via spatial wavefront shaping is only possible when mode coupling occurs in the fiber. The random mode mixing, often unavoidable in an MMF, can be harnessed for functional advantages. Hence, the wavefront shaping can make an MMF function as a highly efficient reconfigurable matrix of waveplates, converting arbitrary polarization states of the incident field to any desired polarization states.

5.2 Mode coupling for polarization control

To illustrate the critical role played by spatial mode coupling in polarization control, let us first consider an MMF with only polarization mixing but no mode mixing. Linearly polarized (LP) modes are the eigenmodes of a perfect fiber under the weak guiding approximation [32]. The birefringence induced by fiber imperfections and perturbations changes the polarization state. Light injected into each LP mode effectively propagates through a distinctive set of wave plates with random orientations of their optical axes. Eventually different LP modes have different polarizations and the total output field becomes depolarized. In the absence of mode coupling, the MMF behaves like a bundle of uncoupled single mode fibers. It is impossible to control the output polarization of each mode without manipulating their individual input polarizations.

With mode mixing in the fiber, spatial and polarization degrees of freedom become coupled. The output polarization state depends not only on the polarization but also on the spatial wavefront of the input field. For illustration, we consider a fiber with only two modes, each of which has two orthogonal polarization states. The incident light is monochromatic and linearly polarized in the horizontal direction. The field is 1 for mode 1, and $\exp(i\theta)$ for mode 2. Without mode coupling, the relative phase θ between the two modes does not affect the output polarization state of either mode. However, with mode coupling, the output field of one mode also depends on the input field of the other. For example, the vertical polarization of mode 1 has contributions from (i) the field in mode 1 converted to the vertical polarization and (ii) the field in mode 2 that is coupled to the vertically polarized mode 1. The relative phase of these two contributions can be changed by varying θ, resulting in a constructive or destructive interference which modifies the amplitude of the vertically polarized field in mode 1. This degree of freedom is effective only when there is mode mixing in the fiber. Compared to a fiber without mode coupling, more polarization states can be created at the output by adjusting the input wavefront. Mode mixing enables a polarization control utilizing spatial degrees of freedom, as illustrated schematically in Fig. 5.1(b).

5.3 Polarization manipulation

5.3.1 Depolarization-free states

To quantitatively evaluate the polarization control via spatial degrees of freedom only, we perform numerical simulation of an MMF with strong polarization and mode coupling. The fiber has N modes, each of which has a two-fold degeneracy corresponding to two orthogonal polarizations. We use the concatenated fiber model [33] to simulate random coupling among all modes of the MMF. Without loss of generality, we use the horizontal (H) and vertical (V) polarizations as the basis to describe the full transmission matrix of the MMF

$$t = \begin{bmatrix} t_{\mathrm{HH}} & t_{\mathrm{HV}} \\ t_{\mathrm{VH}} & t_{\mathrm{VV}} \end{bmatrix}$$

where t_{HH} (t_{VH}) represents the horizontal (vertical) component of the output field when the input light is horizontally polarized. t_{HH} has the dimension of $N \times N$, where N is the number of modes in the fiber for a single polarization. The output field of the horizontal polarization is $|\psi\rangle = t_{\mathrm{HH}}|\phi\rangle$ for a horizontally polarized input $|\psi\rangle$. Hence the total intensity of the horizontal polarization is $\langle\psi|\psi\rangle = \langle\phi|t_{\mathrm{HH}}^{\dagger}t_{\mathrm{HH}}|\phi\rangle$, with $t_{\mathrm{HH}}^{\dagger}$ being the Hermitian conjugate of t_{HH}. The maximum and minimum eigenvalues of $t_{\mathrm{HH}}^{\dagger}t_{\mathrm{HH}}$ set the range of transmission that can be reached in horizontal polarization. The largest eigenvalue gives the maximum energy that can be retained in the horizontal polarization after propagating through the fiber. On the contrary, the smallest eigenvalue tells the maximum energy that can be converted to the vertical polarization. After simulating an ensemble of MMFs with random mode and polarization coupling but no loss, we obtain the eigenvalue density $P(\tau_{\mathrm{HH}})$ plotted in Fig. 5.2(a). If the fiber has only one mode ($N = 1$), $P(\tau_{\mathrm{HH}})$ has a uniform distribution between 0 and 1, as a result of the complete polarization mixing in the fiber. When there are two

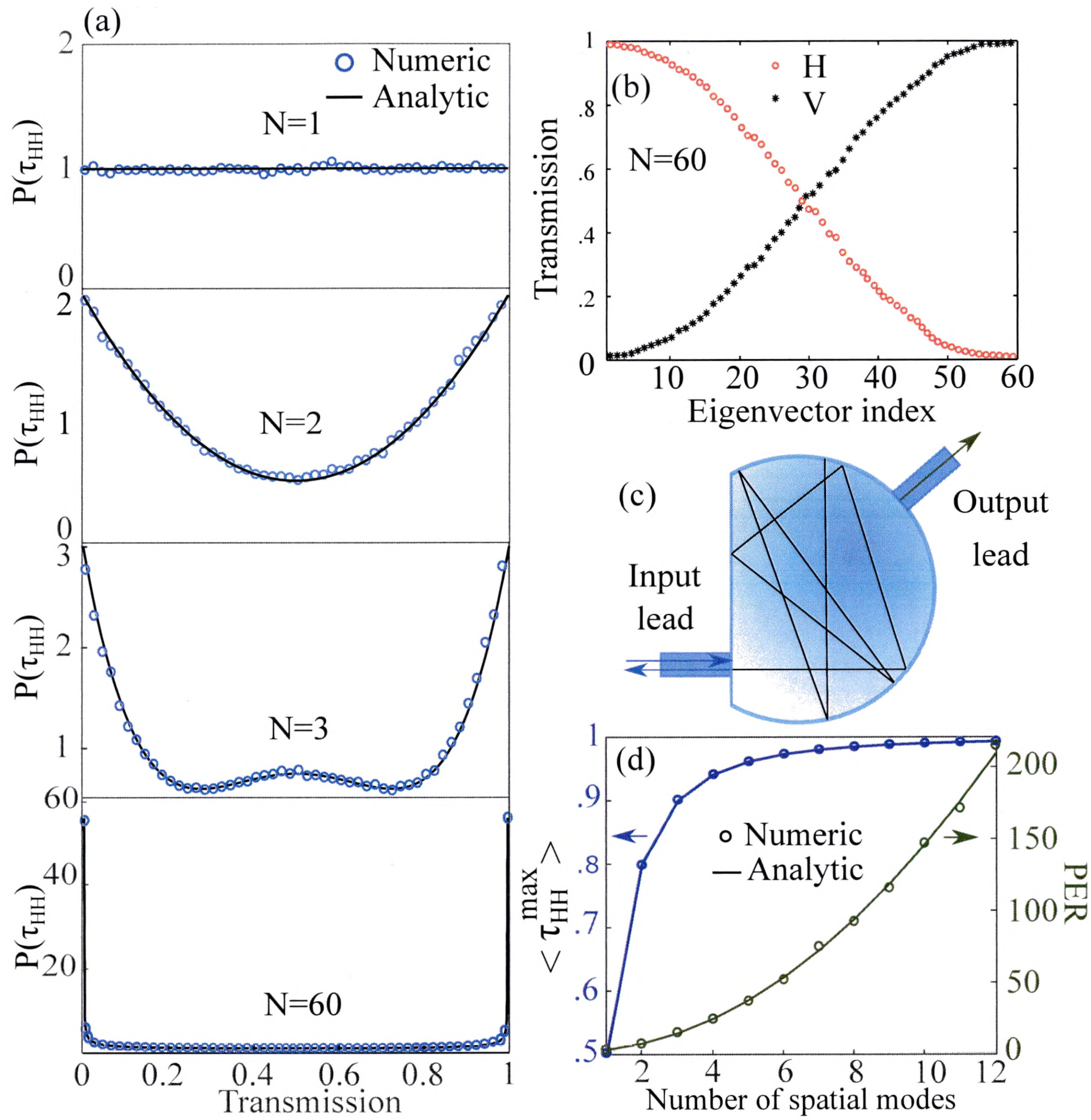

Figure 5.2: Polarization mixing in an MMF and analogy to wave scattering in a chaotic cavity. (a) Numerically calculated density of the eigenvalues of $t_{\mathrm{HH}}^{\dagger} t_{\mathrm{HH}}$ (blue circles) in an MMF with strong mode and polarization coupling. With increasing number of modes N in the fiber, $P(\tau_{\mathrm{HH}})$ evolves to bimodal distribution, in agreement to the analytical expression for the reflection eigenvalue density in a chaotic cavity with two leads (black solid lines). (b) Transmission of horizontal (H) and vertical (V) polarization components for individual eigenvectors of $t_{\mathrm{HH}}^{\dagger} t_{\mathrm{HH}}$, which are numbered by their eigenvalues from high to low. The decrease of H is accompanied by an increase of V, and their sum remains 1. (c) Schematic diagram of a chaotic cavity with two leads. Wave enters the cavity through the input lead and undergoes multiple reflections from the cavity wall before exiting via the output lead (transmission) or the input lead (reflection). (d) The maximum transmission of horizontal polarization $\langle \tau_{\mathrm{HH}}^{\max}$ approaches 1 rapidly with the increasing N. The polarization extinction ratio (PER) scales as N^2. The symbols represent numerical data and the solid lines are analytic results.

guided modes ($N = 2$), $P(\tau_{\mathrm{HH}})$ develops two peaks at $\tau_{\mathrm{HH}} = 0, 1$. With the increase of N, these two peaks grow rapidly and become dominant at $N \gg 1$. The probability of having some eigenvalue very close to unity or zero is very high. The eigenvector associated with $\tau_{\mathrm{HH}} = 1$ retains the input polarization (H) at the fiber output, while the eigenvector associated with $\tau_{\mathrm{HH}} = 0$ makes 100% conversion to the orthogonal polarization (V). As τ_{HH} decreases from 1 to 0, the percentage of transmission in the horizontal polarization drops, while that in the vertical polarization rises, as seen in Fig. 5.2(b).

The numerically calculated eigenvalue density $P(\tau_{\mathrm{HH}})$ agrees with the analytical prediction of the wave transmission in a lossless chaotic cavity [see the lines in Fig. 5.2(a)]. Such an agreement reveals the analogy between an MMF with random mode and polarization coupling and a chaotic cavity with two leads, as drawn schematically in Fig. 5.2(c). Wave enters the chaotic cavity through one lead, then reflected multiple times from the cavity wall before escaping via the same lead or the other lead. Each lead is a waveguide with N statistically equivalent channels. The four components of the scattering matrix

$$s = \begin{bmatrix} r_1 & t_2 \\ t_1 & r_2 \end{bmatrix}$$

correspond to transmissions and reflections at the two leads. When reciprocity is broken (e.g., via magnetic field), $t_1 \neq t_2^{\mathrm{T}}$, and the s matrix is a member of CUE. Both $r_{1,2}$ and $t_{1,2}$ are statistically equivalent $N \times N$ matrices. The density of transmission or reflection eigenvalues exhibits a bimodal distribution, $p(\tau) = 1/\pi\sqrt{\tau(1-\tau)}$, for large N [34]. The transmission of the input polarization in the fiber is analogous to the reflection in the chaotic cavity in the sense that light exits the cavity via the same lead. Hence, the eigenvalue τ_{HH} for the MMF corresponds to the reflection eigenvalue of the chaotic cavity.

5.3.2 Maximum Transmission Eigenvalue

Using the analytical theory developed previously for the chaotic cavity [34, 35], we derive the probability density of the maximum eigenvalue of $t_{\mathrm{HH}}^{\dagger}t_{\mathrm{HH}}$. The joint probability density for the N eigenvalues of $t_{\mathrm{HH}}^{\dagger}t_{\mathrm{HH}}$ or $t_{\mathrm{VH}}^{\dagger}t_{\mathrm{VH}}$ for the MMF, $\{\tau_1, \ldots, \tau_N\}$, is identical to the joint probability of reflection or transmission eigenvalues of a chaotic cavity, which is [34, 35]

$$p(\tau_1, \ldots, \tau_N) = c_N \prod_{n<m} (\tau_n - \tau_m)^2, \tag{5.1}$$

with $\tau_n \in (0, 1)$ for all n. Here c_N is a normalization constant such that $\int (\prod_{n=1}^{N} d\tau_n) p(\tau_1, \ldots, \tau_N) =$ 1 and $\prod_{n<m}$ is short for $\prod_{n=1}^{N} \prod_{m=n+1}^{N}$. The reduced probability when two eigenvalues are close by is a result of eigenvalue repulsion [36].

Let $\tau_{\max}$ be the largest among the N eigenvalues. The probability density of $\tau_{\max}$ follows from (5.1) as

$$p(\tau_{\max}) = N \int_0^{\tau_{\max}} d\tau_1 \cdots \int_0^{\tau_{\max}} d\tau_{N-1} p(\tau_1, \ldots, \tau_{N-1}, \tau_{\max}). \tag{5.2}$$

The integrals in (5.2) gives

$$p(\tau_{\max}) = N^2 (\tau_{\max})^{N^2-1}, \quad \tau_{\max} \in (0, 1). \tag{5.3}$$

Figure 5.3 plots the probability of having at least one eigenvalue above 0.95. The probability increases dramatically with N and reaches 1 for $N \geqslant 10$. From Eq.5.3, we get

$$\begin{aligned} \langle \tau_{\max} \rangle &= 1 - \frac{1}{N^2+1}, \\ \operatorname{var}(\tau_{\max}) &= \frac{N^2}{(N^2+1)^2(N^2+2)}. \end{aligned} \tag{5.4}$$

In the absence of loss, both $1 - \langle \tau_{\max} \rangle$ and the standard deviation of $\tau_{\max}$ scale as

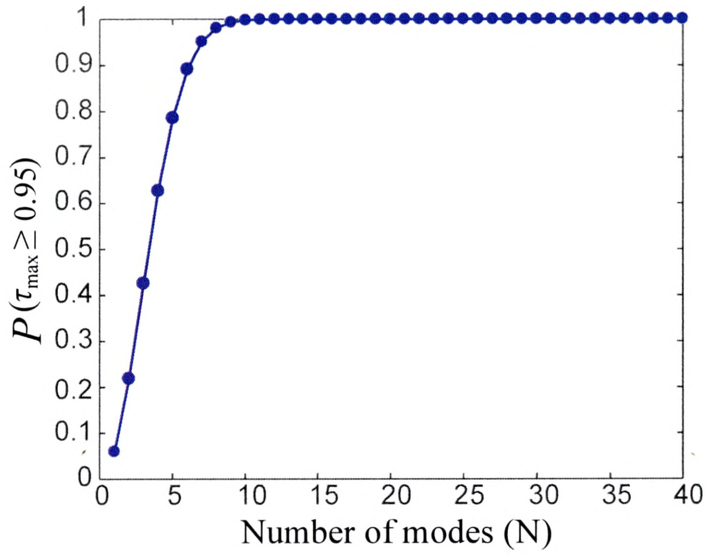

Figure 5.3: Probability of finding at least one eigenvector of $t_{\mathrm{HH}}^{\dagger} t_{\mathrm{HH}}$ with an eigenvalue (transmission in horizontal polarization) exceeding 0.95.

$1/N^2$ for large N. This is because the eigenvalues near 1 are pushed further toward 1 by the repulsion from the smaller eigenvalues and there are no eigenvalues larger than 1 to counter balance this push. We define the polarization extinction ratio (PER) as the maximal ratio of the transmissions in the two orthogonal polarizations, $\langle \tau_{\max} \rangle / (1 - \langle \tau_{\max} \rangle) = N^2$. With a large number of modes in the fiber, we obtain PER $\gg 1$. Depolarizations are avoided by coupling light into the eigenvector associated with the maximum eigenvalue of $t_{\mathrm{HH}}^{\dagger} t_{\mathrm{HH}}$. The eigenvector is a superposition of LP modes with the horizontal polarization, and can be generated by an SLM. The N^2 scaling originates from the repulsion between eigenvalues, which leads to the bimodal distribution of eigenvalues [36].

For comparison we consider the scaling of PER in an MMF without mode mixing. Due to distinctive polarization coupling for individual modes, the probability of retaining the input polarization for all output modes vanishes when the number of modes is large. The best solution to retain the input polarization is to only excite the mode with an output polarization closest to the input polarization. This reasoning can be shown mathematically. Since t_{HH} is now a diagonal matrix, the eigenvalues of $t_{\mathrm{HH}}^{\dagger}t_{\mathrm{HH}}$ are simply N independent random numbers with the n-th eigenvalue being the overlap between the output of the n-th mode and the desired polarization state. The eigenvector with the largest eigenvalue corresponds to sending light only into the mode whose output polarization has the largest overlap with the desired polarization. The joint probability density of the N eigenvalues is simply $p(\tau_1,\ldots,\tau_N)=\prod_{n=1}^{N}p(\tau_n)=1$, and the probability density of the maximal eigenvalue [as given by Eq. (S2)] is

$$p\prime(\tau_{\max}) = N\int_0^{\tau_{\max}} p(\tau_1)d\tau_1\cdots\int_0^{\tau_{\max}} p(\tau_{N-1})d\tau_{N-1}. \tag{5.5}$$

It follows that

$$p\prime(\tau_{\max}) = N(\tau_{\max})^{N-1}, \quad \tau_{\max}\in(0,1). \tag{5.6}$$

From it we have that $\langle\tau_{\max}\rangle = 1-1/(N+1)$ and $\mathrm{PER}=\langle\tau_{\max}\rangle/(1-\langle\tau_{\max}\rangle)=N$. This comparison shows that spatial mode mixing greatly enhances the ability of overcoming depolarization.

5.3.3 Effect of mode-dependent loss

The above results are obtained when the fiber has negligible loss. If the loss in the fiber is significant, the eigenvalue density will be modified, and the maximum eigenvalue will be less than 1. Consequently, the PER for the eigenvector associated with the maximum eigenvalue of $t_{\mathrm{HH}}^{\dagger}t_{\mathrm{HH}}$ will be reduced. In the MMF, the lower order modes experience less attenuation than the higher order modes. To simulate the mode-dependent loss, we assume the decay length ξ for each LP mode is proportional to its propagation constant β, $\xi=\gamma\beta$, where γ is a coefficient. By varying the value of γ, we can tune the amount of loss. We solve for the eigenvectors of $t_{\mathrm{HH}}^{\dagger}t_{\mathrm{HH}}$ with the maximum eigenvalues and compute the PER. Fig. 5.4(a) plots the PER as a function of γ. The stronger the MDL, the lower the PER. Hence, the MDL reduces the polarization control. Mode-dependent loss also reduces the polarization control when there is no mode mixing in the fiber. We repeat the calculation for the MMF without mode mixing, and obtain much lower PER for the same amount of MDL. Fig. 5.4(a) shows no matter how strong the MDL is, the PER without mode coupling is always lower than that with mode coupling. Therefore, mode coupling enhances the polarization control even when the fiber has MDL.

We adjust the amount of MDL in the numerical simulation to match that of the fiber in the experiment. Figure 5.4(b) plots the eigenvalues of numerically calculated t_{H}, which decay over a range comparable to those of the experimentally measured t_{H} (as we will discuss later in Fig. 5.11). With this amount of MDL in the numerical model, the eigenvector with the maximum eigenvalue of $t_{\mathrm{HH}}^{\dagger}t_{\mathrm{HH}}$ has a PER of 29, which is close to the experimental PER of 24. Without mode mixing, the PER is found numerically to be 6.5, much lower than the PER with mode mixing.

No matter how strong the loss is, the PER of an MMF with mode coupling is always higher than that without mode coupling. Therefore, mode coupling enhances the polarization control regardless of the loss in the fiber. Furthermore, a complete polarization control can still be achieved even when the fiber has significant loss, as described in the next subsection.

5.3.4 Polarization conversion

The efficiency of converting the input polarization (H) to the orthogonal polarization (V) is given by the minimum eigenvalue of $t_{\mathrm{HH}}^{\dagger}t_{\mathrm{HH}}$. When loss in the MMF is negligible, the minimum eigenvalue of $t_{\mathrm{HH}}^{\dagger}t_{\mathrm{HH}}$ and the maximum eigenvalue of $t_{\mathrm{VH}}^{\dagger}t_{\mathrm{VH}}$ correspond to the same eigenvector, since $t_{\mathrm{HH}}^{\dagger}t_{\mathrm{HH}}+t_{\mathrm{VH}}^{\dagger}t_{\mathrm{VH}} = 1$. When the polarizations are completely mixed, the transmitted field has no memory of its initial polarization, so the transmission matrix t_{VH} has the same statistical property as t_{HH}. The eigenvalue density $P(\tau_{\mathrm{VH}})$ is identical to $P(\tau_{\mathrm{HH}})$ and has a bimodal distribution. The ensemble-

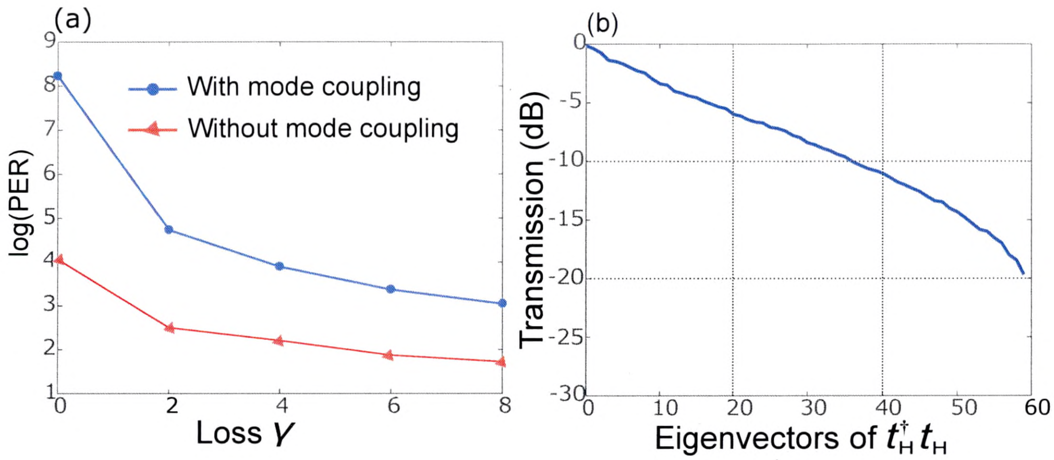

Figure 5.4: Polarization control in the presence of MDL. (a) PER for the output field of the eigenvector with the maximum eigenvalue of $t_{\mathrm{HH}}^\dagger t_{\mathrm{HH}}$ as a function of the MDL, characterized by γ, for the MMF with (blue dot) and without (red triangle) mode coupling. (b) Eigenvalues of the numerical $t_{\mathrm{H}}^\dagger t_{\mathrm{H}}$ for $\gamma = 6$, normalized by the maximum value. The range of decay is comparable to that of the fiber used in our experiment.

averaged value $\langle \tau_{\mathrm{HH}}^{\mathrm{min}} \rangle = 1 - \langle \tau_{\mathrm{VH}}^{\mathrm{max}} \rangle = 1/(N^2+1)$, and PER $= N^2$. Similar to the derivation of $p(\tau_{\mathrm{max}})$, the analytical probability density for the smallest eigenvalue is $p(\tau_{\mathrm{min}}) = N^2(1-\tau_{\mathrm{min}})^{N^2-1}$. When $N \gg 1$, light is almost completely transformed into the orthogonal polarization by spatially coupling light into the eigenvector of $t_{\mathrm{HH}}^\dagger t_{\mathrm{HH}}$ with the minimum eigenvalue.

If the fiber suffers significant loss, the maximum eigenvalue becomes less than 1, but the minimum eigenvalues remains close to 0. The eigenvector associated the minimum eigenvalues can be used for a complete polarization control, despite the reduced total transmission. For example, if the input light is horizontally polarized, by coupling it to the eigenvector of $t_{\mathrm{VH}}^\dagger t_{\mathrm{VH}}$ with eigenvalue close to 0, the transmitted light has a vanishing vertical component. Thus the depolarization is avoided, but part of incident light is lost instead of being transmitted. Also the transmitted light can be converted to the vertical polarization by exciting the eigenvector of $t_{\mathrm{HH}}^\dagger t_{\mathrm{HH}}$ with the minimum eigenvalue. So far we have considered only horizontal and vertical polarizations for input and output fields, but the same concept applies to any polarization

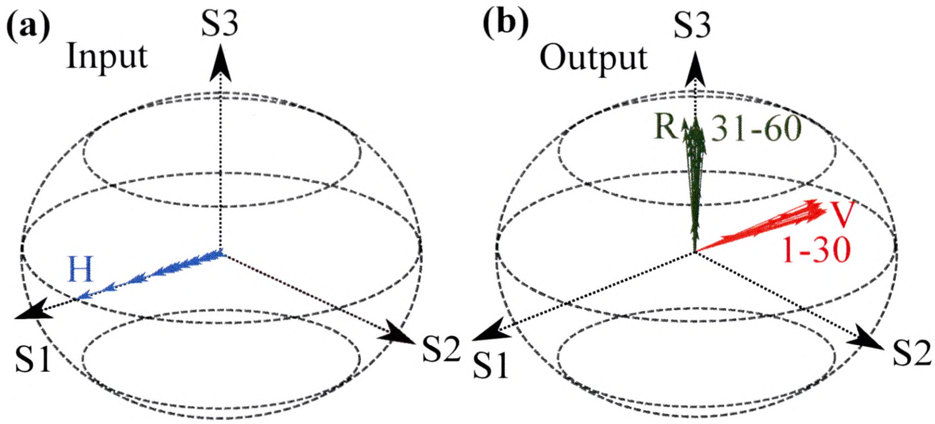

Figure 5.5: Poincaré sphere representation of multi-channel polarization transformation in the MMF. The direction of each arrow stands for the polarization of each mode and the length represents the intensity of the mode. Transformation of the (a) input horizontal polarization (H) to the (b) output polarization state with the vertical polarization (V) for modes 1-30 and the right-hand circular polarization (R) for modes 31-60.

state. As long as the fiber completely scrambles the polarization of light, all polarization states are equivalent. For example, let us consider the conversion from the horizontally polarized (H) input to the right-hand circular polarized (R) output. The corresponding transmission matrix $t_{\mathrm{RH}}^{\dagger}t_{\mathrm{RH}}$ has the same eigenvalue density as $t_{\mathrm{HH}}^{\dagger}t_{\mathrm{HH}}$. With strong mode coupling and negligible loss in the fiber, $P(\tau_{\mathrm{RH}})$ is bimodal, the peak at $\tau_{\mathrm{RH}} = 1$ ($\tau_{\mathrm{RH}} = 0$) allows a full conversion of horizontal polarization to right (left) circular polarization.

5.3.5 Multi-channel polarization transformation

Let us take one step further: instead of controlling the polarization state of the total transmission, we can have different polarization states for different modes. As an example, we transform the horizontal polarization (H) of the input field [Fig. 5.5 (a)] to a complex polarization state (A) at the output of an MMF with 60 modes. As shown in Fig. 5.5 (b), the polarization state A has the vertical polarization (V) for modes 1-30 and right-hand circular polarization (R) for modes 31-60. The conversion is achieved by coupling the incident light to the eigenvector of $t_{\mathrm{AH}}^{\dagger}t_{\mathrm{AH}}$ with the eigenvalue close to 1, when the loss in the fiber is negligible. When the loss is significant, we resort to the output polarization state B that is orthogonal to A. In this case, B has the horizontal polarization (H) for modes 1-30 and the left-hand circular polarization (L) for modes 31-60. By exciting the eigenvector of $t_{\mathrm{BH}}^{\dagger} t_{\mathrm{BH}}$ with the eigenvalue close to 0, the output polarization state is orthogonal to B and thus identical to A.

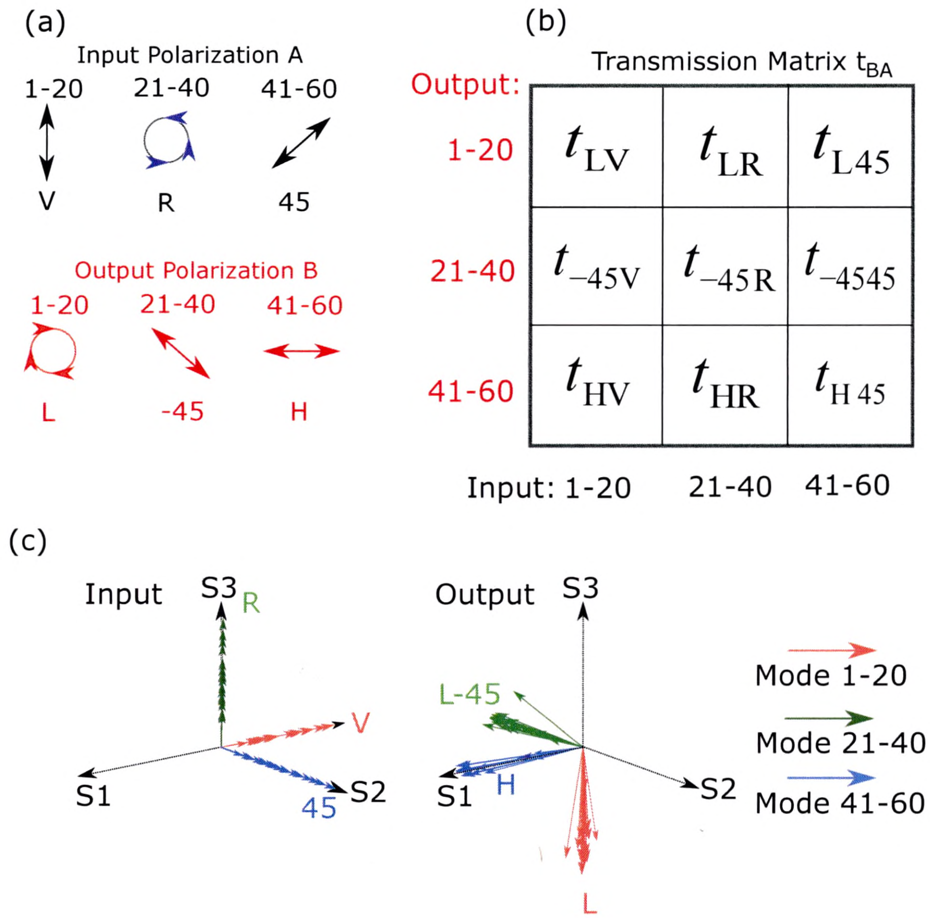

Figure 5.6: Multi-channel polarization control. (a) Input polarization state A and output polarization state B. Modes 1-20 have the linear vertical (V) polarization at the input and the left-circular (L) polarization at the output. Modes 21-40 have the right-circular (R) polarization at the input and the linear $-45°$ polarization at the output. Modes 41-60 have the linear 45° polarization at the input and the linear horizontal (H) polarization at the output. (b) Corresponding transmission matrix t_{BA} is constructed. (c) The Poincaré sphere representation of the input and output polarization states for all modes of the eigenvector of $t_{\mathrm{BA}}^{\dagger} t_{\mathrm{BA}}$ with the largest eigenvalue.

Finally, we can also handle arbitrary input polarization states, i.e. individual spatial modes may have different polarizations. Here we illustrate how to realize this with an example. First we construct the transmission matrix that relate different input and output polarization states. We calculate t_{HH}, t_{VH}, t_{HV}, t_{VV} of a fiber with 60 spatial modes using the concatenated fiber model. From them, we construct, e.g., the transmission matrix for linear vertical (V) polarization input and left-circular (L) polarization output $t_{\mathrm{LV}} = (1/\sqrt{2})(t_{\mathrm{HV}} + it_{\mathrm{VV}})$, or the transmission matrix for right-circular (R) polarization input and L polarization output $t_{\mathrm{LR}} = (1/\sqrt{2})(t_{\mathrm{LH}} - it_{\mathrm{LV}})$, as described in the main text. Next we consider individual input and output modes have different polarizations, e.g., let us bin the LP modes into three groups, i.e. 1-20, 21-40 and 41-60. As illustrated in Fig. 5.6(a), the input polarization state A has V polarization for modes 1-20, R polarization for modes 21-40 and linear 45° (45) polarization for modes 41-60. The output polarization state B is designed to be L polarization for modes 1-20, linear -45° (-45) polarization for modes 21-40 and horizontal (H) polarization for modes 41-60. To achieve the conversion from A to B, we construct the corresponding transmission matrix t_{BA} shown in Fig. 5.6(b). For example, the elements for 1-20 rows and 1-20 columns of t_{BA} are a copy of the elements in 1-20 rows and 1-20 columns of t_{LV}, the elements of 1-20 rows and 21-40 columns of t_{BA} are copied from the corresponding rows and columns of t_{LR}, etc. We then compute the eigenvalues and eigenvectors of $t_{\mathrm{BA}}^{\dagger}t_{\mathrm{AB}}$. When the fiber has no loss, the maximum eigenvalue is equal to 1. Figure 5.6(c) presents the Poincaré sphere representation of the input (left) and output (right) polarization states of the corresponding eigenvector. The arrows of three colors (red, green and blue) denote the polarization states for three groups of LP modes (1-20, 21-40 and 41-60). These results confirm that the eigenvector of $t_{\mathrm{BA}}^{\dagger}t_{\mathrm{BA}}$ with the unity eigenvalue has the input polarization state A and the output polarization state B, thus realizing the polarization conversion from A to B.

Therefore, an MMF with strong mode and polarization coupling is capable of transforming arbitrary input polarizations to arbitrary output polarizations with nearly 100% efficiency. Since only the spatial degrees of freedom are deployed at the input, the output intensity in each spatial mode, i.e., the distribution of output energy among spatial modes, cannot be controlled. To design not only polarizations but also intensities of all output modes, both spatial and polarization degrees of freedom at the input shall be utilized.

5.4 Experimental demonstration

5.4.1 Polarization-resolved transmission matrix

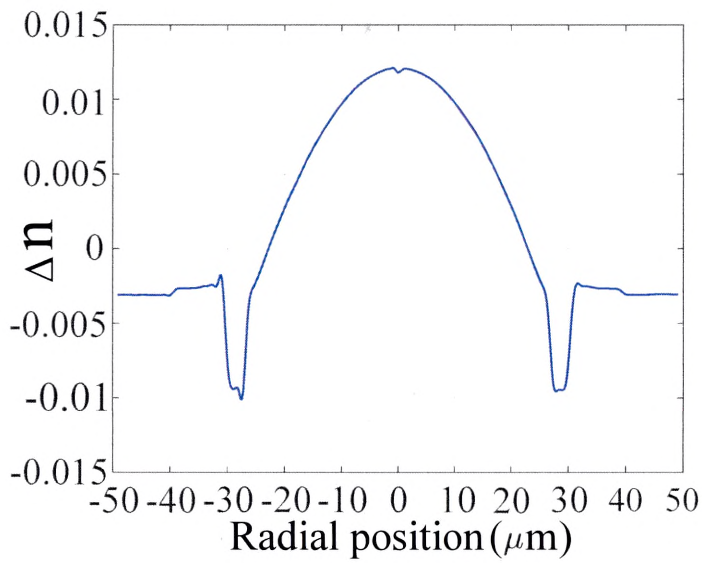

Figure 5.7: Measured refractive index profile of the multimode fiber. The difference between the refractive index in the core and that in the cladding, Δn, has a parabolic profile within the core (from -25 μm to 25 μm), and a sharp drop at the interface between the core and the cladding to reduce light leakage.

We experimentally demonstrate the complete polarization control of an MMF with strong polarization and mode coupling by wavefront shaping. We test different types of MMFs experimentally and obtained similar results. The fiber whose data are presented here has the graded refractive index profile (see Fig. 5.7) designed to reduce the mode-dependent loss, leading to the highest degree of polarization control. The core diameter of the fiber is 50 μm and the numerical aperture (NA) is approximately 0.22. The fiber is 2 m long. To enhance mode and polarization mixing in the MMF, the bare fiber is coiled to 5 loops (without a spool) and pressed by 12 clamps which are arranged in a circle. The clamps not only introduce mode and polarization coupling at multiple points in the fiber, but also stabilize the fiber.

We characterize the polarization-resolved transmission matrix with an interferometric setup shown in Fig. 5.8(a). A horizontally polarized laser beam at wavelength $\lambda = 1550$ nm is split into a fiber arm and a reference arm. The SLM in the fiber arm prepares the spatial wavefront of light before it is launched into the MMF. To measure the field transmission matrix, plane waves with different wavevectors, covering the range of the fiber numerical aperture, are projected onto the input facet of the fiber. The output facet of the fiber is directly imaged by a lens onto a camera. A linear polarizer in front of the camera filter out the polarization component of light transmitted through the fiber. By rotating the linear polarizer, we measure different polarization components of the fiber output. A half-waveplate in the reference arm rotates the polarization direction of the reference beam to match the direction of the linear polarizer. The reference beam then combines with the fiber output beam at a beam-splitter, and their interference fringes are recorded by a camera. Using the off-axis holography, we extract the amplitude and phase of the field exiting the fiber in the same polarization as the reference.

The transmission matrix is measured with input in momentum (wavevector) basis and output in real space. Then we perform a basis transform to represent the matrix in the fiber LP mode basis. By rotating the linear polarizer and the half waveplate, the transmission matrices for both horizontal and vertical polarizations are measured. After computing the eigenvalues and eigenvectors of the transmission matrix, we generate the input wavefronts of individual eigenvectors with the SLM. To modulate

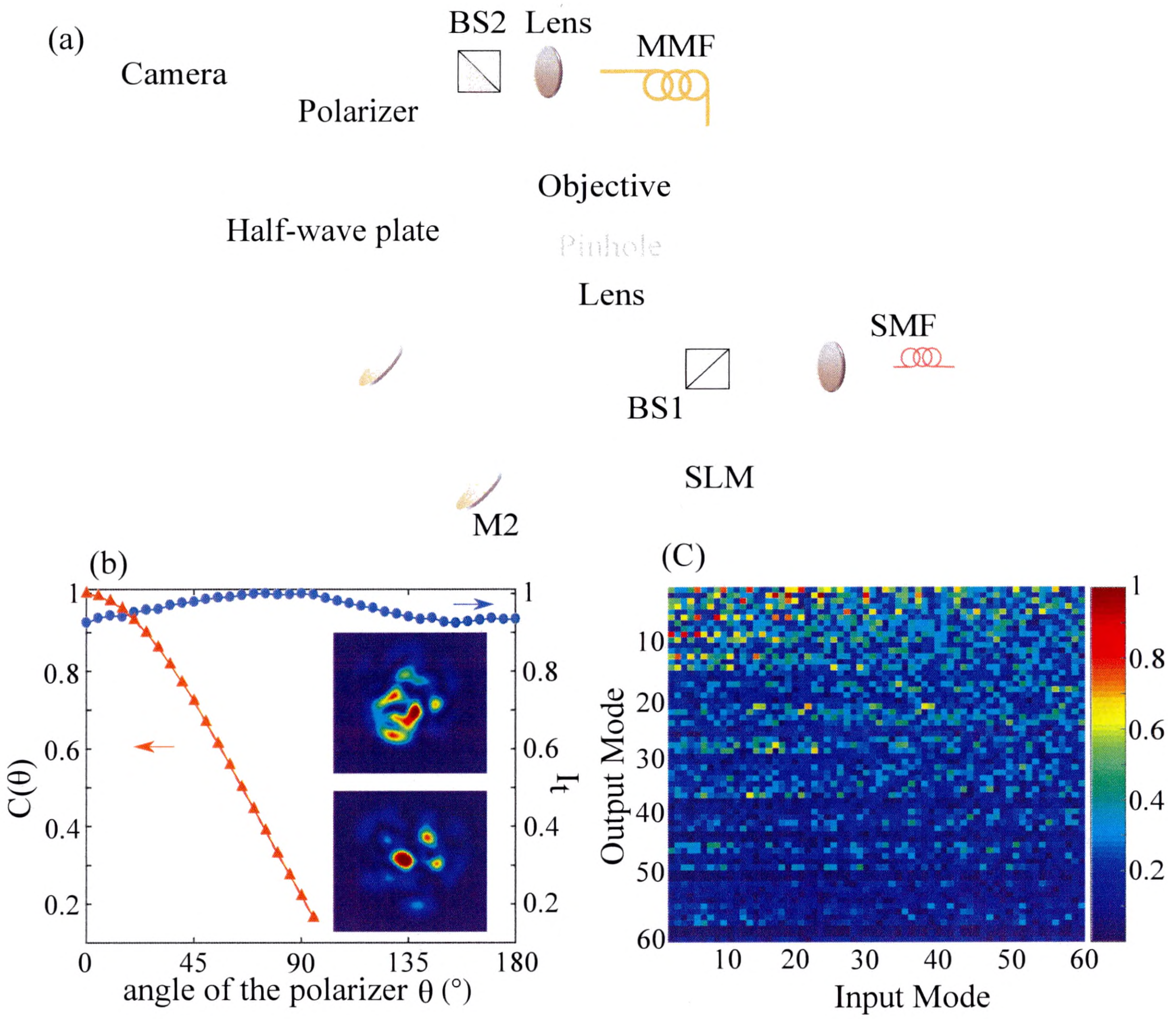

Figure 5.8: Experimental setup and fiber calibration. (a) Schematic of the interferometric setup for measuring the transmission matrix of a multimode fiber (MMF). SMF: single mode fiber. C: lens. BS: beam splitter. PBS: polarizing beam splitter. M: mirror. (b) Characterization of depolarization in the MMF. The total transmitted intensity I_t (blue circles) and the correlation of output intensity patterns $C(\theta)$ (orange triangles) confirm complete depolarization. θ is the angle of the polarizer. Insets: intensity patterns of orthogonal polarizations measured when $\theta = 0°$ and $90°$. (c) Amplitude of measured transmission matrix t_{HH} in LP mode basis reveals strong mode mixing in the fiber.

both amplitude and phase of the input field with a phase-only SLM, a computer-generated phase hologram is employed and a pinhole on the back focal plane of the lens in the fiber arm filters out the first order diffraction pattern of the SLM.

To quantify the depolarization in the MMF, we measure the total transmitted intensity I_t as a function of the angle of the polarizer θ. As shown in Fig. 5.8(b), I_t only exhibits slight ($\sim 9\%$) variations with θ. Furthermore, the output intensity pattern changes with θ and thus individual output channels have distinct polarizations. We compute the correlation function $C(\theta) = \vec{I}(0) \cdot \vec{I}(\theta)$, where $\vec{I}(\theta)$ is a unit vector representing the normalized intensity profile at θ. The decay of $C(\theta)$ in Fig. 5.8(b) illustrates the decreasing correlation of the intensity pattern with θ. The insets of Fig. 5.8(b) are the two intensity patterns of orthogonal polarizations ($\theta = 0, 90°$), which are almost uncorrelated, indicating nearly complete depolarization.

The amplitude of measured transmission matrix t_{HH} of the MMF in the LP mode basis is shown in Fig. 5.8(c). No matter which mode light is injected into, the output field spreads over all modes, although higher order modes have lower amplitudes due to stronger dissipations. The measured t_{VH} has a similar characteristic to that of t_{HH}.

5.4.2 Mode coupling in the experimental fiber

To further confirm that mode coupling occurs in the fiber, we measure the output intensity patterns with and without clamps, when a plane wave is launched into the fiber at normal incidence. As shown in Fig. 5.9, the output intensity pattern is speckled, indicating the output field consists of multiple LP modes. When the fiber is pressed by the clamps, the number of speckle grains increases and the speckle grain size decreases. Therefore, more spatial modes are excited in the fiber due to the enhanced mode mixing introduced by the clamps.

Figure 5.10 presents experimentally measured field transmission matrices, t_{HH} and t_{VH}, of the MMF for two output polarizations H and V, with the input polarization set

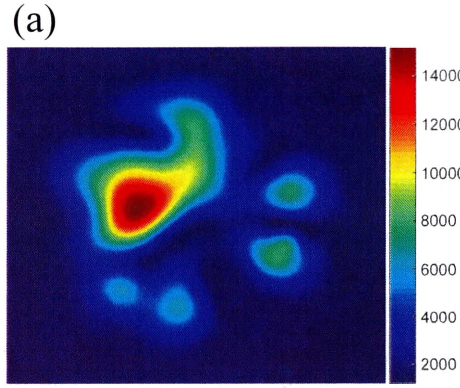

Figure 5.9: Mode mixing introduced by fiber clamps. Output intensity patterns for an MMF (a) without or (b) with clamps applying stress to it. A plane wave is launched into the fiber at normal incidence. The clamps enhance mode mixing in the fiber.

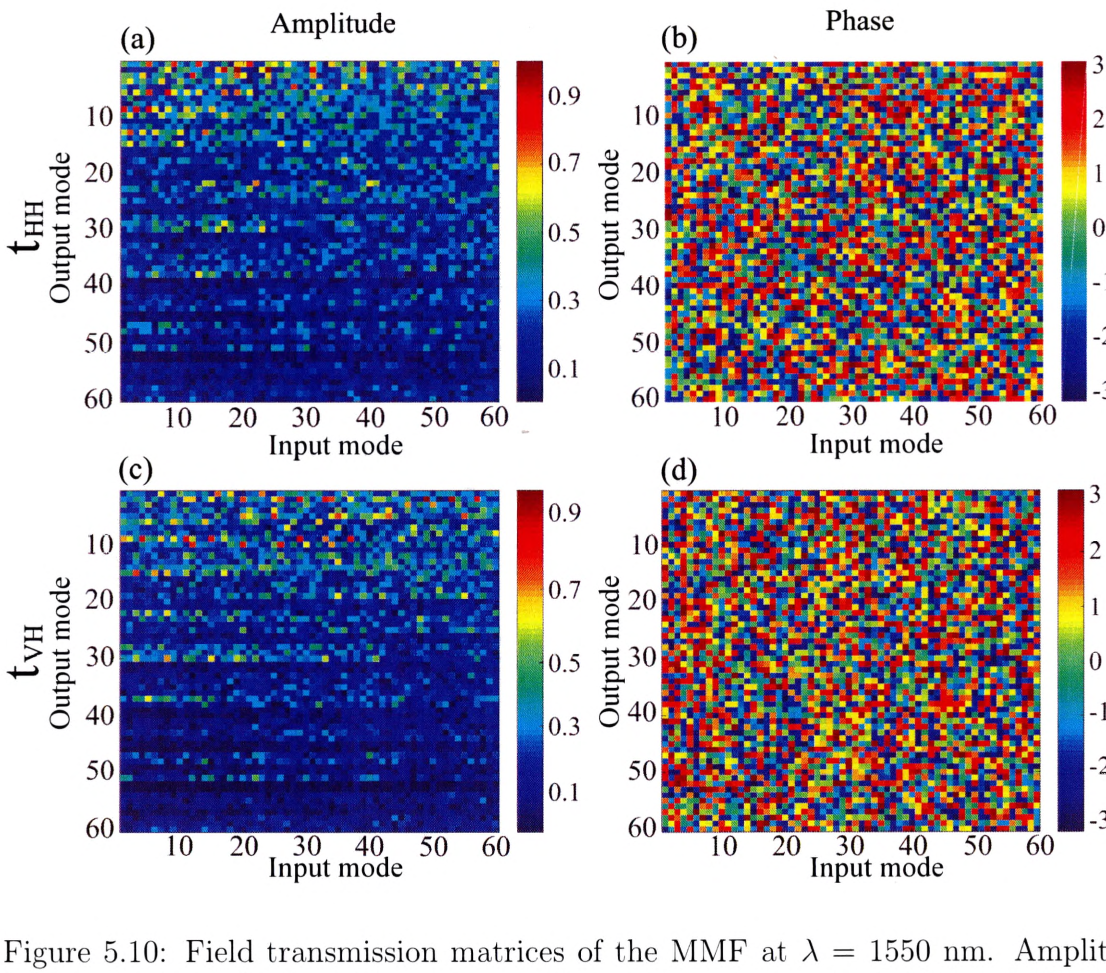

Figure 5.10: Field transmission matrices of the MMF at $\lambda = 1550$ nm. Amplitude (a,c) and phase (b,d) of the measured t_{HH} and t_{VH}. t_{HH} in (a,b) has both input and output horizontally polarized. t_{VH} in (c,d) has input horizontally polarized and output vertically polarized.

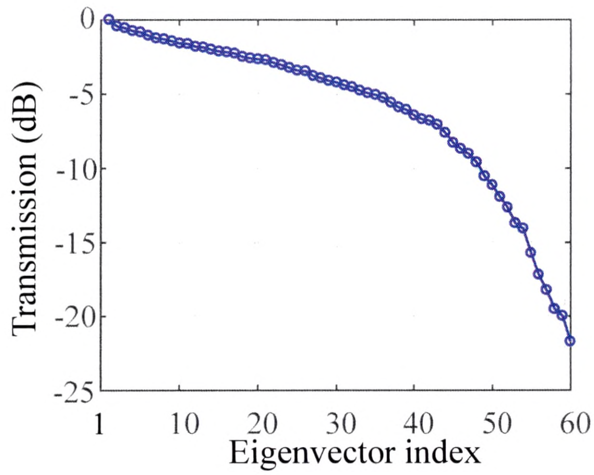

Figure 5.11: Eigenvalues of the measured matrix $t_{\mathrm{H}}^{\dagger}t_{\mathrm{H}}$ of the MMF. The eigenvalues are normalized by their maximum. The decay of τ_{HH} indicates mode-dependent loss in the fiber.

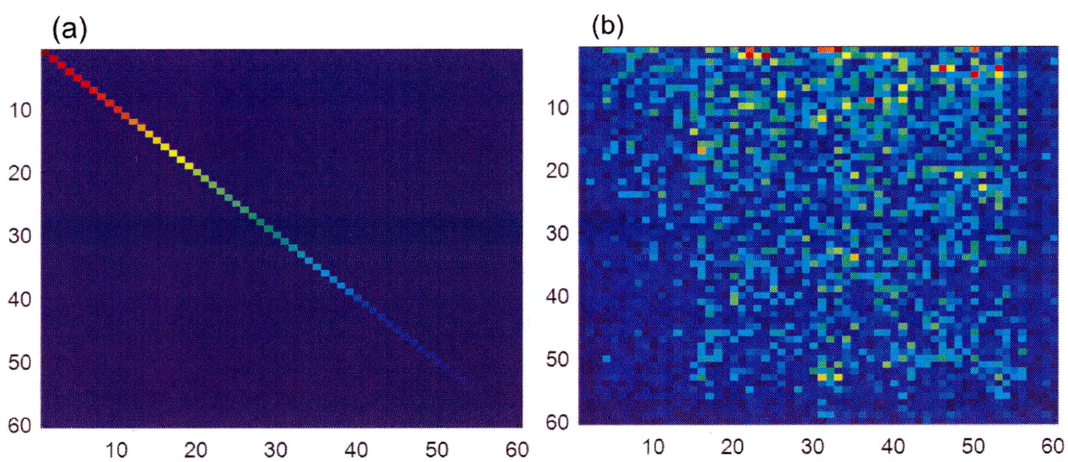

Figure 5.12: Verification of strong polarization and mode mixing in the fiber. Experimentally measured t_{HH} and t_{VH} cannot be made diagonal by a common basis transform. Singular value decomposition of $t_{\mathrm{HH}} = U\Sigma V^{\dagger}$. (a) The diagonal matrix Σ. (b) The transformed matrix $U^{\dagger}t_{\mathrm{VH}}V$ is non-diagonal. A common basis transformation cannot diagonalize t_{HH} and t_{VH} simultaneously.

to H. The eigenvalues of $t_{\mathrm{H}}^{\dagger}t_{\mathrm{H}}$, in which $t_{\mathrm{H}} = \binom{t_{\mathrm{HH}}}{t_{\mathrm{VH}}}$, reveals the mode-dependent loss in the fiber. As seen in Fig. 5.11, the sharp drop of the transmission curve after mode 50 indicates the cut-off of guided modes in the fiber. The measured transmission matrix, represented in LP mode basis, shows that with input light in a single LP mode, the fiber output spreads over all LP modes. To quantify the degree of mode coupling, we calculate the inverse participation ratio (IPR) of the LP modes constituting the fiber output field when the input light is in a single LP mode. The IPR is defined as $\mathrm{IPR} \equiv (\sum_{i=1}^{60} P_i)^2 / \sum_{i=1}^{60} P_i{}^2$, where P_i is the intensity of the i-th LP mode at the fiber output. If the output field consists of only one LP mode, the IPR is equal to 1. If the output is a random superposition of all LP modes (with statistically equal weight), the IPR is 30. In our experiment, the IPR of the output field for a single LP mode input is about 22, indicating the fiber output contains far more than one LP mode due to strong mode mixing in the fiber. The IPR is lower than 30 because the higher order modes experience more loss and have lower output intensities than the lower-order ones.

A systematic error in transforming the transmission matrix from the measurement basis to the LP mode basis might make the measured t_{HH} and t_{VH} non-diagonal matrices. If there were the case, a common basis transformation could diagonalize both t_{HH} and t_{VH}. To test this possibility, we conduct the singular value decomposition of the measured t_{HH}. The input and output singular vectors of t_{HH} diagonalize t_{HH}, but they cannot diagonalize the measured t_{VH}, as shown in Fig. 5.12. This result confirms the measured transmission matrix corresponds to that of an MMF with strong mode and polarization coupling.

5.4.3 Experimentally realized polarization control

To control the output polarization, we compute the eigenvectors of the experimentally measured $t_{\mathrm{HH}}^{\dagger}t_{\mathrm{HH}}$. For each eigenvector, the intensities of horizontal and vertical polarization components in total transmitted light, I_{H} and I_{V}, are plotted in Fig. 5.13. The first eigenvector is associated with the largest eigenvalue, thus having the maximum I_{H} and the minimum I_{V}. The eigenvectors are ordered by the value of I_{H} from high to low. The decrease of I_{H} is accompanied by the increase of I_{V}. Eventually I_{V} cannot reach the maximum of I_{H} due to mode-dependent loss in the fiber. Employing the computer-generated phase hologram for a simultaneous phase and amplitude modulation [37], we create the input wavefront for the first eigenvector with the SLM and launch it into the fiber. The output intensity patterns of horizontal and vertical polarizations are recorded (left panel in Fig. 5.13). Since higher order modes suffer more loss in the fiber , the transmitted light is mainly composed of lower order modes. The horizontal polarization component is much stronger than the vertical one, and the PER is about 24. Hence, most energy is retained in the input polarization (H), and depolarization is overcome. The experimentally obtained PER is in agreement with the numerical simulation result of a fiber with comparable amount of loss (see $\gamma = 6$ in Fig. 5.4).

A complete conversion to the orthogonal polarization (V) is achieved with the eigenvector of $t_{\mathrm{HH}}^{\dagger} t_{\mathrm{HH}}$ with a small eigenevalue. For example, we choose the 52nd eigenvector which has a low transmission of the horizontal polarization and launch its input field profile into the MMF. The measured output intensity patterns are shown in the right panel of Fig. 5.13, and the transmitted light is dominated by the vertical polarization component. The PER is 43, exceeding that of the first eigenvector. Since the 52nd eigenvector has more contributions from higher order modes, which experience a higher attenuation than lower order modes, its transmission is about half that of the first eigenvector.

We can convert the horizontally polarized light to any polarization state at the fiber output. For example, to obtain the right circular polarization (R), we construct $t_{\mathrm{RH}} = \frac{1}{\sqrt{2}}(t_{\mathrm{HH}} - i t_{\mathrm{VH}})$ from the measured t_{HH} and t_{VH}, and couple the incident light to

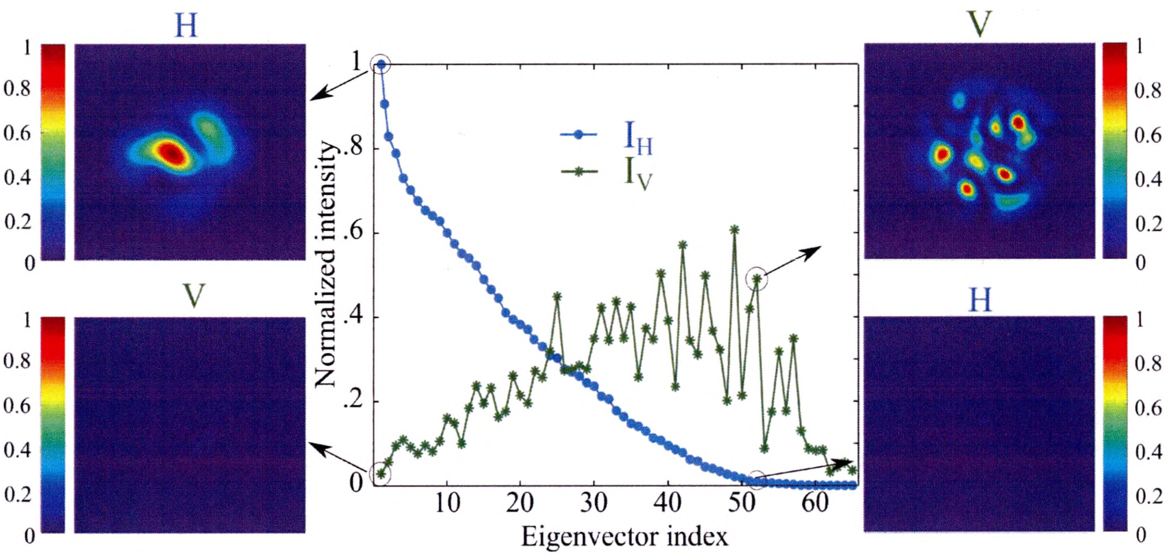

Figure 5.13: Experimental demonstrations of overcoming fiber depolarization and complete conversion to the orthogonal polarization. Central panel: intensities of the horizontal (H) and vertical (V) polarization components of total transmitted light, I_{H} and I_{V}, for individual eigenvectors of experimentally measured $t_{\mathrm{HH}}^{\dagger}t_{\mathrm{HH}}$. The eigenvectors are arranged by I_{H} from high to low, and the largest value of I_{H} is normalized to 1. The experimentally measured output intensity patterns of H and V for the 1st and the 52nd eigenvectors are shown on the left and right, respectively.

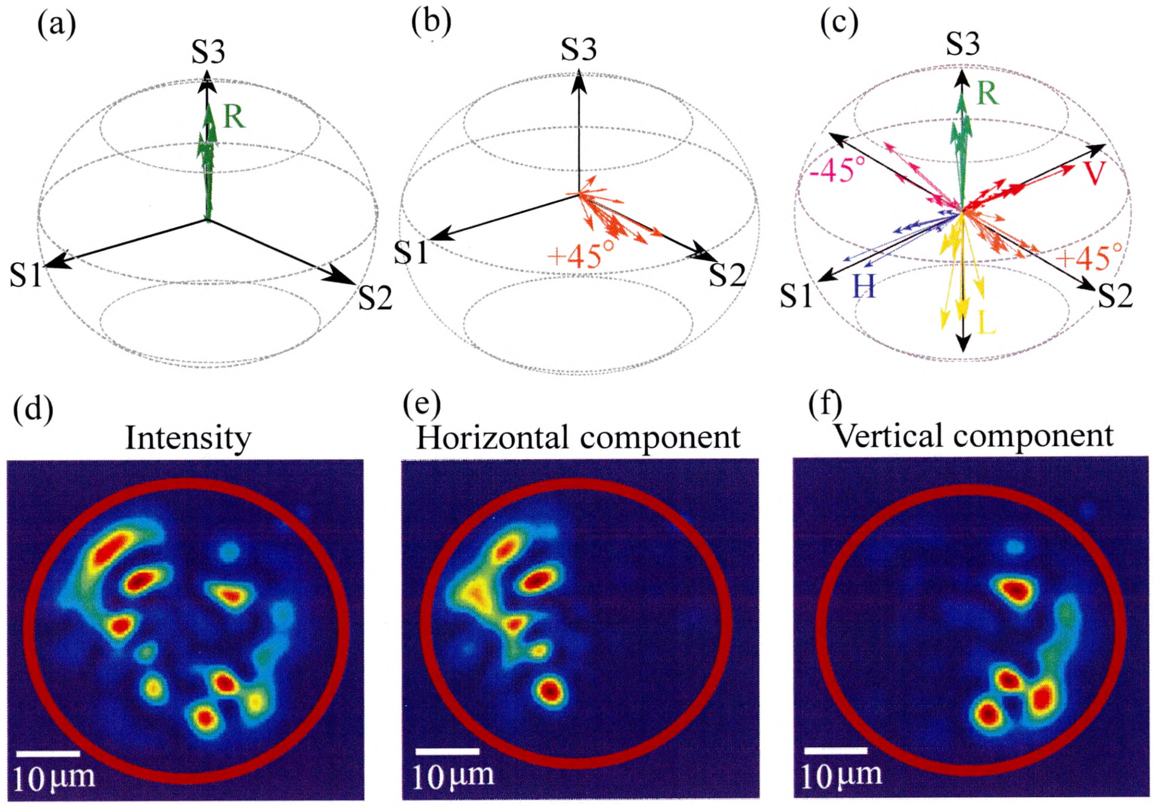

Figure 5.14: Experimental generation of arbitrary polarization states. (a-c) Poincaré sphere representation of output polarization state of (a) the highest transmission eigenchannel of t_{RH}, all LP modes (each represented by an arrow) are right circularly polarized, (b) a low transmission eigenchannel of t_{FH}, all modes are linearly polarized in the 45° direction. (c) different polarization states generated with a fixed input polarization (H). (d-f) Output intensity pattern (d), its horizontal (e) and vertical (f) polarization components reveal the transmitted field in the left half of the fiber facet is horizontally polarized, and the right half vertically polarized.

the eigenvector of $t_{\mathrm{RH}}^{\dagger}t_{\mathrm{RH}}$ with the largest eigenvalue. The output polarization states of individual LP modes are plotted on a Poincaré sphere in Fig. 5.14(a). Each arrow represents one mode, and its length stands for the intensity of that mode. All arrows point along the S_3 axis, indicating all modes are circularly polarized, despite varying intensities. In Fig. 5.14(b), we obtain the linear $+45°$ polarization by exciting a low transmission eigenchannel of $t_{-45\mathrm{H}} = \frac{1}{\sqrt{2}}(t_{\mathrm{HH}} - t_{\mathrm{VH}})$ (the eigenvector of $t_{-45\mathrm{H}}^{\dagger}t_{-45\mathrm{H}}$ with a small eigenvalue). Figure 5.14(c) shows different polarization states that are generated experimentally with a fixed input polarization (H).

To demonstrate the ultimate polarization control, we make the polarization states different for individual output channels. In addition to the fiber mode basis, the spatial channels can be represented in real space (near-field zone of the fiber distal end) or momentum space (far-field zone). In the following example, we describe the fiber output channels in real space. The output polarization state C is designed to have the horizontal polarization for the spatial channels within the left half of the fiber cross-section, and the vertical polarization in the right half. The transmission matrix t_{CH} is constructed by concatenating one half of t_{HH} and the other half of t_{VH}. The conversion of polarization from H to C is realized by exciting the highest transmission eigenchannel of t_{CH}. Figure 5.14(d) is an image of the fiber output facet taken by the camera without a polarizer. After the linear polarizer is placed in front of the camera and oriented in the horizontal direction, the right half becomes dark while the left half remains bright in Fig. 5.14(e). Once the polarizer rotates to the vertical direction, the right half lights up while the left half turns dark in Fig. 5.14(f). Hence, the transmitted field is horizontally polarized in the left half of the fiber facet, and vertically polarized in the right half. Additional example is given in Fig. 5.15, showing numerically generated polarization states using the experimentally measured transmission matrices t_{HH} and t_{VH}. The output field is the left-hand circular polarization (L) in the top half of the fiber facet and right-hand

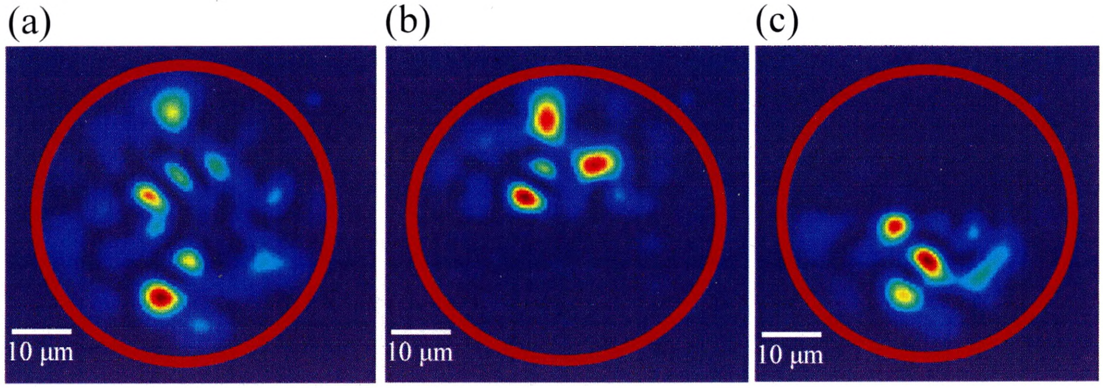

Figure 5.15: Circular polarization control. Output intensity pattern (a), its left-hand (b) and right-hand (c) circularly polarized components reveal the transmitted field in the top half of the fiber facet is the left circularly polarization, and the bottom half right circularly polarization.

circular polarization (R) in the bottom half.

5.5 Wavelength dependence

While our scheme of polarization control works for any wavelength, we must adjust the input wavefront with wavelength in order to realize a specific output polarization state. This is because the transmission matrix t_{HH} is wavelength dependent, and its spectral correlation width is determined by the properties of the fiber, such as the length, the differential group delay and the degree of mode mixing. The spectral correlation function is defined as $C(\Delta\lambda) = \langle I(\lambda_0)I(\lambda_0 + \Delta\lambda)\rangle / \langle I(\lambda_0)\rangle\langle I(\lambda_0 + \Delta\lambda)\rangle - 1$, where $I(\lambda)$ is the output intensity pattern at wavelength λ for a fixed input wavefront. We compute $C(\Delta\lambda)$ using $t_{\mathrm{HH}}(\lambda)$ for 1550 nm $\leqslant \lambda \leqslant$ 1551.3 nm in the numerical simulation of an MMF with strong mode mixing but negligible loss. The spectral width of $C(\Delta\lambda)$ is 0.2 nm in Fig. 5.16(a). We further calculate the eigenvector with the largest eigenvalue of $t^{\dagger}_{\mathrm{HH}}t_{\mathrm{HH}}$ at $\lambda_0 = 1550$ nm. The transmission of horizontal polarization for this eigenvector is unity at λ_0, as expected. As shown in Fig. 5.16(b), when the wavelength λ is detuned from λ_0 by $\Delta\lambda$, the transmission in horizontal

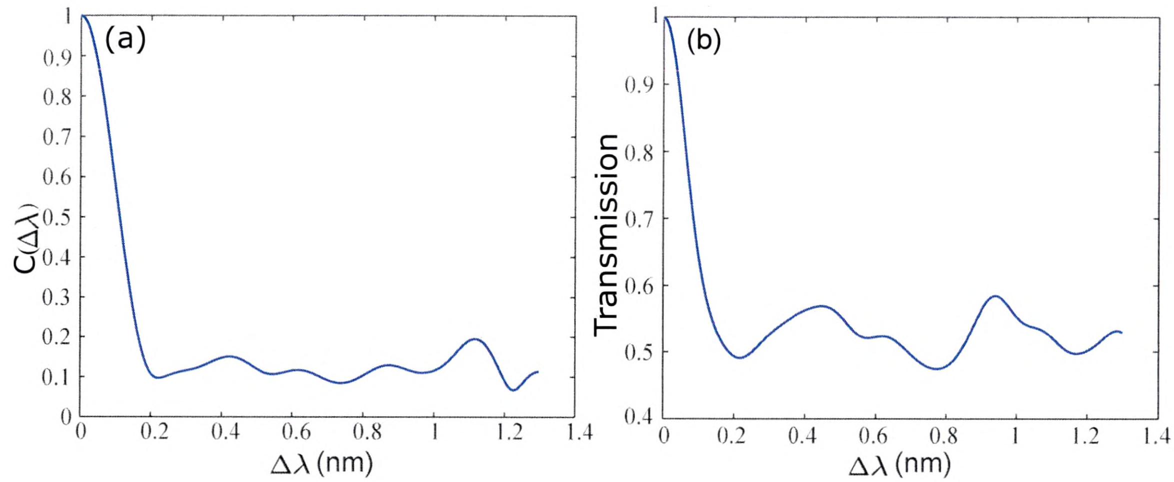

Figure 5.16: Spectral correlation function of the state with polarization control. (a) Spectral correlation function $C(\Delta\lambda)$ of an MMF with strong mode coupling and negligible loss. (b) Wavelength dependent transmission in horizontal polarization for the eigenvector with largest eigenvalue of $t_{\mathrm{HH}}(\lambda_0)$.

polarization decreases and the transmission in vertical polarization increases, eventually both approach 0.5 for $\Delta\lambda \geqslant 0.2$ nm. Thus the bandwidth of the polarization-preserving channel is equal to the spectral correlation width of the fiber. The same bandwidth is found for the polarization-changing channels. For the applications in nonlinear optics, broad-band pulses are usually used, and a large bandwidth of the polarization-shaping channels is required. This can be achieved by using MMFs with small differential group delay, which gives a large spectral correlation width.

5.6 Discussion and conclusion

Random mode mixing is long regarded as an obstacle for multimode fiber applications, and there have been intensive efforts to reduce or eliminate mode coupling. Instead of battling it, we take advantage of mode mixing for polarization control in a fiber. We demonstrate that strong coupling between spatial and polarization degrees of freedom in an MMF enable a complete control of output polarization states by manipulating only the spatial input wavefront. A general procedure of finding the spatial wavefront to create arbitrary polarization state is outlined and confirmed experimentally. It involves a measurement of the polarization-resolved transmission matrix and a selective excitation of the transmission eigenchannels corresponding to the extremal eigenvalues. With random mixing among all modes of different polarizations in the fiber, the probability of having extremal eigenvalues is enhanced by eigenvalue repulsion, analogous to a chaotic cavity. We apply the existing theory of chaotic cavities to multimode fibers, uncovering the connection between the two fields of wave chaos and fiber optics.

The global control of polarization states for MMFs is not only useful for overcoming the depolarization in an MMF, but also valuable for employing polarization-sensitive imaging techniques of fiber endoscopy and nonlinear microscopy. In this work, we demonstrate polarization control for monochromatic light, which is relevant, e.g., to fiber-based fluorescence microscopy with laser excitation. Our scheme of MMF polarization control is applicable at any wavelength, but the input wavefront for a specific output polarization state, is wavelength-dependent. The polarization shaping channels have a finite bandwidth, which corresponds to the spectral correlation width of the MMF. The nonlinear optics applications often use broad-band short pulses, and require a large spectral bandwidth for the polarization-shaping channels, which can be achieved with MMFs having small differential group delay.

Bibliography

[1] W. Xiong, C. W. Hsu, Y. Bromberg, J. E. Antonio-Lopez, R. A. Correa, & H. Cao, Complete polarization control in multimode fibers with polarization and mode coupling, Light Sci. Appl. **7**, 54 (2018).

[2] Y. Guan, O. Katz, E. Small, J. Zhou & Y. Silberberg, Polarization control of multiply scattered light through random media by wavefront shaping, Opt. Lett. **37**, 4663-4665 (2012).

[3] J. H. Park, C. Park, H. Yu , Y. H. Cho & Y. Park, Dynamic active wave plate using random nanoparticles, Opt. Express **20**, 17010-17016 (2012).

[4] S. Tripathi, R. Paxman, T. Bifano, and K. C. Toussaint, Vector transmission matrix for the polarization behavior of light propagation in highly scattering media, Opt. Express **20**, 16067-16076 (2012).

[5] S. Tripathi & K. C. Toussaint, Harnessing randomness to control the polarization of light transmitted through highly scattering media, Opt. Express **22**, 4412-4422 (2014).

[6] H. B. de Aguiar, S. Gigan & S. Brasselet, Polarization recovery through scattering media, Sci. Adv. **3**, e1600743 (2017).

[7] D. V. Kiesewetter, Polarisation characteristics of light from multimode optical fibres, Quantum Electron **40**, 519-524 (2010).

[8] A. P. Mosk, A. Lagendijk, G. Lerosey & M. Fink, Controlling waves in space and time for imaging and focusing in complex media, Nat. Photon. **6**, 283-292 (2012).

[9] S. Rotter & S. Gigan, Light fields in complex media: Mesoscopic scattering meets wave control, Rev. Mod. Phys. **89**, 015005 (2017).

[10] T. Čižmár & K. Dholakia, Shaping the light transmission through a multimode optical fibre: complex transformation analysis and applications in biophotonics, Opt. Express **19**, 18871–18884 (2011).

[11] T. Čižmár & K. Dholakia, Exploiting multimode waveguides for pure fibre-based imaging, Nat. Commun. **3**, 1027 (2012).

[12] Y. Choi, C. Yoon, M. Kim, T. D. Yang, C. Fang-Yen, R. R. Dasari, K. J. Lee and W. Choi, Scanner-free and wide-field endoscopic imaging by using a single multimode optical fiber, Phys. Rev. Lett. **109**, 203901 (2012).

[13] A. M. Caravaca-Aguirre, E. Niv, D. B. Conkey and R. Piestun, Real-time resilient focusing through a bending multimode fiber, Opt. Express **21**, 12881–12887 (2013).

[14] R. Y. Gu, R. N. Mahalati and J. M. Kahn, Design of flexible multi-mode fiber endoscope, Opt. Express **23**, 26905–26918 (2015).

[15] M. Plöschner, T. Tyc and T. Čižmár, Seeing through chaos in multimode fibres, Nat. Photon. **9**, 529–535 (2015).

[16] S. Sivankutty, V. Tsvirkun, G. Bouwmans, D. Kogan, D. Oron, E. R. Andresen and H. Rigneault, Extended field-of-view in a lensless endoscope using an aperiodic multicore fiber, Opt. Lett. **41**, 3531–3534 (2016).

[17] A. Porat, E. R. Andresen, H. Rigneault, D. Oron, S. Gigan and O. Katz, Wide-field lensless imaging through a fiber bundle via speckle correlations, Opt. Express **24**, 16835–16855 (2016).

[18] A. M. Caravaca-Aguirre & R. Piestun, Single multimode fiber endoscope, Opt. Express **25**, 1656–1665 (2017).

[19] B. Redding & H. Cao, Using a multimode fiber as a high-resolution, low-loss spectrometer, Opt. Lett. **37**, 3384–3386 (2012).

[20] B. Redding, M. Alam, M. Seifert and H. Cao, High-resolution and broadband all-fiber spectrometers, Optica **1**, 175–180 (2014).

[21] N. H. Wan, F. Meng, T. Schröder, R.-J. Shiue, E. H. Chen and D. Englund, High-resolution optical spectroscopy using multimode interference in a compact tapered fibre, Nat. Commun. **6**, 7762 (2015).

[22] S. Brasselet, Polarization-resolved nonlinear microscopy: application to structural molecular and biological imaging, Adv. Opt. Photonics **3**, 205 (2011).

[23] N. Stasio, C. Moser and D. Psaltis, Calibration-free imaging through a multicore fiber using speckle scanning microscopy, Opt. Lett. **41**, 3078–3081 (2016).

[24] L. G. Wright, D. N. Christodoulides and F. W. Wise, Controllable spatiotemporal nonlinear effects in multimode fibres, Nat. Photon. **9**, 306–310 (2015).

[25] L. G. Wright, Z. Liu, D. A. Nolan, M.-J. Li, D. N. Christodoulides and F. W. Wise, Self-organized instability in graded-index multimode fibre, Nat. Photon. **10**, 771 (2016).

[26] H. Defienne, M. Barbieri, I. A. Walmsley, B. J. Smith and S. Gigan, Two-photon quantum walk in a multimode fiber, Sci. Adv. **2**, e1501054 (2016).

[27] Y. Israel, R. Tenne, D. Oron and Y. Silberberg, Quantum correlation enhanced super-resolution localization microscopy enabled by a fibre bundle camera, Nat. Commun. **8**, 14786 (2017).

[28] D. Richardson, J. Fini and L. Nelson, Space-division multiplexing in optical fibres, Nat. Photon. **7**, 354–362 (2013).

[29] V. Doya, O. Legrand and F. Mortessagne, Optimized absorption in a chaotic double-clad fiber amplifier, Opt. Lett. **26**, 872–874 (2001).

[30] C. Michel, V. Doya, O. Legrand and F. Mortessagne, Selective amplification of scars in a chaotic optical fiber, Phys. Rev. Lett. **99**, 224101 (2007).

[31] M. Fridman, M. Nixon, M. Dubinskii, A. A. Friesem and N. Davidson, Principal modes in fiber amplifiers, Opt. Lett. **36**, 388–390 (2011).

[32] K. Okamoto, Fundamentals of optical waveguides (Academic press, 2010).

[33] K. P. Ho & J. M. Kahn, Statistics of group delays in multimode fiber with strong mode coupling, J. Lightwave Technol. **29**, 3119–3128 (2011).

[34] H. U. Baranger & P.A. Mello, Mesoscopic transport through chaotic cavities: A random s-matrix theory approach, Phys. Rev. Lett. **73**, 142 (1994).

[35] R. Jalabert, J.-L. Pichard and C. Beenakker, Universal quantum signatures of chaos in ballistic transport, EPL (Europhysics Letters) **27**, 255 (1994).

[36] C. W. Beenakker, Random-matrix theory of quantum transport, Rev. Mod. Phys. **69**, 731 (1997).

[37] V. Arrizón, U. Ruiz, R. Carrada and L. A. González, Pixelated phase computer holograms for the accurate encoding of scalar complex fields, J. Opt. Soc. Am. A **24**, 3500–3507 (2007).

Chapter 6

Single-shot full-field measurement of optical pulses with a multimode fiber

6.1 Introduction

In the previous chapters, we discussed that the abundant spatial degrees of freedom can be utilized for controlling linear [1–4] and nonlinear light propagation [5–9] in an MMF. The spatial, temporal, spectral or polarization states of transmitted light are manipulated by shaping the spatial wavefront of an incident beam. An MMF can function as a microscope [10–13], a reconfigurable waveplate [14] or a pulse shaper [1–4]. In particular, the coupling between spatial and temporal degrees of freedom in an MMF enables tailoring the output state in time by manipulating the input state in space. However, the reverse process, i.e., extracting the input temporal shape from the output spatial profile of an MMF, has not been explored. It will open the possibility of using an MMF for temporal pulse measurement.

MMFs have already been employed for various sensing applications. For example, the MMF is implemented to detect changes in temperature, refractive index and strain [15–18], because the speckle pattern, produced by the interference of guided modes, is sensitive to external perturbations. For optical coherence tomography (OCT), random temporal speckles generated by MMFs are used to image axial reflectivity profiles [19]. Furthermore, the dependence of the output spatial pattern on the input spectrum is utilized to transform an MMF into a compact and high-resolution spectrometer [20, 21]. However, only the spectral amplitude is encrypted in the spatial intensity pattern, not the spectral phase, which is needed for full-field temporal measurement.

[1]In this chapter, we propose and realize a novel method based on an MMF for single-shot full-field measurement of optical pulses. It utilizes the complex yet deterministic spatiotemporal speckle field produced by a reference pulse $f(t)$ propagating through an MMF. Such field $E(\mathbf{r}, t)$, which is two-dimensional (2D) in space $\mathbf{r}$ and one-dimensional (1D) in time t, interferes with the unknown field $g(t)$ of a signal pulse that is phase coherent with $f(t)$. The interference pattern is integrated in time by a camera. From this pattern, both spectral amplitude and phase of the signal are retrieved. The Fourier transform gives the full field of $g(t)$. The temporal resolution δt is set by the temporal speckle size, which is inversely proportional to the spectral bandwidth of the reference pulse $\delta\omega$. The temporal range of single-shot measurement Δt is set by the temporal length of the transmitted waveform, which is given by the inverse of the spectral correlation width $\Delta\omega$ of the MMF. A fiber with stronger modal dispersion has faster spectral decorrelation, thus covering a longer time window.

Our scheme can be considered as parallel ghost imaging in time [23]. Compared to the conventional ghost imaging that relies on the sequential generation of different temporal waveforms [24–26], the MMF simultaneously creates many distinct temporal

1. This chapter is primarily based on the work in ref [22]. W. Xiong performed the experiment and developed the algorithm with help from S. Gertler and H. Yilmaz. H. Cao supervised the project.

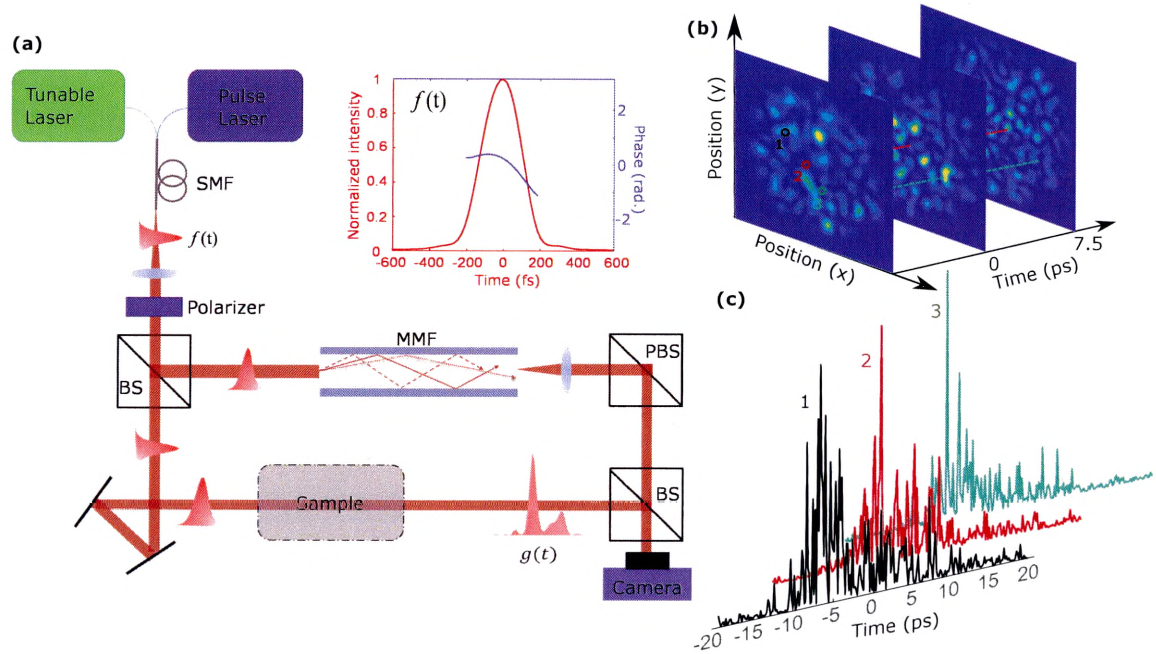

Figure 6.1: Experimental setup and measured spatio-temporal speckles. (a) Schematic of a Mach-Zehnder interferometric setup for full-field measurement. A CW laser with tunable frequency (Agilent 81940A) for MMF calibration and a pulsed laser (NKT, Onefive Origami) for temporal measurement are sequentially coupled to a single-mode fiber (SMF). The output is collimated by a lens, and one polarization is selected by a linear polarizer. The beam is split by a beam splitter into the fiber arm and the reference arm with equal path length. Light fields from the two arms recombine by a second beam splitter, and their interference pattern is recorded by a camera (Xenics Xeva 1.7-640). Inset: intensity (red) and phase (blue) of the reference pulse launched into the MMF. BS: beam splitter. PBS: polarizing beam splitter. (b) Spatial field (amplitude) distribution of the laser pulse transmitted through the MMF at three arrival times -7.5, 0 and 7.5 ps. (c) Temporal field amplitudes at three spatial positions of the fiber output facet, marked by matching colors in (b).

speckle patterns, each at a different spatial location of the output facet, to sample the signal. The parallel sampling enables single-shot measurement, eliminating the requirement for repetitive signals.

6.2 Measurement scheme

The proposed scheme is experimentally demonstrated in a Mach-Zehnder interferometric setup shown schematically in Fig. 6.1(a). A 230 fs pulse from a mode-locked near-IR fiber laser is split by a beam splitter into two, one is launched into the MMF for creation of spatio-temporal speckle field $E(\mathbf{r}, t)$, the other is sent to probe a sample placed in the other arm of the interferometer. The transmitted or reflected field $g(t)$ from the sample is combined with $E(\mathbf{r}, t)$ by a second beam splitter. Since they are phase-coherent, they will interfere, as long as $g(t)$ overlaps with $E(\mathbf{r}, t)$ in time, which is ensured by matching the optical path lengths of the two arms of the interferometer. To increase the temporal length of $E(\mathbf{r}, t)$, which determines the measurement range, we adjust the launch condition for the reference pulse into the MMF so that it excites many guided modes that propagate at a different speed. Due to modal dispersion, the transmitted pulse is broadened and distorted. The pulse shape varies spatially across the fiber facet. To have strong modal dispersion, we choose a step-index fiber (105 μm core, 0.22 NA, Thorlabs FG105LCA) of 1.8-meter length.

To calibrate the spatiotemporal speckle at the fiber output, we measure the transmitted field profile in the spectral domain with a tunable continuous-wave (CW) fiber laser. The laser wavelength λ is scanned from 1520 nm to 1570 nm with a step of 0.2 nm. This range fully covers the spectrum of the reference pulse. To ensure the launch condition of the CW laser light into the MMF is identical to that of the pulsed laser, the outputs from both lasers are coupled to a single-mode fiber (SMF) switch. The CW light transmitted through the MMF is combined with that from the reference arm at a slight angle, producing spatial interference fringes. By applying a Hilbert filter in the Fourier domain of the recorded interference pattern, the amplitude and phase of the transmitted field at a single frequency ω are extracted. Scanning the frequency ω of the CW laser and repeating the off-axis holography measurement gives the frequency-resolved field transmission matrix $T(\mathbf{r}, \omega)$. At both the input and the output of the MMF, only one polarization is selected.

After calibrating $T(\mathbf{r}, \omega)$ of the MMF with the tunable CW laser, the input source is switched to a pulsed laser (NKT Onefive Origami). When the diode current is

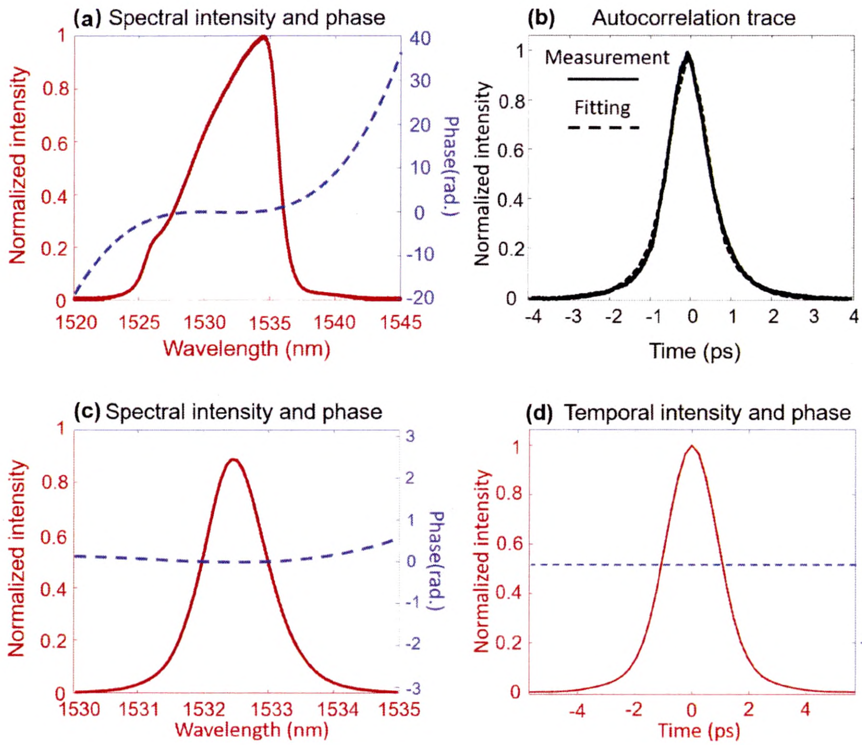

Figure 6.2: Calibration of the femtosecond reference pulse. (a) Red solid line is the measured spectral intensity of the laser pulse from NKT Onefive Origami, and the blue dashed line is the spectral phase obtained from fitting the measured temporal autocorrelation trace of the pulse in (b). (b) Measured temporal autocorrelation trace of the pulse (black solid line) and simulated trace (black dashed line) from the measured spectral intensity and fitted spectral phase in (a).

set to 750 mA, the emission spectrum is centered at wavelength $\lambda = 1546$ nm and has a full width at half maximum (FWHM) of 12 nm. The spectrum of the pulse is measured by an optical spectrum analyzer (OSA, YOKOGAWA AQ6370D), and plotted in Fig. 6.2(a). To obtain the temporal pulse shape, we measure the temporal autocorrelation trace of the pulse with an autocorrelator (Femtochrome FR-103XL), see Fig. 6.2(b). We fit the spectral phase of the pulse (blue dashed line in Fig. 6.2(a) so that the corresponding autocorrelation trace (black dashed line in Fig. 6.2(b) matches well with the measured one. The FWHM of the pulse is 230 fs, as shown in the inset of Fig. 6.1.

From these measurements, the spectral amplitude and phase of the reference field

$f(\omega)$ are obtained. The Fourier transform $\mathcal{F}$ gives the temporal waveform $f(t) = \mathcal{F}[f(\omega)]$ of the reference pulse that is injected to the MMF. The temporal shape and phase of the reference pulse are shown in the inset of Fig. 6.1(a). The transmitted field of the MMF is $E(\mathbf{r}, \omega) = T(\mathbf{r}, \omega)f(\omega)$ in frequency, and $E(\mathbf{r}, t) = \mathcal{F}[E(\mathbf{r}, \omega)]$ in time. As shown in Fig. 6.1(b), the output speckle pattern changes rapidly in time. At each spatial location, the distinct temporal waveform is composed of multiple speckles, as plotted in Fig. 6.1(c).

The complex yet deterministic spatiotemporal speckles generated by the MMF enable single-shot full-field measurement of the unknown signal by interfering $E(\mathbf{r}, t)$ and $g(t)$. The time-integrated interference pattern is recored by the off-axis holography, $I(\mathbf{r}) = \int |E(\mathbf{r}, t) + g(t)|^2 dt$. The information of $g(t)$ is encoded in the interference term $\tilde{I}(\mathbf{r}) = \int dt[E(\mathbf{r}, t)g^*(t) + E(\mathbf{r}, t)^* g(t)]$. $\tilde{I}(\mathbf{r})$ is extracted with the same Hilbert filter used in the calibration of $T(\mathbf{r}, \omega)$. In the frequency domain, the interference term is $\tilde{I}(\mathbf{r}) = \int [T(\mathbf{r}, \omega)f(\omega)g^*(\omega) + T^*(\mathbf{r}, \omega)f^*(\omega)g(\omega)]d\omega$, where $g(\omega)$ is the Fourier transform of $g(t)$. This expression can be rewritten as a linear product of a matrix and a vector:

$$\tilde{I}(\mathbf{r}) = \begin{bmatrix} T(\mathbf{r}, \omega)f(\omega) & T^*(\mathbf{r}, \omega)f^*(\omega) \end{bmatrix} \begin{bmatrix} g^*(\omega) \\ g(\omega) \end{bmatrix}. \tag{6.1}$$

With $T(\mathbf{r}, \omega)$ and $f(\omega)$ known, $g(\omega)$ is retrieved from $\tilde{I}(\mathbf{r})$ by iterative optimization algorithms. To account for temporal or spectral sparsity of g, we deploy a compressive sensing algorithm FASTA [27] to solve the sparse least square optimization problem.

To find the temporal resolution, we compute the temporal correlation function of spatiotemporal speckle field, $C(\Delta t) \equiv \langle E^*(\mathbf{r}, t)E(\mathbf{r}, t + \Delta t)\rangle$, where $\langle ... \rangle$ denotes averaging over $\mathbf{r}$ and t. The FWHM of $C(\Delta t)$ gives the average temporal speckle size $\delta t = 230$ fs, which determines the temporal resolution. The temporal range of measurement Δt is equal to the temporal length of $E(\mathbf{r}, t)$, which is inversely proportional to the width of the spectral correlation function $C(\Delta\omega) \equiv \langle E^*(\mathbf{r}, \omega)E(\mathbf{r}, \omega + \Delta\omega)\rangle$.

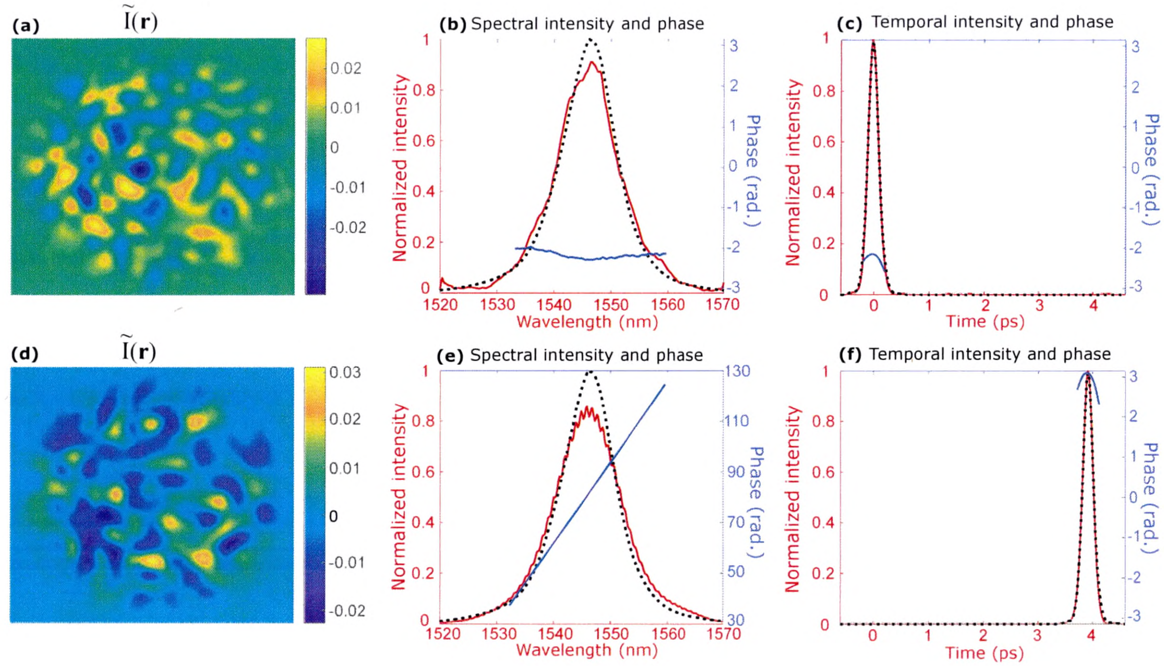

Figure 6.3: Full-field measurement of single pulses with varying delay. (a,d) 2D interference term $\tilde{I}(\mathbf{r})$ extracted from the off-axis hologram for a single pulse with arrival time $\tau = 0$ and 4 ps. (b,e) Spectral intensity (red solid line, left axis) and spectral phase (blue solid line, right axis) of the signal retrieved from (a,d). Black dashed line is the spectral intensity of the signal measured by an optical spectrum analyzer. (c,f) Temporal intensity (red solid line, left axis) and temporal phase (blue solid line, right axis) of the signal, obtained by Fourier transform of (b,e). Black dashed line is the temporal intensity of the signal obtained from autocorrelation and spectrum measurements.

From the width of $C(\Delta\omega)$, we estimate Δt to be about 35 ps. The time bandwidth product (TBP), defined by the ratio of the temporal range to the temporal resolution, is $\Delta t/\delta t = 152$.

6.3 Single pulse with varying delay times

We first test our method by measuring single pulses propagating through the reference arm (without sample) of the Mach-Zehnder interferometer with different delay times. By changing the length of the reference arm with a delay line, we vary the arrival time τ of the pulse. The zero delay time $\tau = 0$ is set by the arrival time of the pulse when the length of the reference arm is matched to that of the fiber arm. Figure 6.3 shows the measurement results for two delay times $\tau = 0$ (top row) and $\tau = 4$ ps (bottom row). The left column shows the interference term $\tilde{I}(\mathbf{r})$ extracted from the experimentally measured hologram in these two cases. Although the pulse shape remains the same, the spatial interference pattern is very different. This is because the pulse with varying delay interferes with a different part of the spatiotemporal speckles from the MMF. The retrieved intensity and phase of the pulses in wavelength and time domains are plotted in the second and third columns. The recovered spectral intensity is consistent with the measurement of the optical spectral analyzer. While the recovered spectral phase is flat for $\tau = 0$, it changes linearly for $\tau = 4$ ps. These results are expected, as the slope of the spectral phase corresponds to the delay time. In the time domain, the arrival times of the recovered pulses agree with the values set by the delay line, and the temporal pulse shape is consistent with the autocorrelation trace.

6.4 Multiple pulses

We next measure double pulses. Unstable double-pulsing is a common phenomenon for lasers that are over-pumped, but it is difficult to detect with repetitive measurement techniques that rely on stable pulse trains. Our method can measure double pulses in a single shot. To produce double pulses, we first create 2.2 ps long pulses by spectral filtering the output from a mode-locked fiber laser (Calmar Mendocino). By spectral filtering of the laser output, we obtain longer pulses. We use a fiber-based tunable filter and first set the center wavelength to 1532 nm and the FWHM to 10 nm. The measured spectrum of the filtered pulse is plotted in Fig. 6.4(a), and the autocorrelation trace is shown in Fig. 6.4(b). Again we fit the spectral phase of the filtered pulse (blue dashed line in Fig. 6.4(a)) so that the autocorrelation traces

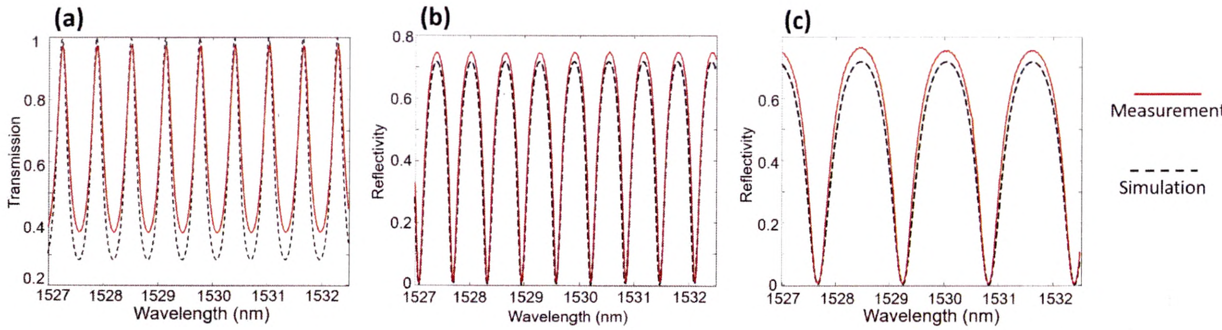

Figure 6.4: Calibration of the picosecond reference pulse. (a) Red solid line is the measured spectral intensity of the laser pulse after being spectrally filtered to 10 nm FWHM at 1532 nm, blue dashed line is the spectral phase obtained from fitting the temporal autocorrelation trace in (b). (b) Measured temporal autocorrelation trace (black solid line) and simulated trace (black dashed line) from the measured spectral intensity and fitted spectral phase in (a). (c) Measured spectral intensity (red solid line) of the filtered pulse with the FWHM reduced to 1 nm. The spectral phase (blue dashed line), obtained from (b), is nearly flat. (d) Temporal intensity (red solid line) and phase (blue dashed line) of the filtered pulse used as the reference.

agree well. Then we further reduce the FWHM of the spectral filter to 1 nm. The corresponding spectrum measured by the OSA is shown in Fig. 6.4(c). The spectral phase within this narrow range is nearly constant so that the filtered pulse is almost transform-limited and has a length of 2.2 ps.

Then we insert a double-side-polished silicon wafer to the reference arm of the March-Zehnder interferometer as the sample. An incident pulse is bounced back and forth between the two surfaces of the wafer, creating multiple pulses in transmission. The distance between the pulses is determined by the wafer thickness. The thicknesses of the silicon wafers are approximately 500 μm and 200 μm. To find the precise thickness of the sample and the incident angle of the probe light, we measure the transmission spectrum of the silicon wafer with the experimental setup shown in Fig. 6.1. The wafer is placed in the reference arm and the fiber arm is blocked. By scanning the frequency of a CW laser, we measure the spatially integrated intensity of transmitted light with the camera. Then we simulate the transmission spectrum of a silicon wafer with the transfer matrix method. By matching the simulated spectrum

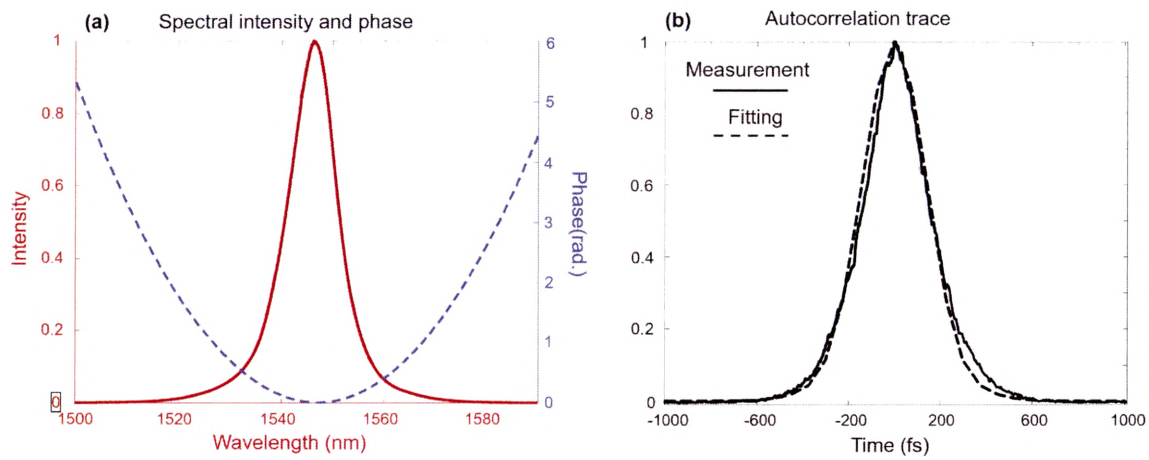

Figure 6.5: Transmission and reflection spectra of two silicon wafers. Red solid lines: experimental data. Black dashed lines: numerical results from transfer matrix simulation. (a) The transmission spectrum of the 535 μm silicon wafer with an incident angle of 1 degree. (b) The reflection spectrum of the 535 μm wafer with an incident angle of 3 degrees. (c) The reflection spectrum of the 212 μm wafer with an incident angle of 2 degrees.

(black dashed line in Fig. 6.5(a)) to the measured one (red solid line), we find that the wafer thickness is 535 μm and the incident angle is 1°.

We first measure the pulse transmitted through the 535 μm wafer. Figure 6.7(a) shows the recovered spectral intensity, which exhibits a rapid oscillation. The simulated spectrum, plotted by the black dotted line, agrees well with the recovered spectrum (red solid line). The recovered spectral phase, unwrapped and plotted by the blue dashed line, features descending jumps at the frequencies of local minima for the spectral intensity. These phase jumps, together with the amplitude oscillations, are results of spectral interference of double pulses, which are reconstructed from the Fourier transform of the recovered spectral field in Fig. 6.7(b). The first pulse originates from direct transmission of the probe pulse through the wafer and the second pulse from two bounces within the wafer. They are spaced by 12.5 ps, which is consistent with the 3.75 mm one-round-trip optical path length. Because of the relatively low reflectivity of the silicon-air interface, the intensity ratio of the first pulse to the second pulse is 17.6. Although the second pulse is rather weak, it can still be recovered by our scheme, and the temporal shape agrees well with the simulation result. The temporal phases of the two pulses vary linearly, reflecting the absence of frequency chirp within each pulse.

Finally, we measure more complex pulses that are created by reflection from a silicon wafer. The interferometric setup is slightly modified to measure the pulses reflected by the sample in the reference arm as shown in Fig. 6.6. The reference arm is divided into two by a beam splitter (BS), one is the reflection from a mirror (M3), the other from the sample. When calibrating the field transmission matrix of the multimode fiber, a beam blocker is placed in front of the sample, and the reflection from the mirror M3 serves as the reference for off-axis holography. To measure the reflection from the sample, the beam blocker is placed in front of the mirror M3. We use the tunable CW laser to measure the reflection spectrum of the silicon wafers, as plotted by red solid lines in Fig. 6.5(b)-(c). By matching them to the transfer matrix simulation results (black dashed line), the two wafers are 535 μm and 212 μm thick, and the angles of incidence are 3° and 2°, respectively.

The pulse reflected from the 535 μm wafer is recovered in Fig. 6.7(c). The recovered spectral intensity features interference fringes of higher contrast, and the spectral phase exhibits larger jumps than those in Fig. 6.7(a). The Fourier transform of the recovered spectral field reveals three pulses in the time domain, as plotted in Figure 6.7(e). The first pulse results from the direct reflection of the incident pulse by the front surface of the wafer, and the second pulse from direct reflection by the back surface. The intensity ratio of the second pulse to the first pulse in reflection is higher than that in transmission, leading to more pronounced interference fringes in the spectral domain. Nevertheless, the frequency spacing of the fringes, which is determined by the time delay between the two pulses, remains the same. Even the third pulse, generated by three reflections in the wafer, is still visible and recovered in our measurement. The recovered spectral and temporal intensities are in good

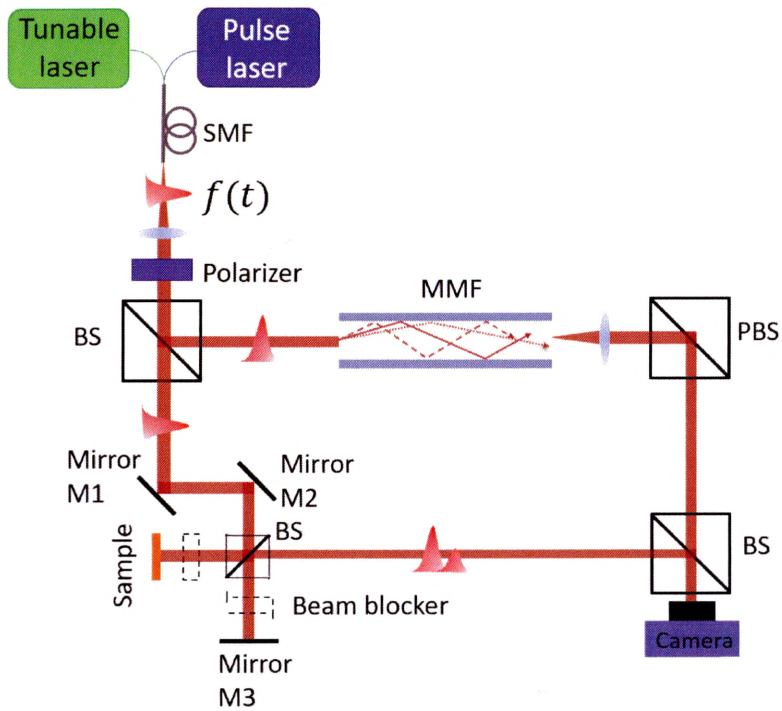

Figure 6.6: Experimental setup for measuring the reflected pulses from the sample. The reference arm of the March-Zehnder interferometer is slightly modified from the one shown in Fig. 2(a) in the main text. The reference arm is divided into two by a beam splitter (BS). The beam blocker blocks the reflection from the sample during the calibration of the fiber transmission matrix, and it blocks the reflection from the mirror M3 in the measurement of reflection from the sample. The positions of the mirror M3 and the sample are adjusted to match the optical path-length to that of the fiber arm.

agreement with the simulation results. The temporal phase within each of the three pulses increases linearly in time with the same slope, indicating each pulse has the same frequency and no chirp.

To reduce the pulse spacing, we switch to the 212 μm wafer. The reconstructed pulses in reflection are shown in Fig. 6.7(f). The delay time between adjacent pulses is reduced to 5 ps, corresponding to one round-trip in the silicon wafer. However, the relative intensities of the three pulses are not changed, as they are determined by the reflectivity of the silicon-air interface. The shorter delay time corresponds to the larger spacing of spectral fringes, leading to a smaller number of fringes within the same frequency range in Fig. 6.7(e). The recovered pulses have a slight overlap

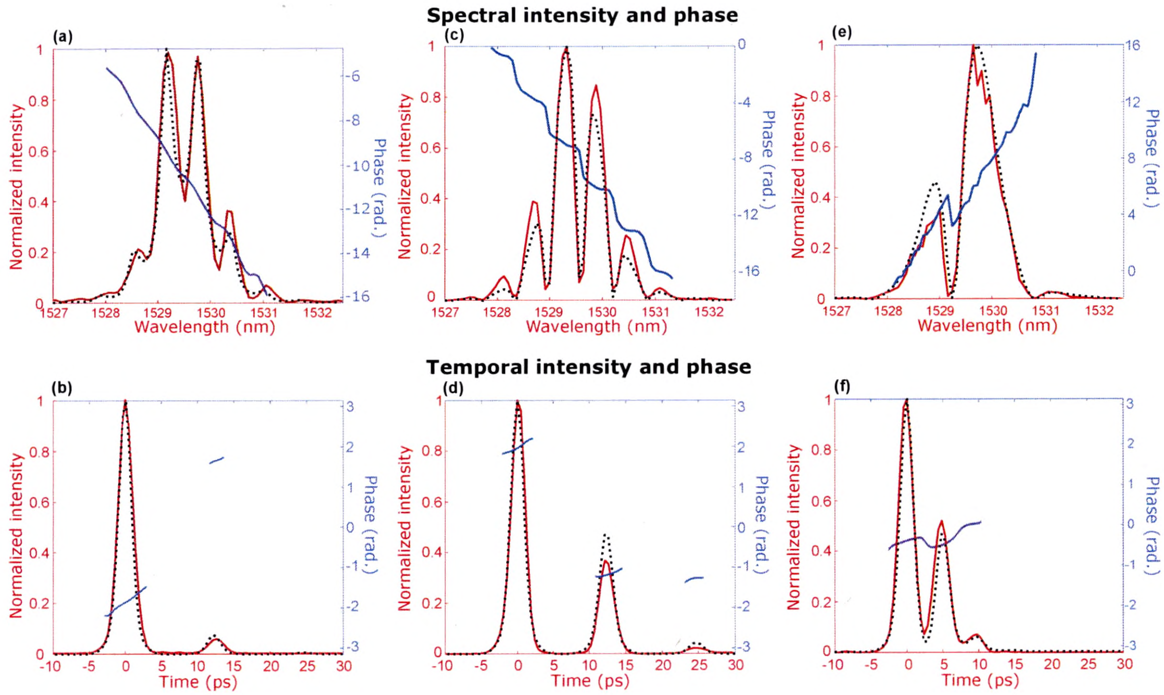

Figure 6.7: Full-field measurement of multiple pulses. First row: spectral intensity (left axis) and spectral phase (right axis). Second row: temporal intensity (left axis) and temporal phase (right axis). (a,b) Transmission of the reference pulse through a silicon wafer of thickness 535 μm with an incident angle of 1°. (b,e) Reflection of the reference pulse from the 535 μm-thick silicon wafer at the incident angle of 3°. (c,f) Reflection of the reference pulse from a 212 μm-thick silicon wafer at an incident angle of 2°.

in time, again in good agreement with the simulation result.

6.5 Discussion and summary

In summary, we demonstrate a novel MMF-based scheme for the single-shot full-field measurement of complex pulses. We obtain a temporal resolution of 230 fs, a temporal range of ~35 ps and a TBP (see the definition in Sec. 6.2) of 152. The temporal resolution can be further enhanced by increasing the spectral bandwidth of the reference pulse. The temporal range of the single-shot measurement, which is governed by the spectral correlation width of the MMF, may be tuned independently of the temporal resolution. Using a 100 meter long MMF will increase the temporal range to nanosecond [21]. The TBP is limited by the number of guided modes in the MMF, which may well exceed 1000 for large fiber core and high numerical aperture. Using a bundle of MMFs will further increase the TBP [28].

Taking full advantage of the complex spatio-temporal speckles created by the reference pulse through an MMF, our scheme eliminates the mechanical scanning of the time delay between the signal and the reference. Furthermore, our method overcomes the limitation of spectral resolution in the spectral interferometry [29–33]. Comparing to other single-shot methods based on nonlinear processes such as time lens [34–38], our scheme is based on linear interferometry, which possesses a much higher sensitivity. With the knowledge of the reference pulse, as required by all linear interferometric methods [39], it can measure non-reproducible and non-periodic, ultra-weak signals. Even without knowledge of the reference pulse, the relative phase and amplitude change imposed by the sample can still be recovered. The simplicity and high sensitivity of our method illustrate the potential of MMFs as versatile and multi-functional sensors.

Bibliography

[1] J. Carpenter, B. J. Eggleton and J. Schröder, Observation of EisenbudWigner-Smith states as principal modes in multimode fibre, Nat. Photon. **9**, 751 (2015).

[2] W. Xiong, P. Ambichl, Y. Bromberg, B. Redding, S. Rotter and H. Cao, Spatiotemporal control of light transmission through a multimode fiber with strong mode coupling, Phys. Rev. Lett. **117**, 053901 (2016).

[3] W. Xiong, P. Ambichl, Y. Bromberg, B. Redding, S. Rotter and H. Cao, Principal modes in multimode fibers: exploring the crossover from weak to strong mode coupling, Opt. Express **25**, 2709-2724 (2017).

[4] P. Ambichl, W. Xiong, Y. Bromberg, B. Redding, H. Cao and S. Rotter, Super- and Anti-Principal-Modes in Multimode Waveguides, Phys. Rev. X **7**, 041053 (2017).

[5] L. G. Wright, D. N. Christodoulides and F. W. Wise, Controllable spatiotemporal nonlinear effects in multimode fibres, Nat. Photon. **9**, 306 (2015).

[6] O. Tzang, A. M. Caravaca-Aguirre, K. Wagner and R. Piestun, Adaptive wavefront shaping for controlling nonlinear multimode interactions in optical fibres, Nat. Photon. **12**, 368374 (2018).

[7] I. S. Chekhovskoy, A. M. Rubenchik, O. V. Shtyrina, M. A. Sorokina, S. Wabnitz and M. P. Fedoruk, Nonlinear discrete wavefront shaping for spatiotemporal pulse compression with multicore fibers, JOSA B **35**, 2169-2175 (2018).

[8] R. Florentin, V. Kermene, J. Benoist, A. Desfarges-Berthelemot, D. Pagnoux, A. Barthlmy and J. P. Huignard, Shaping the light amplified in a multimode fiber, Light Sci. Appl. **6**, e16208 (2017).

[9] K. Krupa, V. Couderc, A. Tonello, D. Modotto, A. Barthlmy, G. Millot and S. Wabnitz, Refractive index profile tailoring of multimode optical fibers for the spatial and spectral shaping of parametric sidebands, JOSA B **36**, 1117-1126 (2019).

[10] I. N. Papadopoulos, S. Farahi, C. Moser and D. Psaltis, Focusing and scanning light through a multimode optical fiber using digital phase conjugation, Opt. Express **20**, 10583-10590 (2012).

[11] A. M. Caravaca-Aguirre, E. Niv, D. B. Conkey and R. Piestun, Real-time resilient focusing through a bending multimode fiber, Opt. Express **21**, 12881-12887 (2013).

[12] M. Plöschner, T. Tyc and T. Čižmár, Seeing through chaos in multimode fibres, Nat. Photon. **9**, 529 (2015).

[13] R. French, S. Gigan and O. L. Muskens, Snapshot fiber spectral imaging using speckle correlations and compressive sensing, Opt. Express **26**, 32302-32316 (2018).

[14] W. Xiong, C. W. Hsu, Y. Bromberg, J. .E. Antonio-Lopez, R. A. Correa and H. Cao, Complete polarization control in multimode fibers with polarization and mode coupling, Light Sci. Appl. **7**, 54 (2018).

[15] T. Okamoto and I. Yamaguchi, Multimode fiber-optic Mach-Zehnder interferometer and its use in temperature measurement, Appl. Opt. **27**, 3085-3087 (1988).

[16] Q. Wang and G. Farrell, All-fiber multimode-interference-based refractometer sensor: proposal and design, Opt. Lett. **31**, 317-319 (2006).

[17] Y. Liu and L. Wei, Low-cost high-sensitivity strain and temperature sensing using graded-index multimode fibers, Appl. Opt. **46**, 2516-2519 (2007).

[18] E. Fujiwara, Y. T. Wu and C. K. Suzuki, Vibration-based specklegram fiber sensor for measurement of properties of liquids, Optics and Lasers in Engineering **50**, 1726-1730 (2012).

[19] M. Villiger, P. C. Hui, N. Uribe-Patarroyo and B. E. Bouma, Imaging reflectivity profiles with random axial encoding, Photonics Conference, IEEE 299-300 (2017).

[20] B. Redding and H. Cao, Using a multimode fiber as a high-resolution, low-loss spectrometer, Opt. Lett **37**, 3384-3386 (2012).

[21] B. Redding, M. Alam, M. Seifert and H. Cao, High-resolution and broadband all-fiber spectrometers, Optica **1**, 175-180 (2014).

[22] W. Xiong, S. Gertler, H. Yilmaz and H. Cao, Multimode fiber based single-shot full-field measurement of optical pulses, arXiv preprint:1907.09057 (2019).

[23] F. Devaux, P. A. Moreau, S. Denis and E. Lantz, Computational temporal ghost imaging, Optica **3**, 698-701 (2016).

[24] T. Shirai, T. Setälä, A. T. Friberg, Temporal ghost imaging with classical non-stationary pulsed light, JOSA B **27**, 2549-2555 (2010).

[25] Z. Chen, H. Li, Y. Li, J. Shi and G. Zeng, Temporal ghost imaging with a chaotic laser, Opt. Eng. **52**, 076103 (2013).

[26] P. Ryczkowski, M. Barbier, A. T. Friberg, J. M. Dudley and G. Genty, Ghost imaging in the time domain, Nat. Photon. **10**, 167 (2016).

[27] T. Goldstein, C. Studer and R. Baraniuk, A field guide to forward-backward splitting with a FASTA implementation, arXiv:1411.3406 (2014).

[28] S. F. Liew, B. Redding, M. A. Choma, H. D. Tagare and H. Cao, Broadband multimode fiber spectrometer, Opt. Lett. **41**, 2029-2032 (2016).

[29] C. Froehly, A. Lacourt and J. C. Vienot, Notions de réponse impulsionnelle et de fonction de transfert temporelles des pupilles optiques, J. d'optique **4**, 183-196 (1973).

[30] L. Lepetit, G. Chériaux and M. Joffre, Linear techniques of phase measurement by femtosecond spectral interferometry for applications in spectroscopy, JOSA B **12**, 2467-2474 (1995).

[31] C. Dorrer, Influence of the calibration of the detector on spectral interferometry, JOSA B **16**, 1160-1168 (1999).

[32] C. Dorrer, N. Belabas, J. p. Likforman and M. Joffre, Spectral resolution and sampling issues in Fourier-transform spectral interferometry, JOSA B **17**, 1795-1802 (2000).

[33] P. R. Griffiths and J. A. De Haseth, Fourier transform infrared spectrometry (John Wiley & Sons 2007), Vol. 171.

[34] C. Iaconis and I. A. Walmsley, Spectral phase interferometry for direct electric-field reconstruction of ultrashort optical pulses, Opt. Lett. **23**, 792-794 (1998).

[35] P. Oshea, M. Kimmel, X. Gu and R. Trebino, Highly simplified device for ultrashort-pulse measurement, Opt. Lett. **26**, 932-934 (2001).

[36] B. Li, S. W. Huang, Y. Li, C. W. Wong and K. K. Wong, Panoramic-reconstruction temporal imaging for seamless measurements of slowly-evolved femtosecond pulse dynamics, Nat. Commun. **8**, 61 (2017).

[37] P. Ryczkowski, M. Nrhi, C. Billet, J. M. Merolla, G. Genty and J. M. Dudley, Real-time full-field characterization of transient dissipative soliton dynamics in a mode-locked laser, Nat. Photon. **12**, 221 (2018).

[38] A. Tikan, S. Bielawski, C. Szwaj, S. Randoux and P. Suret, Single-shot measurement of phase and amplitude by using a heterodyne time-lens system and ultrafast digital time-holography, Nat. Photon. **12**, 228 (2018).

[39] A. Monmayrant, S. Weber and B. Chatel, A newcomer's guide to ultrashort pulse shaping and characterization, J. Phys. B **43**, 103001 (2010).

Chapter 7

Deep learning pulse shapes with a multimode fiber

7.1 Introduction

In chapter 6, we have shown that with a reference pulse, an MMF can measure the spectral phase of an ultrafast optical pulse. It is required that the reference pulse is mutually coherent with the unknown signal to measure, limiting the stand-alone characterization of ultrafast pulses. Here, in this chapter, we demonstrate a self-referenced method of characterizing ultrafast pulse with an MMF [1]. Our method can measure the spectral phase of an optical pulse without a reference pulse. Moreover, this technique allows for single-shot pulse measurement in a simple experimental setup. In addition to demonstrating a novel pulse characterization scheme, the work in this chapter further illustrates the potential of complex photonic structures such as multimode fibers as a versatile optical sensing platform.

A wide variety of techniques have been proposed to characterize ultrafast pulses.

1. This chapter is primarily based on the work published in ref. [1]. W. Xiong performed the experiment and developed the algorithm with help from B. Redding, S. Gertler, Y. Bromberg and H. Tagare. H. Cao supervised the project.

Autocorrelation was first used to estimate the pulse width [2], but it introduced significant ambiguities because an auto-correlation (AC) trace is always symmetric in time. Other methods such as FROG [3], SPIDER [4], MIIPS [5] and PICASSO [6] rely on a nonlinear optical process to introduce interference between different spectral components of a pulse. These methods introduce trade-offs between the experimental complexity of the measurement, the complexity of the phase recovery algorithms, the required optical power level and the ability to characterize pulses in a single-shot.

Our approach relies on the wavelength-dependent speckle patterns formed at the end of an MMF due to multimodal interference. After calibrating the speckle field at the end of the fiber as a function of wavelength, we use the speckle pattern formed by an unknown optical pulse as a fingerprint to identify both the spectral amplitude and phase of the unknown pulse. Recovering the spectral amplitude has been demonstrated in multimode-fiber-based spectrometers [7, 8] (also see chapter 1). In chapter 6, we have shown that the spectral phase can be retrieved from the interference pattern of the unknown pulse with the spatiotemporal speckle generated by the propagation of the reference pulse through the MMF. Recovering the spectral phase without any reference is more challenging since any linear, time-stationary device is phase insensitive [9]. This is easy to understand because measuring the relative phase of different spectral components of an optical pulse requires those components to interfere. Distinct wavelengths do not interfere on a linear detector, and thus the spectral phase information is lost. Here we deployed a silicon camera to perform nonlinear measurement of an optical pulse at a wavelength of $\sim$ 1550 nm. The photon energy at 1550 nm is below the bandgap of silicon, so the silicon camera only records a signal due to two-photon absorption, providing the required nonlinear measurement. Silicon cameras were used to record the sonogram generated by femtosecond laser pulses [10]. In the scheme proposed in this chapter, a silicon camera is used to record a nonlinear speckle pattern generated by two-photon absorption of the speckle field.

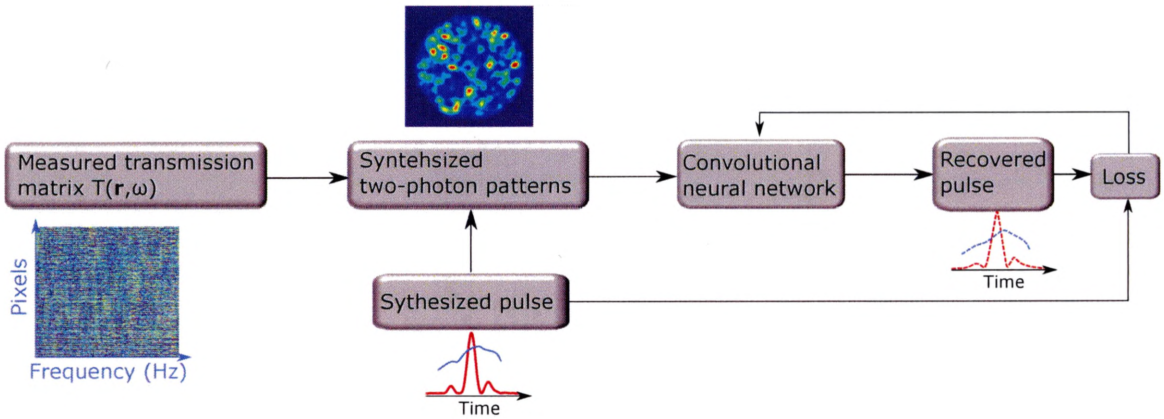

Figure 7.1: Flowchart representing the scheme of characterizing ultrafast pulses with an MMF.

7.2 Scheme of measurement

The proposed scheme of characterizing ultrafast pulses is shown by the flowchart in Fig. 7.1. To use the speckle pattern as the fingerprint of pulses, we first need to calibrate the spectral to spatial mapping properties of the MMF. This requires measuring both the amplitude and the phase of the speckle pattern at the end of the fiber as a function of the input frequency. The measured amplitude and phase at multiple frequencies are stored in a field transmission matrix $T(\mathbf{r}, \omega)$. It relates the input spectral amplitude and phase to the complex speckle field at the output of the fiber

$$E_{\text{out}}(\mathbf{r}, \omega) = E_{\text{in}}(\omega) \cdot T(\mathbf{r}, \omega).$$

Here $E_{\text{in}}(\omega)$ is the input spectral amplitude and phase and $E_{\text{out}}(\mathbf{r}, \omega)$ is the speckle field formed at the end of the fiber. With the field transmission matrix, we are able to predict the output speckle field for any input pulses with their known amplitude and phase in the frequency domain.

Recovering the pulse shape from the two-photon speckle is a non-convex inverse problem. In this scheme, we employed a deep neural network to retrieve the pulse shape. More specifically, we train a convolutional neural network (CNN) to learn the inverse mapping of the two-photon pattern and the spectral phase. Deep neural networks were demonstrated to outperform other phase retrieval algorithms in ultra-fast pulse characterizations [11], especially in the presence of noise. In the training procedure, we generate a set of pulses $E_{\text{in}}(\omega)$ and calculate the corresponding two-photon pattern $I_{2-\text{ph}}(\mathbf{r}) = \int |\int E_{\text{in}}(\omega)T(\mathbf{r},\omega)e^{-i\omega t}d\omega|^4 dt$. The two-photon pattern is the input to the neural network and the recovered pulse is compared to the known input pulse. The loss is backpropagated to the CNN to update the weights.

After the training, an experimentally measured two-photon pattern generated by a femtosecond laser on a silicon camera is sent to the well-trained neural network and the pulse shape is predicted.

7.2.1 Fiber calibration

A schematic representation of our pulse characterization setup is shown in Fig. 7.2. We deploy a Mach-Zehnder interferometric setup to calibrate the field transmission matrix of a 1.5-meter-long MMF with 105 μm diameter core and 0.22 NA (Thorlabs FG105LCA). The speckle pattern at the distal end of the fiber interferes with the plane wave in the reference arm at a slight angle, forming an off-axis hologram. We extract the amplitude and phase of the speckle pattern from the hologram recorded by the IR camera (Xenics Xeva 1.7-640). The input frequency of the tunable laser (Agilent 81940A) is swept from 1520 nm to 1580 nm at a step of 0.2 nm. After calibration, the reference arm is blocked by a shutter and an ultrafast pulsed laser is coupled to the same single-mode fiber, ensuring the same input spatial profile. The speckle pattern formed at the end of the fiber was imaged simultaneously onto the IR camera and the silicon camera (Andor Newton DU940N-UV). The IR camera records the linear speckle pattern which is used to recover the spectral amplitude $A(\omega)$ while the silicon camera records the nonlinear two-photon speckle pattern which is used to recover the spectral phase $\theta(\omega)$.

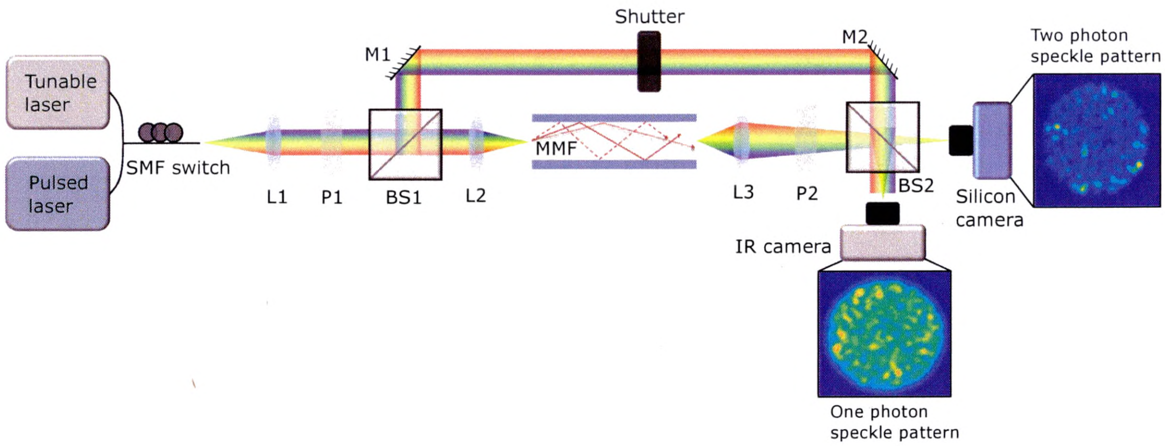

Figure 7.2: Schematics of the experimental setup. A tunable laser and a pulsed laser are coupled to a single-mode fiber switch (SMF switch). In the calibration, the fiber-switch couples light from the tunable laser to the setup. Light is collimated by a lens (L1) and polarized by a polarizer (P1). The beam splitter (BS1) splits light into a fiber arm and a reference arm. In the fiber arm, light is coupled into the multimode fiber (MMF) by a lens (L2). The output light from the fiber is imaged and polarized by another lens (L3) and a polarizer (P2). The path-length of the reference arm is adjusted by the two mirrors (M1, M2) to match that of the fiber arm. The reference beam and the output light from the MMF are recombined by a beam splitter (BS2). The IR camera record the hologram. In the measurement, the fiber-switch couple light from the pulsed laser. The reference beam is blocked by the optical shutter. A silicon camera detects the two-photon pattern.

7.2.2 Neural network and training data

We employ the architecture of Res-Net 18 [12] with the structure of the last layer adapted to our specific problem in Pytorch machine learning library [13]. The weights of the CNN are optimized using Adam [14]. The neural network is trained for 1000 epochs with the initial learning rate set to $r = 1\times10^{-4}$. The learning rate is shrunk by a factor of 0.1 each time after 200, 400 and 800 epochs.

We generate a set of pulses with the amplitude $A(\omega)$ recovered from the linear speckle pattern. To simplify the optimization problem, we represented the spectral phase in a sparse parameter basis. We present the spectral phase in a polynomial basis and considered the discontinuity in the spectral phase when the amplitude reaches a local minimum. The spectral phase is expressed as

$$\theta(\omega) = \sum_i \alpha_i \Theta(\omega, i) + a(\omega - \omega_0)^2 + b(\omega - \omega_0)^3 + c(\omega - \omega_0)^4.$$

Here $\Theta(\omega, i)$ is the Heaviside function with the discontinuity at the i^{th} local minimal of the spectral amplitude. The phase jump is due to the interference in time when there are multiple pulses. The coefficient α_i thus controls the magnitude of the phase jump, which is within the range from -π to π. The polynomial terms take into account of second, third and fourth-order chirps at the center frequency ω_0, which is defined as the center of mass of the spectral intensity $\omega_0 = \frac{\int \omega |A(\omega)|^2 d\omega}{\int |A(\omega)|^2 d\omega}$. Depending on the optical pulse, one might need to present the spectral phase with higher-order terms. With the simplified spectral phase, the CNN now only needs to predict the few key parameters. We numerically generate 10,000 pairs of pulses and two-photon patterns, 8000 of which are used as the training data set and the rest is used as the validation data set.

7.3 Numerical validation

To quantitatively evaluate the accuracy of our recovery algorithm, we performed two sequential measurements of the transmission matrix. With the first transmission matrix (TM1), we generate a set of pairs of pulses and two-photon patterns for training the CNN. Next, we calculate the two-photon patterns of pulses that have never been seen by the CNN with the second transmission matrix (TM2). The pairs of two-photon patterns and pulses generated from TM2 are used as the test data to evaluate the trained CNN. By using two transmission matrices, we are able to account for the noise in the measurement and the effect of environmental changes on the stability of the MMF.

With an experimentally measured spectrum shown in Fig. 7.5(a), we simulate

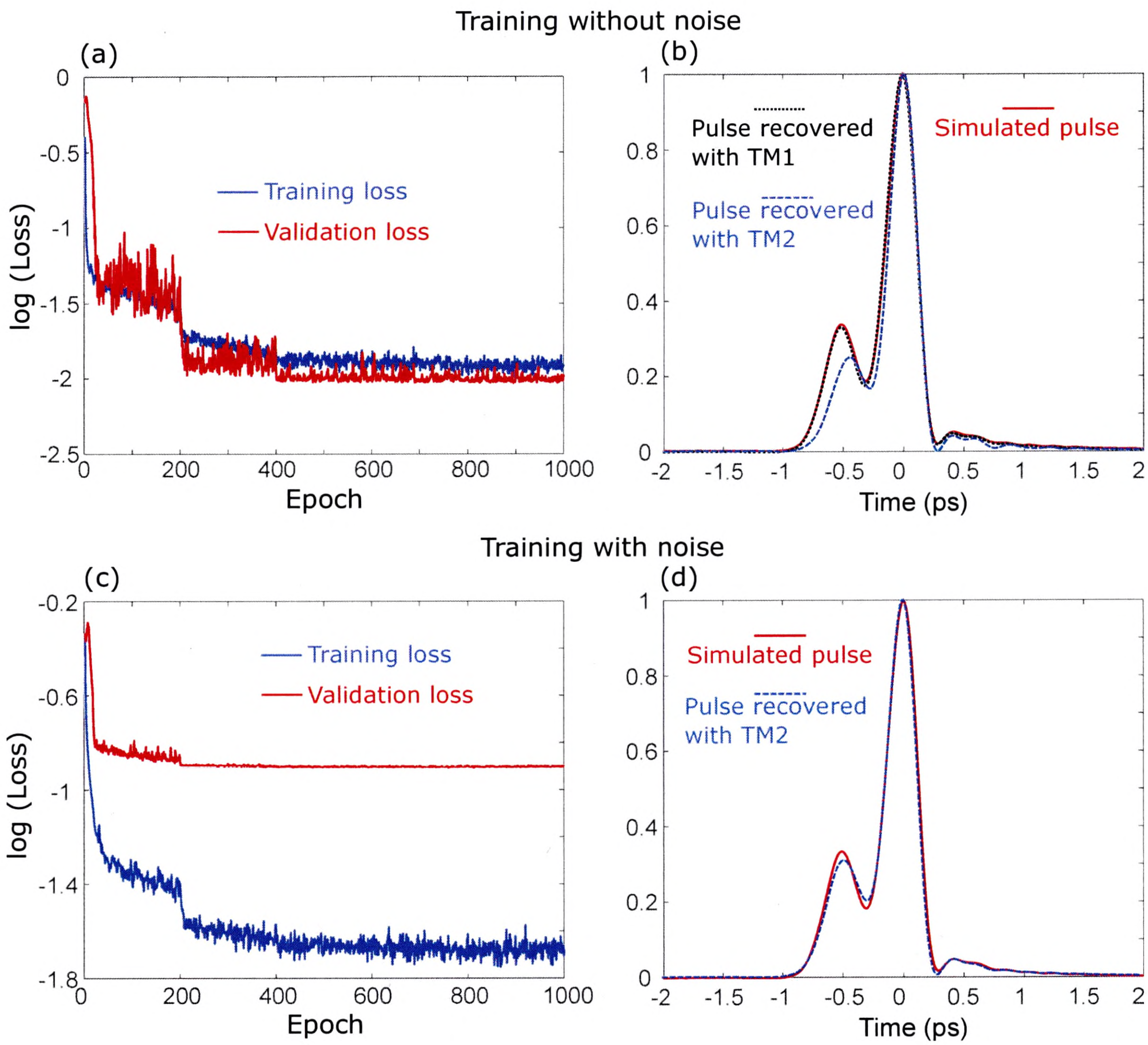

Figure 7.3: Numerical validation of the deep neural network with two transmission matrices. (a) Loss curve of the training process using TM1. (b) Temporal shape of a sample pulse. Red solid curve: the simulated pulse (ground truth). Black dotted curve: the pulse shape recovered with the two-photon pattern generated by TM1 and the CNN trained by TM1. Blue dashed curve: the pulse shape recovered with the two-photon pattern generated by TM2 and the CNN trained by TM1. (c) Loss curve of the training process using TM1 with phase noise. (d) Temporal shape of the pulse recovered with TM2 after the CNN training with noise.

10,000 pairs of pulses and two-photon patterns. A phase jump at 1541.4 nm is assumed to be in the range from $-\pi$ to π. The coefficients of the second, third and fourth-order chirp terms are [-0.3, 0.3], [-0.05, 0.05] and [-0.005, 0.005] respectively. The loss curve of the training process with the data generated by TM1 is shown in Fig. 7.3(a). We observe similar training and validation losses, with the lowest validation loss being 0.01. A sample pulse in the validation data set is plotted in Fig. 7.3(b). Since the CNN is trained by TM1, the pulse recovered from the two-photon pattern generated by TM1 (black dotted curve) agrees well with the ground truth of the simulated pulse (red solid curve). The pulse recovered from the two-photon pattern generated by TM2 (blue dashed curve), however, deviates from the simulated pulse more significantly. The loss obtained with the test data is 0.25, much higher than the 0.01 validation loss. The increase of the loss mainly results from wavelength-dependent phase fluctuations in the interferometric measurement of transmission matrices. To account for the phase noise, we add a phase fluctuation to each column of the training matrix TM1. The noise is drawn from a Gaussian distribution with its mean at zero. We tune the variance of the noise distribution to reduce the test loss. With the optimized variance of 0.22, we obtain the training and validation losses shown in Fig. 7.3(c). The minimum training loss is 0.02 while the minimum validation loss is 0.126. The gap between the training loss and the validation loss is the effect of overfitting because the phase noise is not a feature that can be learned by the CNN. The training with noise reduces the test loss from 0.25 to 0.14. The test loss now is very close to the validation loss. The pulse shape recovered with TM2 after the training with noise now agrees better with the simulated pulse.

The numerical simulation confirms that the CNN can learn pulse shapes from two-photon patterns formed at the end of the multimode fiber. By intentionally adding the wavelength-dependent phase noise in the transmission matrix used for the training, the CNN can account for the phase noise in the measurement.

7.4 Experimental measurement

Experimentally, we characterize the propagation of a pulse from a femtosecond laser (NKT, Onefive Origami) through a one-meter-long single-mode fiber. Due to the dispersion and nonlinearity in the single-mode fiber, the output pulse shape is broadened and distorted. Both the spectral amplitude and phase are changed after the propagation. By controlling the power coupled into the single-mode fiber, we can tune the strength of nonlinearity and thus adjust the distortion in the spectral amplitude and phase of the ultrafast pulses.

We first experimentally measured the pulse when the nonlinearity is very weak. The pulse spectra measured by the optical spectrum analyzer (OSA, YOKOGAWA AQ6370D) and reconstructed from the one-photon pattern recorded by the IR camera is shown in Fig. 7.4(a). The overlap of two curves validates the accuracy of the spectrum recovery. For this smooth spectrum, we assume second, third and fourth-order chirp terms and no phase jumps in the spectral phase. The ranges of chirp terms are the same as specified in section 7.3. The recovered spectral phase in Fig. 7.4 is flat at frequencies with significant intensities, indicating a nearly transform-limited pulse. From the spectral intensity and phase, we reconstruct the temporal profile of the pulse, as shown by the blue dotted line in Fig. 7.4(b). There are no obvious distortions or side lobes in the temporal profile, as expected for a transform-limited pulse. To quantitatively estimate the accuracy of the reconstructed temporal profile, we further calculate the AC trace of the pulse. Though there are ambiguities when recovering a pulse shape from its AC trace, the AC trace is still a useful metric to evaluate the accuracy of the pulse shape recovered from other methods. The AC trace of the recovered pulse agrees well with the AC trace measured by an auto-correlator (Femtochrome FR-103XL). Since we are using the two-photon pattern to recover the pulse shape, the recovered pulse should generate a similar two-photon pattern with the experimentally measured one. The experimentally measured two-photon pattern

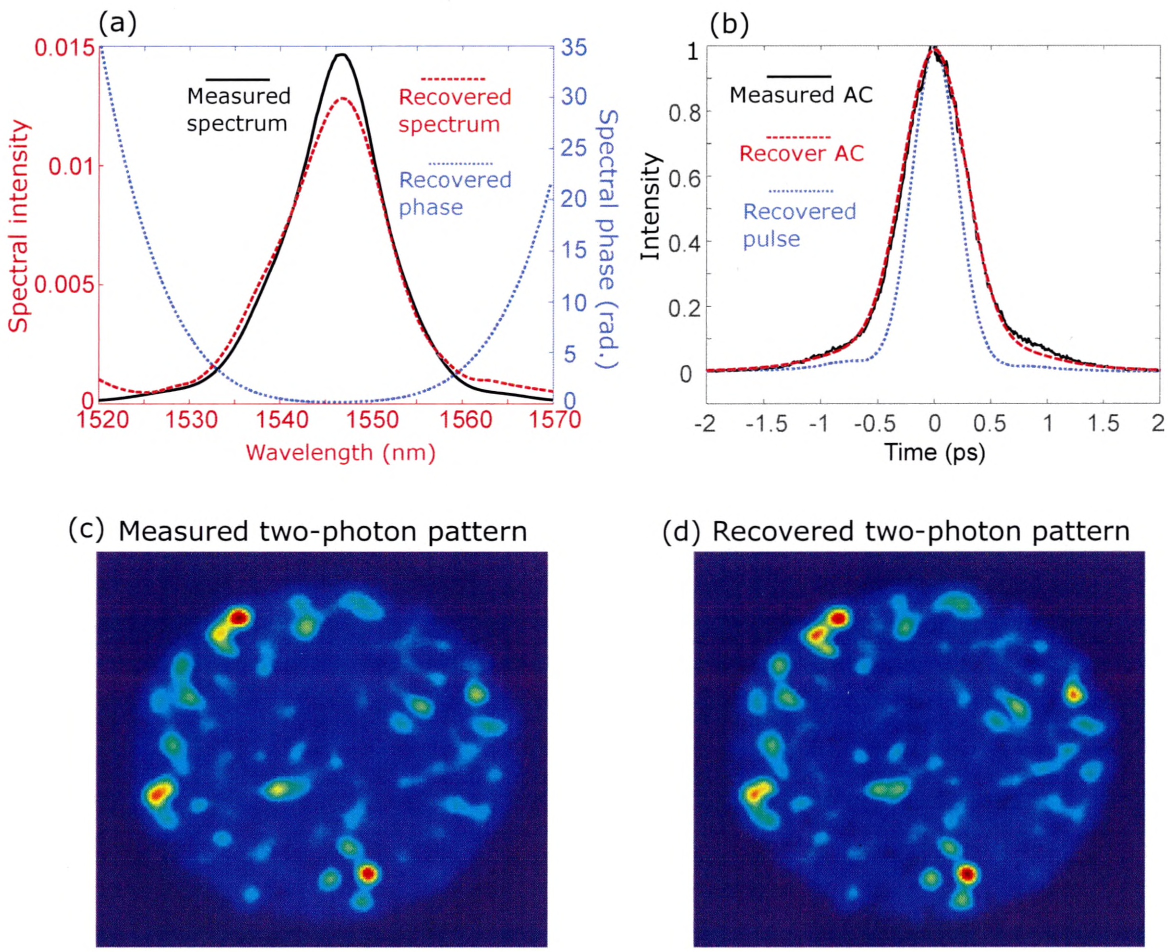

Figure 7.4: Recovery of a nearly transform-limited pulse. (a) Recovered spectral intensity (red dashed line) and phase (blue dotted line) of the nearly transform-limited pulse as compared to the spectral intensity measured by the OSA (black solid line). (b) Recovered pulse shape (blue dotted line) and auto-correlation (AC) trace (red dashed line) of the pulse. The experimentally measured AC trace is plotted as the black solid curve. (c) Experimentally measured two-photon pattern. (d) Two-photon pattern reconstructed with the transmission matrix and the recovered spectral amplitude and phase.

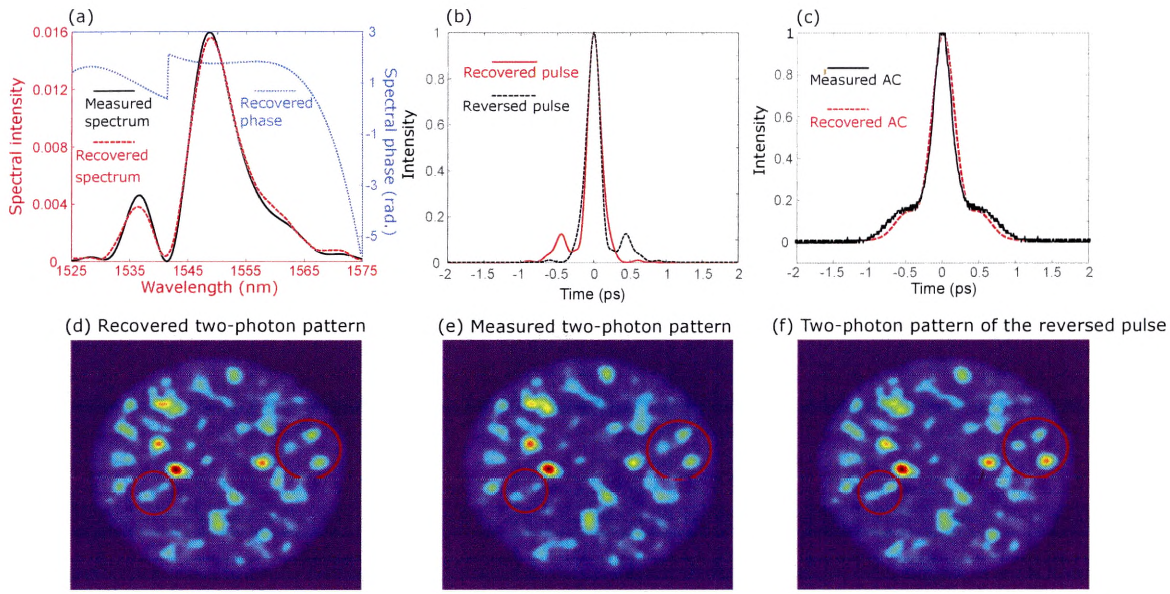

Figure 7.5: Recovery of a distorted pulse after nonlinear propagation. (a) Recovered spectral intensity (red dashed line) and phase (blue dotted line) of the distorted pulse as compared to the spectral intensity measured by the OSA. (b) Recovered pulse shape (red solid line) and its time-reversed pulse (black dashed line). (c) Experimentally measured AC trace and the AC trace reconstructed with the pulse in (b). (d) Two-photon pattern reconstructed with the transmission matrix and the recovered spectral amplitude and phase. (e) Experimentally measured two-photon pattern. (f) Two-photon pattern reconstructed with the time-reversed pulse.

of this transform-limited pulse is shown in Fig. 7.4(c). With the transmission matrix and the recovered spectral amplitude and phase, we calculate the two-photon pattern [Fig. 7.4(d)] of this pulse. The agreement of both the AC traces and the two-photon patterns validates the recovered pulse shape.

By coupling more power into the single-mode fiber, we enhance the nonlinearity to introduce distortions. The spectrum of the distorted pulse measured by the OSA and recovered with the one-photon speckle are plotted in Fig. 7.5(a). Due to the nonlinearity, the spectrum presents a local minimal at $\lambda \sim 1541.4$ nm. We assume a spectral phase with a phase jump at this wavelength and chirp terms up to the fourth-order. There is one more local minimum at 1530.6 nm, but the modulation is too shallow to affect the temporal pulse shape. Thus we ignore this local minimum. The ranges of the parameters are specified in section 7.3. We recovered the spectral phase shown by the blue dotted line in Fig. 7.5(a). The phase presents a significant jump. With the recovered spectral amplitude and phase, we obtained the pulse shape shown by the red solid curve in Fig. 7.5(b). The pulse is distorted with a side lobe. The AC trace calculated with the recovered pulse shape is shown in Fig. 7.5(c). Comparing to the AC trace measured experimentally, we achieve a high agreement. The time-reversed counterpart of the reconstructed pulse [black dashed line in Fig. 7.5(b)] can generate the same AC trace, which is the well-known time-reversal ambiguity in autocorrelation. This ambiguity is also known in some existing pulse characterization techniques [15]. The two-photon speckle pattern is sensitive to the direction of the pulse in time and the ambiguity is removed in our method. Figure 7.5(d) - (e) show the two-photon pattern calculated with the recovered pulse and the experimentally measured one. The difference between the two patterns is 9.8%. For the time-reversed pulse, the error increases to 13.3%. The red circles on the patterns highlight several speckle grains. The speckle pattern of the recovered pulse and the experimentally measured one are more similar. Though the difference is small, it is enough for the algorithm to distinguish the pulse from its time-reversed counterpart.

7.5 Discussion and conclusion

Our scheme relies on the complexity of the speckle pattern formed at the end of a multimode fiber to provide a unique fingerprint of an optical pulse. It is possible since each speckle grain at the end of the fiber is formed by a different sampling of the pulse. In the spectral domain, each speckle consists of a random summation of the different spectral components of the pulse, each with varying amplitude and phase. In the time domain, each speckle grain is a measurement of the pulse after it passes through a different dispersive medium. The silicon camera detects many speckle grains in parallel, so we are able to differentiate pulses which may introduce ambiguities in other pulse characterization methods.

Using this approach, we experimentally reconstructed ultrafast pulses propagating through a single-mode fiber with nonlinearity. The recovered pulse shape is verified with the auto-correlation traces and the two-photon patterns. Similar to their applications in computer vision, the convolutional neural network performs a complex mapping between the pattern and the spectral phase parameters. The phase noise accumulated in the transmission matrix measurement can be reduced by assuming a similar amount of noise in the training data. Numerical simulations with two sequentially measured transmission matrices validate the effectiveness of the deep neural network for recovering the spectral phase. As with the problem of computer vision or other artificial intelligence, a deep neural network is usually data-hungry. It demands a lot of data to obtain good performance. The advantage of our method is that with the transmission matrix, we can easily generate a huge amount of numerical data for the training. Comparing to training a neural network with experimental data, numerical data is more efficient in terms of both time and cost.

Bibliography

[1] W. Xiong, B. Redding, S. Gertler, Y. Bromberg, H. Tagare, and H. Cao, Deep learning of ultrafast pulses with a multimode fiber, arXiv preprint arXiv:1911.00649 (2019).

[2] H. P. Weber, Method for pulsewidth measurement of ultrashort light pulses generated by phaselocked lasers using nonlinear optics, J. Appl. Phys. **38**, 2231-2234 (1967).

[3] D. J. Kane and R. Trebino, Single-shot measurement of the intensity and phase of an arbitrary ultrashort pulse by using frequency-resolved optical gating. Opt. Lett. **18**, 823-825 (1993).

[4] C. Iaconis and I. A. Walmsley, Spectral phase interferometry for direct electric-field reconstruction of ultrashort optical pulses, Opt. Lett. **23**, 792-794 (1998).

[5] V. V. Lozovoy, I. Pastirk and M. Dantus, Multiphoton intrapulse interference. IV. Ultrashort laser pulse spectral phase characterization and compensation. Opt. Lett. **29**, 775-777 (2004).

[6] J. W. Nicholson, J. Jasapara, W. Rudolph, F. G. Omenetto and A. J. Taylor, Full-field characterization of femtosecond pulses by spectrum and cross-correlation measurements, Opt. Lett. **24**, 1774-1776 (1999).

[7] B. Redding and H. Cao, Using a multimode fiber as a high-resolution, low-loss spectrometer, Opt. Lett. **37**, 3384-3386 (2012).

[8] B. Redding, M. Alam, M. Seifert and H. Cao, High-resolution and broadband all-fiber spectrometers, Optica **1**, 175-180 (2014).

[9] V. Wong and I. A. Walmsley, Analysis of ultrashort pulse-shape measurement using linear interferometers, Opt. Lett. **19**, 287-289 (1994).

[10] D. Panasenko and Y. Fainman, Single-shot sonogram generation for femtosecond laser pulse diagnostics by use of two-photon absorption in a silicon CCD camera, Opt. Lett. **27**, 1475-1477 (2002).

[11] T. Zahavy, A. Dikopoltsev, D. Moss, G. I. Haham, O. Cohen, S. Mannor and M. Segev, Deep learning reconstruction of ultrashort pulses, Optica **5**, 666-673 (2018).

[12] K. He, X. Zhang, S. Ren and J. Sun, Deep residual learning for image recognition, Proceedings of the IEEE conference on computer vision and pattern recognition, 770-778 (2006).

[13] R. Collobert, S. Bengio and J. Marithoz, Torch: a modular machine learning software library, IDIAP-RR-46-2002 (2002).

[14] D. P. Kingma and J. Ba, Adam: A method for stochastic optimization, arXiv preprint arXiv:1412.6980 (2014).

[15] R. Trebino, P. Bowlan, P. Gabolde, X. Gu, S. Akturk and M. Kimmel, Simple devices for measuring complex ultrashort pulses, Laser Photonics Rev. **3**, 314-342 (2009).

Chapter 8

Conclusion and future prospect

A multimode fiber is a complex photonic system that couples degrees of freedom of light in space, time, frequency and polarization. The abundant degrees of freedom in space enable effective control and measurement of the degrees of freedom in other domains, making a multimode fiber a versatile and multi-functional platform for studying wave physics and for inventing novel optical techniques.

In the first part of this thesis (chapter 2-5), we utilized the spatial degrees of freedom at the input of a multimode fiber to control the degrees of freedom in time and polarization at the output. We accessed the spatial degrees of freedom via the wavefront shaping technique. To perform the control, we first needed a complete calibration of the multimode fiber. Using a spatial light modulator, we calibrated the response of the fiber to different wavefronts. Comparing to other complex photonic structures such as disordered scattering media, multimode fibers had the advantage of a controllable number of modes, which made the complete calibration possible. With the full transmission matrix, the linear propagation of light in the fiber is fully captured. For specific control, additional information about the transmission matrix was needed. For example, to understand the temporal dynamics of a pulse propagating through the fiber, transmission matrices at different frequencies were required.

To control the polarization state, a polarization-resolved transmission matrix was needed.

In chapter 2 to 4, we studied the dynamics of pulses transmitted through multimode fibers. We demonstrated three methods of global spatiotemporal control. By controlling the input wavefront, we were able to control the output temporal profile in all spatial channels. The three methods all relied on measuring the wavelength-resolved transmission matrix of a multimode fiber. In chapter 2, we experimentally probed individual eigenstates of the Wigner-Smith time-delay matrix, i.e., principal modes, of a multimode fiber in both the weak and strong mode coupling regime. We revealed the unique property of principal modes that the spatial and temporal profiles were decoupled, which enabled the global spatiotemporal control. We found that principal modes were formed by multi-path interference. By manipulating the input wavefront to destructively interfere the paths with very different path-lengths, principal modes overcame modal dispersions in the fiber even in the presence of strong mode coupling. This property is desired in applications such as optical communication. However, this property of principal modes can only be retained within a narrow frequency range, limiting its effectiveness for short pulses. The bandwidth limit resulted from the definition of principal modes, in which only the first-order approximation was taken into account.

In chapter 3, we proposed super-principal modes, which exhibited broader bandwidths than principal modes. Super-principal modes were achieved by directly optimizing a nonlinear cost function with the initial guess to be principal modes. The optimization algorithm allowed us to determine a whole set of super-principal modes, which were mutually orthogonal to each other. Reversing the concept, we also found anti-principal modes, the modes that exhibited much narrower bandwidths and experienced the strongest modal dispersion in the fiber. By decomposing super- and anti- principal modes into principal mode basis, we found that super-principal modes tended to combine several principal modes with nearby delay times in a super-position with optimized phases. Anti-principal modes, on the contrary, tended to combine principal modes with the most different delay times available in the fiber.

Both principal modes and super-principal modes revealed the possibility of delivering an undistorted pulse through a multimode fiber with wavefront shaping. Super-principal modes improved the bandwidth by a factor of two, making the technique more practical for short pulses. However, it was unknown what was the most effective way to deliver an arbitrarily short pulse at any target arrival time. We addressed this fundamental question in chapter 4. We resolved this problem by studying the maximum eigenmodes of a time-resolved transmission matrix of the multimode fiber. This method was effective for any input pulse with an arbitrarily broad spectrum. The maximal power delivery was guaranteed at any target arrival time. The eigenmodes outperformed principal modes and super-principal modes in the broad bandwidth regime, and converged to principal modes in the narrow bandwidth regime. More interestingly, we found that long-range correlations played an important role in the pulse delivery process. The correlation not only determined the achievable enhancement via wavefront shaping, but also captured the temporal shape of the optimized pulses. Short- and long-range correlations had been studied extensively in scattering media, but there were few observations in other complex photonic systems before our work in chapter 4. The above three chapters provided a systematical discussion on spatiotemporal control, revealed the effectiveness and limitations of different methods and provided physics understandings of these methods.

In chapter 5, we studied complete polarization control with the spatial degrees of freedom. Strong coupling between spatial and polarization degrees of freedom in an MMF enabled control of output polarization states in all spatial channels by manipulating only the spatial input wavefront. A general procedure of finding the spatial wavefront to create an arbitrary polarization state involved measurement of the polarization-resolved transmission matrix and a selective excitation of the transmission eigenchannels corresponding to the extremal eigenvalues. With random mixing among all modes of different polarizations in the fiber, the probability of having extremal eigenvalues was enhanced by eigenvalue repulsion, analogous to a chaotic cavity. We applied the existing theory of chaotic cavities to multimode fibers, uncovering the connection between the two fields of wave chaos and fiber optics. The global control of polarization states for MMFs could be not only useful for overcoming the depolarization in an MMF, but also valuable for employing polarization-sensitive imaging techniques of fiber endoscopy and nonlinear microscopy.

The second part of this thesis (chapter 6 to 7) is complementary to the first part. In this part, we demonstrated that the spatial degrees of freedom at the output of a multimode fiber were useful for characterizing ultrafast pulses. Chapter 6 provided a referenced method when a reference pulse was available while chapter 7 solved the problem with a self-referenced scheme. Both schemes utilized the complex spatiotemporal speckle generated at the output of a multimode fiber and achieved single-shot measurement. The scheme in chapter 6 was based on linear interferometry and thus possessed a high sensitivity. On the contrary, the scheme in chapter 7 required nonlinear measurement and high power level. The advantage of the scheme in chapter 7 was that it required no reference and was able to measure stand-alone ultrafast pulses.

The mathematical inverse problems in chapter 6 and 7 were at different complexity levels. For the linear interferometric measurement, we only needed to solve a linear inverse problem. However, for the self-referenced method, we needed to solve a highly nonlinear and non-convex optimization problem. We took full advantage of the fast-developing computational algorithms. The compressive sensing algorithm employed in chapter 6 was a time-efficient algorithm for solving linear inverse problems. With prior information on the spectrum of the pulse, we were able to measure more channels in time than the spatial degrees of freedom in the fiber. In chapter 7, we utilized convolutional neural networks, the well-developed tool in artificial intelligence, to perform the optimization. The neural network mapped the two-photon speckle pattern to the temporal pulse shape. As the problem in computer vision, a deep neural network is data-hungry. But with a calibrated transmission matrix, we were able to generate a large amount of numerical data for the training. Our work illustrated the possibility of solve complex photonic problems with artificial intelligence.

In summary, this thesis investigated spatial degrees of freedom in multimode fibers. Physics, concepts and methods provided in this thesis may also be used in other complex photonic systems. For example, principal modes also exist in disordered scattering media. It would be interesting to study the bandwidth of principal modes in the scattering media. Because the path-length distribution is different, we expect different results. Long-range correlation in scattering media has been studied for many years. The dynamics of the correlation, i.e., how the long-range correlation changes with time when a pulse is transmitted through the system, is still unknown. It is also an interesting topic and requires further investigation. Though we only studied passive multimode fibers, these ideas in active fibers can be more complex but intriguing. We hope this thesis can provide some guidance and intuition for future studies in the research field of complex photonics.